Searching for Pulsars in Unassociated *Fermi*-LAT sources

Hung Kit (Jason) Wu

Searching for Pulsars in Unassociated *Fermi*-LAT sources

Dissertation

zur

Erlangung des Doktorgrades (*Dr. rer. nat.*)

der

Mathematisch-Naturwissenschaftlichen Fakultät

der

Rheinischen Friedrich–Wilhelms–Universität Bonn

vorgelegt von

Hung Kit (Jason) Wu

aus

Hong Kong

Bonn, 2017

Angefertigt mit Genehmigung der Mathematisch-Naturwissenschaftlichen Fakultät
der Rheinischen Friedrich–Wilhelms–Universität Bonn

1. Referent: Prof. Dr. M. Kramer
2. Referent: Prof. Dr. N. Langer
Tag der Promotion: 09.04.2018
Erscheinungsjahr: 2018

Diese Dissertation ist auf dem Hochschulschriftenserver der ULB Bonn unter
http://hss.ulb.uni-bonn.de/diss_online elektronisch publiziert

RHEINISCHE FRIEDRICH–WILHELMS–UNIVERSITÄT BONN

Abstract

by Hung Kit (Jason) Wu for the degree of

Doctor rerum naturalium

Pulsars have always been under the γ-ray spotlight since the birth of γ-ray astronomy. They were the first sources that were firmly established as γ-ray sources in the 70s. Since then, pulsars have been the prime suspect of unassociated γ-ray sources in our Galaxy. The Large Area Telescope (LAT) is the game changer of γ-ray astronomy, on-board the *Fermi* Gamma-ray Space Telescope which launched in 2008, has increase the known population of γ-ray by over a factor of 30 in just 8 years. It enabled the discoveries of pulsars in different types through their γ-ray pulsations, including a large number of millisecond pulsars, which were originally thought to be weak in γ-rays. Many of the young γ-ray pulsars discovered have not yet been detected in subsequent radio searches, like the famous Geminga pulsar. These "radio-quiet" γ-ray pulsars population can only be accessed through blind periodicity searches in γ-rays. Therefore, γ-ray observations is the only way to complete the radio-quiet part of the Galactic pulsar population.

This thesis describe the most recent major blind search survey of γ-ray pulsar – Einstein@Home γ-ray pulsar survey. Firstly, technique using machine learning were used in identifying viable unassociated γ-ray sources for blind searches. This algorithm incorporate spectral, temporal behaviour and γ-ray flux information of individual γ-ray sources to divide them into different clusters. Secondly, LAT photons associated with these sources were weighted according to the spectral result to improve the sensitivity of subsequent blind searches. γ-ray sources selected for the blind-search survey was performed on the distributed volunteer computing system Einstein@Home using the multi-stages semi-coherent technique, which is optimized for the long duration LAT dataset. This resulted in the discovery of seventeen isolated γ-ray pulsars. Follow-up multi-wavelength analysis reveals the new discoveries are mostly similar with the existing γ-ray pulsar population.

However, temporal behaviours of several pulsars discovered in this survey are peculiar. This includes a young glitching pulsar PSR J1906+0722; the youngest radio-quiet γ-ray pulsar ever found PSR J1208−6238, its high magnetic field strength with its young age enable the measurement of its braking index, which is the only measurement for radio-quiet γ-ray pulsar; the discovery of the first two isolated millisecond pulsars PSRs J1035−6720 & J1744−7619 from γ-ray blind search, one of which remained radio quiet despite the deepest searches conducted by the Parkes radio telescope.

Utilizing Effelsberg's Ultra-Broad-Band receiver, currently under commission, originally designed for precision pulsar timing, 54 unassociated γ-ray sources were observed to explore the possibility of using wide band receiver for simultaneous pulsar searching observation in multiple radio bands. Simulations of the expected discovery yield suggested that less than one pulsar is expected to be found by random chance. Flux densities upper limits were present for all observations and the reasons of non-detection were also discussed.

This thesis is concluded by the summary of the completed blind search survey, current status of ongoing and upcoming blind search γ-ray pulsar projects, and the impact of the new collection of γ-ray pulsars to the current pulsar population.

To humanity...

Each piece, or part, of the whole nature is always an approximation to the complete truth, or the complete truth so far as we know it. In fact, everything we know is only some kind of approximation, because we know that we do not know all the laws as yet. Therefore, things must be learned only to be unlearned again or, more likely, to be corrected. The test of all knowledge is experiment. Experiment is the sole judge of scientific "truth".

Richard Feynman
The Feynman Lectures, Introduction

Contents

List of Figures

List of Tables

Chapter 1

Pulsars Astrophysics

Contents

1.1 Introduction

Pulsars are great tools for both astrophysics and high-energy particle physics studies. For particle physicists, they provide a unique laboratory to probe high-energy γ-rays and particle acceleration. For astronomers and astrophysicists, they are the perfect examples of exotic, dense stars to study how physics behaves under extreme conditions. A pulsar is a rapidly rotating neutron star, formed after a massive core-collapse supernova, that emits pulsed radiation across the electromagnetic (EM) spectrum. It is a gateway for understanding the structure, formation, and evolution of neutron stars. The detection of over 2,600 pulsars in our Galaxy[1] indicates that pulsars are not rare, but abundant. Due to observational biases such as flux limitations and radiation beaming, we might not observe pulsars across the entire frequency spectrum. γ-ray pulsars, named because we directly observe their γ-ray emission, comprise a considerable portion ($\sim$ 10%) of the pulsar population (Abdo et al., 2013), second to radio pulsars. Pulsars have a wide range of rotation periods, rotational kinetic-energy losses and ages. However, the emission geometry and the Galactic population are not well understood. Finding more pulsars is the key in understanding pulsar properties, their evolution, and their roles in Galactic evolution.

The first pulsar (now known as PSR J1921+2153) was discovered accidentally in the radio wavelength (Hewish et al., 1968) and this was rapidly followed by the discovery of pulsars in the Crab nebula and Vela supernova remnant. The Crab pulsar was subsequently found in optical (Cocke et al., 1969), X-rays (Bradt et al., 1969), and γ-rays (Browning et al., 1971). The early γ-ray satellite SAS-2 (Derdeyn et al., 1972) discovered high-energy emission from the Vela pulsar (Thompson et al., 1975). The COS-B γ-ray satellite (Bignami et al., 1975) compiled the first catalog of γ-ray sources which included two pulsars and one unknown source, which turn out to be the radio-quiet pulsar Geminga (PSR J0633+1746) (Hermsen et al., 1977). Decades later, pulsations from seven γ-ray pulsars were measured by COMPTEL and EGRET both onboard the Compton Gamma-Ray Observatory (CGRO) (Thompson, 2008). This established the link between Galactic unassociated γ-ray sources with pulsars. The latest generation of γ-ray telescopes – the *Fermi* Gamma-ray Space Telescope (*Fermi*) and *Astro-Rivelatore Gamma ad Immagini LEggero (AGILE)* have increased the number of γ-ray pulsars by a factor of 30 with many unexpected discoveries.

Pulsars play several important roles in many areas of high-energy astrophysics, for example: supernova remnants (SNRs), pulsar wind nebulae (PWNe), gravitational waves, and tests of general relativity. SNRs are the structures remaining after a supernova explosion, where the stellar material ejected from the supernova explosion interacts with the surrounding interstellar gas to form a shock wave, which is one of the Galactic Cosmic Rays acceleration sites (Blasi, 2013). Active pulsars are occasionally found in these supernova remnants. For example, the Vela pulsar in the Vela SNR (Thompson et al., 1975) and PSR J0007+7303 in the CTA-1 SNR (Abdo et al., 2008). The study of PWNe, the extended nebulae formed as pulsar winds expand into

[1] http://www.atnf.csiro.au/people/pulsar/psrcat/

their surroundings, can also provide clues to the Galactic Cosmic Rays origin, particularly the leptonic component (Weinstein, 2014). For example, TeV γ-ray has been observed from PWN 3C 58 which is powered by one of the highest spin-down power PSR J0205+6449 (López-Coto, 2016). Furthermore, pulsars can be used to detect gravitational waves in Pulsar Timing Arrays (Hobbs, 2011), and the verification of the strong-field limit of general relativity (Hulse & Taylor, 1975; Kramer et al., 2006).

It is clear that pulsars have important roles in the Galaxy and many applications in the study of astrophysics. In the following sections, the characteristics of pulsars, the Galactic pulsar population and various pulsar emission models will be discussed.

1.2 Characteristics of pulsars

1.2.1 Spin period and spin-period derivative

The first and the most basic characteristic of a pulsar is its spin period, P, the time lapsed between consecutive pulses. If a pulsar is regularly monitored over a long period (months to years), a change in the spin period can also be observed. The rate of change of the spin period (i.e. spin-period derivative), $\dot{P} = \mathrm{d}P/\mathrm{d}t$, which is usually a small positive number, indicates the pulsar's rotation is slowing down over time. Negative spin-period derivative can also be seen on pulsars which are in the process of accretion or on pulsars in globular cluster's where the intrinsic spin-period derivative may be contaminated by the acceleration in the cluster gravitation potential. We can calculate important pulsar properties such as the age, magnetic field, and rotational energy loss using the rotational spin parameters P, $\dot{P}$ and assumptions about mass and size. I will present here some of the relationships following the discussion of Lorimer & Kramer (2005).

1.2.2 Rotational energy loss

The observed positive $\dot{P}$ implies energy loss by the slowdown of the pulsar rotation. The energy loss is thought to be converted into radiation and particle wind. Following the discussion of Lorimer & Kramer (2005), we assume the moment of inertia of a pulsar I, with a mass of 1.4 M_{sun} and a radius of 10 km, to be 10^{45} g cm^2. For a rigidly rotating object the rotation energy is $E = \frac{1}{2} I \omega^2$, so the time derivative (energy loss) due to emission would be

$$\dot{E} = I \omega \dot{\omega}. \tag{1.1}$$

As the intrinsic $\dot{P}$ is positive for all rotational-powered pulsars, it naturally gives a negative $\dot{E}$. The amount of power loss is often denoted as spin-down luminosity L_{sd}. The spin-down luminosity, period and period derivative are related as shown in this formula:

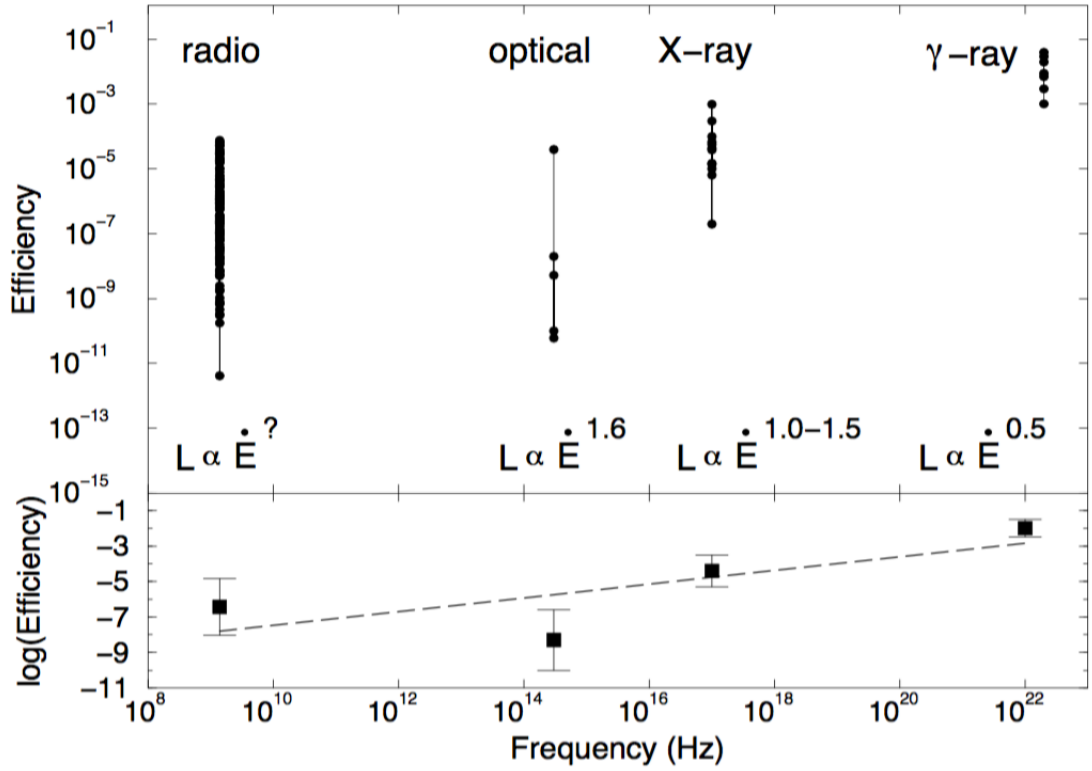

Figure 1.1 Upper panel: Efficiency, $\eta \equiv L_{\rm sd}/\dot{E}$, as derived for radio, optical, X-ray and γ-ray frequencies. The inferred efficiency is different in each energy band. Lower panel: Power law fitted to the median values of the inferred efficiency shows an increases of efficiencies with frequencies of $\eta \propto f^{0.17 \pm 0.10}$ (Lorimer & Kramer, 2005).

$$L_{\rm sd} = \frac{4\pi^2 I \dot{P}}{P^3} \sim 4 \times 10^{31} \left(\frac{I}{10^{45}\ {\rm g\ cm^2}}\right) \left(\frac{P}{1\ s}\right)^{-3} \left(\frac{\dot{P}}{10^{-15}}\right) {\rm erg\ s^{-1}}. \tag{1.2}$$

The efficiency $\eta \equiv L_{\rm sd}/\dot{E}$ of pulsed emission across the EM band varies. Figure 1.1 shows the efficiency in different wavelengths. There is a general trend that the efficiency increases as the frequency increases. While the least amount of spin-down energy carried away as radio wave is $\sim 0.001\%$, over 10% of the pulsar's spin down power are converted into γ-rays (see, Lorimer & Kramer, 2005).

1.2.3 Magnetic field

Pulsar radiations are driven by a strong magnetic field from the pulsar, it is not clear what the internal processes create such high surface magnetic field. Some suggested that the magnetic field builds up gradually after the neutron star was formed, while some suggested the field is inherited from the progenitor star, see Spruit (2009) for a

detailed summary on the origin of magnetic field in neutron stars. Nevertheless, the effect of the high magnetic field is clearly seen. If we assume a simple dipole field with magnetic moment $|\vec{m}|$, which is related to the surface magnetic field strength B_s by

$$|\vec{m}| = \frac{1}{2} B_s R_s^3, \tag{1.3}$$

where $R_{\rm s}$ is the radius of the neutron star. The power emitted by the dipole takes the following form,

$$L_{\rm sd} = \frac{2}{3c} |\vec{m}|^2 \omega^4 \sin^2\alpha. \tag{1.4}$$

Substituting L_{sd} using equation 1.2, we obtain

$$\dot{\omega} = -\left(\frac{2|\vec{m}|^2 \sin^2\alpha}{3Ic^3}\right)\dot{\omega}^3, \tag{1.5}$$

where α is the magnetic inclination angle.

Assuming that all energy losses from the pulsar are in the form of magnetic dipole radiation, the surface magnetic field is given by

$$B_{\rm s} = \sqrt{\frac{3c^3 I P \dot{P}}{8\pi^2 R_{\rm s}^6 \sin^2\alpha}}. \tag{1.6}$$

If we assume $\alpha = 90°$, an upper limit of $B_{\rm s}$ can be obtained

$$B_{\rm s} \sim 1 \times 10^{12} \left(\frac{P}{1\ s}\right)^{1/2} \left(\frac{\dot{P}}{10^{-15}\ {\rm s\ s^{-1}}}\right)\ G. \tag{1.7}$$

For example, a pulsar with a spin period of 1s and a spin-period derivative of 10^{-15} would have a surface magnetic field of 1×10^{12} G.

Under the influence of the pulsar's strong magnetic field, charged particles co-rotate with the pulsar within the radius where the speed of particles reach the speed-of-light. This boundary is called the light cylinder, and its radius is given by

$$R_{\rm LC} = \frac{c}{\omega}. \tag{1.8}$$

As the dipole-field strength is inversely proportional to the third power of the distance (equation 1.3), the magnetic field at the light cylinder $B_{\rm LC}$ would be

$$B_{\rm LC} = B_s \left(\frac{R_{\rm s}}{R_{\rm LC}}\right)^3 \sim 9.2\ {\rm G} \left(\frac{P}{1\ {\rm s}}\right)^{5/2} \left(\frac{\dot{P}}{10^{-15}\ {\rm s\ s^{-1}}}\right)\ {\rm G}. \tag{1.9}$$

The magnetic field strength $B_{\rm LC}$ is an useful quantity for models of which emission are produced near the light cylinder, which will be discussed in Section 1.5.

1.2.4 Magnetic braking

If we rewrite equation (1.5) by substituting ω with $\nu = 1/P$, the rotational frequency,

$$\dot{\nu} = K\nu^n, \tag{1.10}$$

where K is a constant and n is called braking index. For a pure magnetic dipole in a vacuum, we expect $n = 3$.

Taking the time derivative of equation (1.10) gives us a equation which contains only the braking index and observables

$$n = \frac{\nu\ddot{\nu}^2}{\dot{\nu}}\ , \tag{1.11}$$

this equation allow us to measure the braking index of any pulsar with measurable $\ddot{\nu}$.

However, majority of the pulsars have small $\ddot{\nu}$, hence their $\ddot{\nu}$ measurements are usually dominated by timing noise. In fact, only a few young pulsars have large $\ddot{\nu}$ allowing reliable braking indices measurement. Surprisingly, a wide range of braking indices from 0 to 3.15 were observed, for example: Vela pulsar ($n = 1.4 \pm 0.2$) , PSR B0540−69 ($n = 0.031 \pm 0.013$), PSR J1734−3333 ($n = 0.9 \pm 0.2$), Crab pulsar ($n = 2.509 \pm 0.001$), PSR B1509−58 ($n = 2.8 \pm 0.2$), PSR J1640−4631 ($n = 3.15 \pm 0.03$) (Archibald et al., 2016; Espinoza et al., 2011; Lyne et al., 1996, 1993; Marshall et al., 2016). Clearly, the observed braking indices deviate from pure magnetic dipole braking, which means that there may be other dissipation mechanisms that also carry away rotational kinetic energy: for example, in the form of particle wind ($n = 1$) (Michel & Tucker, 1969; Harding et al., 1999) or in the form of resistive torque from an in-falling disk (n = −1) (Menou et al., 2001). Also evolution of the pulsar's magnetic field, magnetic/mass quadrupole (Blandford & Romani, 1988), changes of the angle between the spin and magnetic axis (Lyne et al., 2013) would result in different braking index.

1.2.5 Age estimate

By integrating the equation (1.10), we obtain an equation of the age of a pulsar

$$T = \frac{1}{(n-1)}\frac{P}{\dot{P}}\left[1 - \left(\frac{P_0}{P}\right)^{n-1}\right] \tag{1.12}$$

where P_0 is the spin period at birth. If $P \ll P_0$ and $n = 3$, the above equation reduces to a "characteristic age"

$$\tau_c = \frac{1}{2}\frac{P}{\dot{P}}. \tag{1.13}$$

Because the characteristic age τ_c assumes a constant braking index $n = 3$ for the pulsar's whole life time, and that the birth period of the pulsar was negligible compared to its current observed period, any changes in spin-down power, spin period or braking index will give a characteristic age inconsistent with the true pulsar age. So it is important to have independent measurements of the age. For example, the characteristic

age of the Crab pulsar is 1300 years, while historical documentation of the associated supernova explosion determines to be happened 972 years ago.

1.2.6 Dispersion

As the pulsed radiation propagates through the interstellar medium (ISM), it experiences a frequency-dependent refraction, μ,

$$\mu = \sqrt{1 - \left(\frac{f_{\rm p}}{f}\right)^2}, \tag{1.14}$$

where f is the frequency of the incoming wave and $f_{\rm p}$ is the plasma frequency, given by

$$f_{\rm p} = \sqrt{\frac{e^2 n_{\rm e}}{\pi m_{\rm e}}} \simeq 8.5 \text{ kHz} \left(\frac{n_{\rm e}}{\text{cm}^{-3}}\right)^{1/2}, \tag{1.15}$$

here, e is the fundamental electrical charge, m_e is the electron mass, and n_e is the free electron density along the line of sight. For the ISM, $n_{\rm e}$ is typically ~ 0.03 cm^{-3} (Gomez-Gonzalez & Guelin, 1974; Ables & Manchester, 1976), which gives $f_{\rm p} \simeq 1.5$ kHz. Therefore, a broadband emission from pulsars propagating through the ISM to Earth is delayed depending on the frequency, as shown in Figure 1.2. The time delay ($t_{\rm DM}$) at frequency f with respect to the signal at infinite frequency is,

$$t_{\rm DM} = \mathcal{D} \frac{\rm DM}{f^2} \tag{1.16}$$

where DM is the dispersion measure, the electron density along the line-of-sight integrate over the distance to the pulsar d

$$\text{DM} = \int_0^d n_e \text{d}l \tag{1.17}$$

and $\mathcal{D}$ is the dispersion constant

$$\mathcal{D} \equiv \frac{e^2}{2\pi m_e c} = (4.148808 \pm 0.00003) \times 10^3 \text{ MHz}^2 \text{ pc}^{-1} \text{ cm}^3 \text{ s}. \tag{1.18}$$

The time difference between two frequencies, f_1 and f_2 in MHz, is

$$\Delta t_{\rm DM} \simeq 4.15 \times 10^6 \text{ ms} \times (f_1^{-2} - f_2^{-2}) \times \text{DM} \tag{1.19}$$

By applying Equation 1.19 to the observation frequencies and measured arrival times of a pulse, the frequency-dependent delay is removed, and the pulse is "de-dispersed". De-dispersion is one of the important steps in radio pulsar searching, the detail of the de-dispersion scheme used in radio pulsar searching is describe in Chapter 3.

Pulsars detected in radio are very useful in ISM studies because their pulsed radio

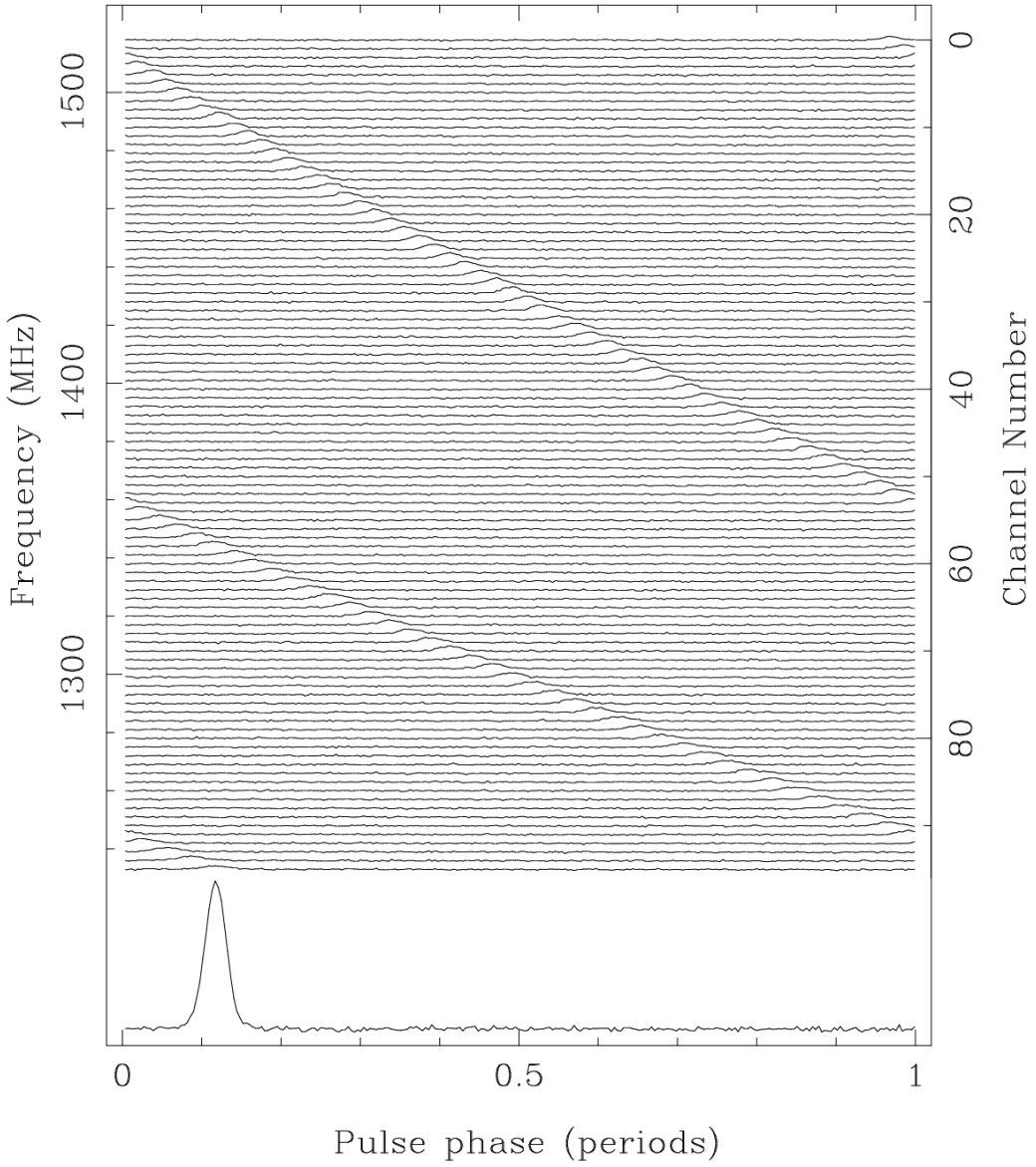

Figure 1.2 Dispersion of pulsar signal in radio. Uncorrected dispersive delays for a pulsar observation over a bandwidth of 288 MHz centered at 1380 MHz. The delays wrap since the data are folded the pulse period. (Lorimer & Kramer, 2005)

emission allows n_e to be measured. Models of the free electron density in the ISM have been constructed to translate the DM value into distance. The model most commonly used in the pulsar community is the NE2001 model[2] from Cordes & Lazio (2002). An updated version of electron density model from Yao et al. (2017)[3] is also introduced.

DM distance estimates can have quite large uncertainties, in some cases $\sim 100\%$, due to variations in n_e that are not accounted for in electron density models (Abdo et al., 2013). For example, in regions of ongoing star formation, the electron density of the ISM is much higher than the average value. A pulsar situated within or behind the star formation region will have a much larger DM and thus an over-estimated distance.

Since γ-rays do not interact with the ISM (reflect or refract), they have no dispersion measure. To estimate the distance of a radio-quiet γ-ray pulsar, a heuristic distance is used by assuming the γ-ray luminosity follows the $L_\gamma \sim \sqrt{\dot{E}}$ relationship (see Section 4.4.4).

1.3 Pulsar population

1.3.1 The $P - \dot{P}$ diagram

As mentioned in the previous chapters, apart from the DM, if available, the period and period derivative are the two fundamental observables from a pulsar. From these two observables, many physical characteristics like the spin-down powers, the characteristic ages and the magnetic field strength can be derived. In pulsar astronomy, all these quantities can be shown at once using the $P - \dot{P}$ diagram. Known rotational powered pulsars are shown in the $P - \dot{P}$ diagram (Figure 1.3). The pulsar population is mainly divided into two major sub-groups, canonical pulsars and millisecond pulsars (MSPs), based on their spin period and spin-period derivative.

1.3.2 Canonical pulsars

The majority of pulsars in the Galactic population ($\sim 90\%$) have a spin period in the range of 0.1 s to 1.0 s, and a spin-period derivative of typically $\dot{P} \sim 10^{-15}$ s s^{-1}. These are called canonical pulsars. The longest period observed from a rotationally powered pulsar is PSR J0250+58 which is 23.5 s (Tan et al., in prep.). Canonical pulsars have characteristic ages younger than ~ 100 Myr. After they formed from supernova explosions, they start to slow-down from their initial period of milliseconds to seconds and their magnetic fields are suspected to become weaker over their lifetime. When their spin period is slowed down to a point that the pulsar no longer produces significant emission, the pulsar is considered dead as it is no longer observable, entering the pulsar graveyard (Chen & Ruderman, 1993).

[2] https://www.nrl.navy.mil/rsd/RORF/ne2001/
[3] http://119.78.162.254/dmodel/index.php

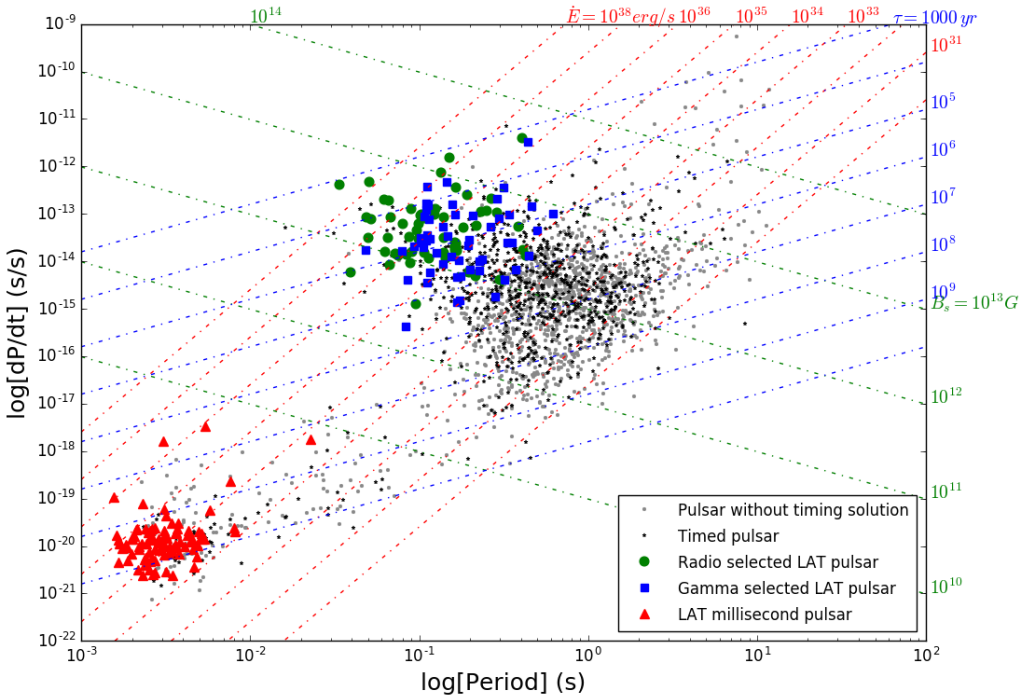

Figure 1.3 Pulsar spin-down rate, $\dot{P}$, versus the rotation period P. Green dots indicate young, radio-loud γ-ray pulsars and blue squares indicate radio-quiet pulsars, defined as $S_{1400} < 30$ μJy, where S_{1400} is the radio flux density at 1400 MHz. Red triangles are the γ-ray MSPs.

1.3.3 Millisecond pulsars (MSPs)

Besides the canonical pulsar population, ∼10% of the total pulsar population are clustered in the lower left part of Figure 1.3. The temporal behaviour of these pulsars can not be explained by the above picture of a canonical pulsar. Instead, these pulsars have both small periods (of the order of milliseconds) and small spin-downs, $\dot{P} \sim 10^{-20}$ s s^{-1}. The shortest known period is 1.39 ms (716 Hz) of PSR J1748-2446ad which resides in globular cluster Terzan 5 (Hessels et al., 2006). This pulsar population appears to be much older than ordinary pulsars from the characteristic age calculation (equation 1.13). These fast spinning pulsars are called millisecond pulsars (MSPs) as their spin periods are on the order of milliseconds, MSPs represent the oldest population of pulsars with characteristic ages $\sim 10^{10}$ yr.

It is generally accepted that MSPs emerge from canonical pulsars in a binary system which was not disrupted during the supernova explosion. If the companion is sufficiently massive and it evolves into a red giant after the pulsar's emission has ceased, the "dead" pulsar can accrete materials through the Roche lobe from the donor star and obtain angular momentum to spin up again to millisecond periods. That is why they are referred to as being "recycled", because they were spun up to millisecond periods by accretion from a binary companion. A comprehensive review of the recycling process can be found in Bhattacharya & van den Heuvel (1991).

1.3.4 Mildly-recycled pulsars

There is a growing number of mildly-recycled pulsars in the current population, around 30 systems to date, located between the canonical pulsar population and the MSP population on the $P-\dot{P}$ diagram. This new class of pulsars was established by the discovery of three binary pulsars with rather massive companions (Camilo, 1996). Unlike a fully recycled pulsar, which has to go through an extended period in an accretion process involving a low-mass X-ray binary (LMXB) state, mildly recycled pulsars are formed in a different formation scenario. The donor stars for mildly recycled pulsars are more massive, they have gone through either the intermediate-mass X-ray binary (IMXB; $M_{\rm donor}$ 1 - 10 $M_{\rm sun}$) or a high-mass X-ray binary (HMXB; $M_{\rm donor} \geq 10$ $M_{\rm sun}$) phase, which are unstable and inefficient. These accretion phases often result in mildly-recycled pulsars. Unlike fully-recycled MSPs where helium low-mass white dwarf (WD) companions with short spin period (P $<$ 10 ms) and a small spin-down rate ($\dot{P} \leq 10^{-20}$), mildly-recycled pulsars tend to have massive CO/ONeMg WDs companion with $10 < P < 100$ ms and $10^{-20} < \dot{P} < 10^{-18}$. Recent examples of these mildly-recycled pulsars discovered are PSR J1930−1852, PSR J2045+3633 and PSR J2053+4650 (Swiggum et al., 2015; Berezina et al., 2017).

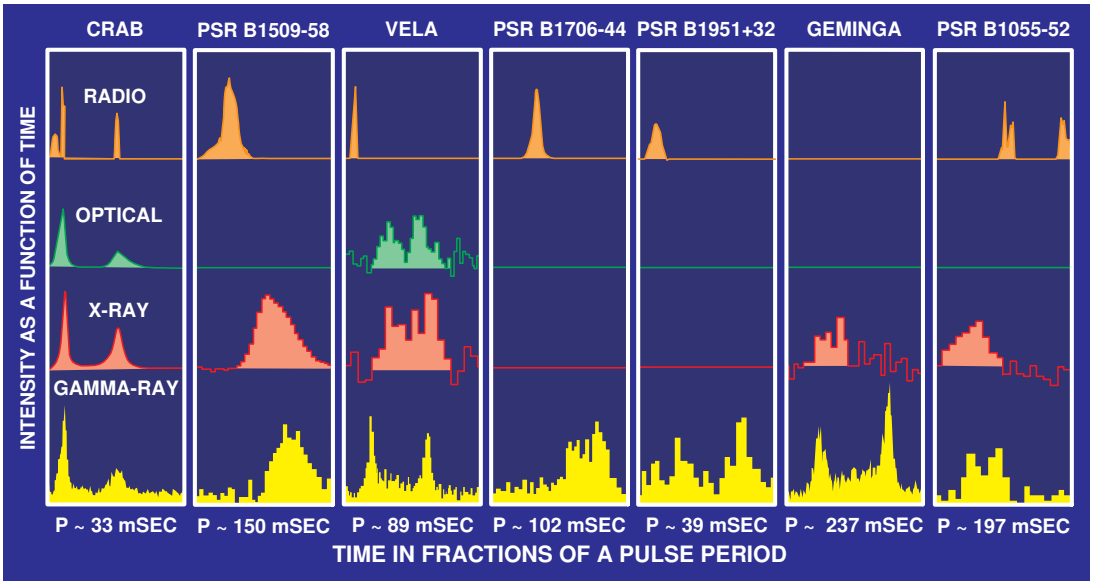

Figure 1.4 Multiwavelength pulse profiles (Radio, Optical, X-ray and γ-ray) of seven γ-ray pulsars detected by EGRET (Thompson, 2004).

1.4 Pulsars in γ-ray

1.4.1 *Fermi*-LAT

Our knowledge of pulsars in the γ-ray energies increased exponentially with the effort from *Fermi*. Before the launch of *Fermi*, only 7 pulsars were known to be pulsating in γ-ray. They were detected by the Energetic Gamma Ray Experiment Telescope (EGRET) as shown in Figure 1.4.

Fermi was launched on June 11, 2008. It has two instruments onboard, the Gamma-ray Burst Monitor (GBM) working in the energy range 150 keV - 30 MeV, and the Large Area Telescope (LAT), covering the energy range below 30 MeV to above 300 GeV. The LAT, as the major instrument of the satellite, consists of an array of 4×4 towers, each composed of a tracker module, a calorimeter module and a data acquisition module (Fig. 1.5). As the successor of the EGRET telescope, the LAT has a much higher sensitivity and better resolution (energy and spatial), as well as a large Field of View (2.4 sr). The effective area of LAT above 1 GeV of $\sim$ 8000 cm^2, which is 5 times of EGRET. A comparison of the LAT and EGRET can be found in Table 1.1. *Fermi* was launched into a low Earth orbit and it operates mainly in survey mode, which covers the entire sky every 3 hours. The LAT has a superb time resolution of less than 10 μs, making it favourable for pulsar observations.

1.4.2 Early discoveries from *Fermi*-LAT

During the early calibration phase, the LAT performed a sequence of test observations toward multiple objects, first the Vela pulsar and then the EGRET unassociated source

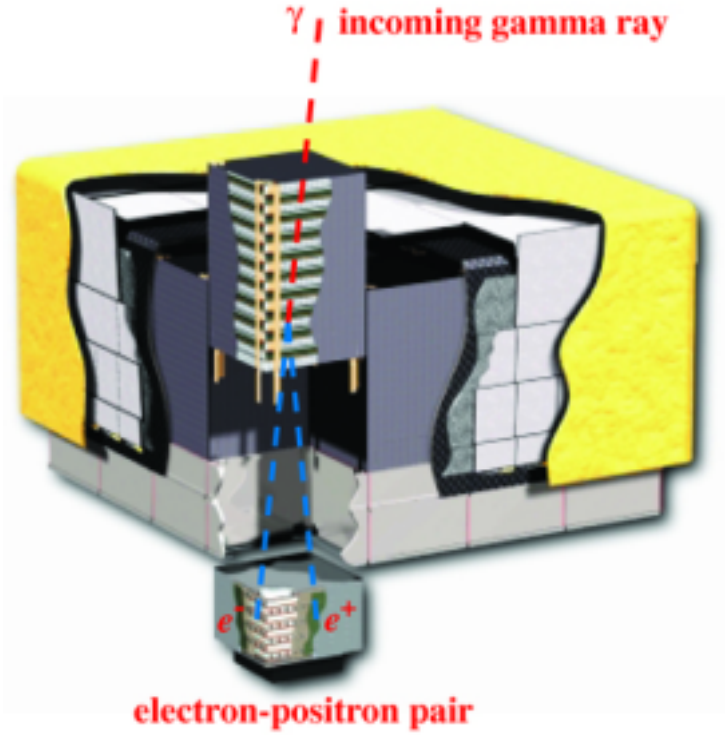

Figure 1.5 Illustration of the Large Area Telescope (LAT) onboard the *Fermi* Gamma-ray Space Telescope. The tracker (dark grey) consists of 18 tungsten converter layers and 16 dual silicon tracker planes. The calorimeter module (light grey) consist of 96 long, narrow CsI scintillators, stacked in an alternating fashion so that the location and the energy of the charged particle can be measured. The tracker is surrounded by the plastic anti-coincidence detector (ACD). The red light shows a γ-ray photon travelling through the tracker and being converted into pairs (blue lines) before entering the calorimeter.

Table 1.1 Comparison of instrument details between EGRET and LAT (Thompson et al., 1993; Atwood et al., 2009).

	EGRET	LAT
Energy Range	20 MeV - 30 GeV	20 MeV - 300 GeV
Energy Resolution	10 %	$<$ 10 %
Peak Effective Area cm^2	1500	$>$ 8000
Field of View	0.5 sr	$>$ 2 sr
Angular Resolution	5.8°(100 MeV)	$<$ 3.5°(100 MeV)
		$<$ 0.15°($>$10 GeV)
Deadtime per Event	100 ms	$<$ 100 μs
Source Location Determination	15′	$<$ 0.5′
Point Source Sensitivity	$\sim$ 10^{-7} cm^{-2} s^{-1}	$<$ 6 $\times$ 10^{-9} cm^{-2} s^{-1}

3EG J0010+7309, associated with the SNR CTA-1. 3EG J0010+7309 was long suspected to be a X-ray/γ-ray pulsar since in the EGRET era in the 90s (Slane et al., 1997). The test observation was able to revealed the long-overdue detection of periodicity from 3EG J0010+7309, making it one of the high-impact pulsar discoveries from *Fermi* (Abdo et al., 2008). The detection of CTA-1 pulsar (now known as PSR J0007+7303) implies that many of the unassociated γ-ray sources could also be pulsars.

Because of the relatively lower surface magnetic fields, hence the low spin-down power, MSPs were thought to be not favourable for producing γ-ray. The detection of the MSP PSR J0030+0451 came as a real surprise (Abdo et al., 2009c). As the *Fermi* mission continuties, surprisingly, MSPs dominated the known γ-ray pulsar population. At time of writing, *Fermi* has already detected more than 100 MSPs, almost half of the γ-ray pulsar population, from either folding γ-ray photons with known radio ephemerides or targeted radio searches on unassociated γ-ray sources.

Besides revealing that MSPs can also emit in γ-rays, the detection of γ-ray emission from the globular cluster 47 Tuc (Abdo et al., 2009b) was also a big surprise. Globular clusters are large spherical collections of stars gravitationally bound to a galaxy's core, are found to host many MSPs (Camilo & Rasio, 2005). As the *Fermi* mission continues, another 20 globular clusters were discovered as point sources (Abdo et al., 2010b; Kong et al., 2010; Tam et al., 2011). Originally, the γ-ray emission from the globular clusters was thought to be from the integrated γ-ray emission from all the γ-ray emitting pulsars within the cluster. The detection of γ-ray pulsations from two globular cluster pulsars in NGC6624 (PSR J1823−3021A) (Freire et al., 2011) and M28 (PSR B1821−24) (Johnson et al., 2013; Wu et al., 2013) implied that the cluster γ-ray flux could be dominated by just one strong γ-ray pulsar, strongly affecting the predicted number of MSPs within the cluster.

1.4.3 γ-ray pulsar population

The observed γ-ray spectra of LAT pulsars can be well described by a power law with an exponential cutoff, similar to what has been found from EGRET (see Figure 1.6 for an example of a pulsar's γ-ray spectrum). Their light curves are usually double peaked (with peak separation of 0.4 - 0.6), but a number of single-peaked pulsars is also present in the current population (see Figure 1.7 for examples of pulsars γ-ray light curves). The γ-ray peaks are usually not aligned with the radio ones with very few exceptions. This confirms early EGRET findings and suggests γ-ray emission regions locate far from the pulsar's surface.

To date, over 200 γ-ray pulsars have been detected by the *Fermi*-LAT in the past eight years of operation. Table 1.2 summarizes the currently known γ-ray pulsar population in different categories. The majority of the detected γ-ray pulsars were previously detected as radio pulsars, either discovered from radio pulsar surveys or targeted radio observations of unassociated LAT sources (see e.g. Barr et al., 2013; Bhattacharyya et al., 2013; Camilo et al., 2012, 2015; Cognard et al., 2011; Cromartie et al., 2016; Guillemot et al., 2012a; Keith et al., 2011; Kerr et al., 2012; Ransom et al., 2011). γ-ray pulsars found with the above methods are naturally radio-loud, with both canonical

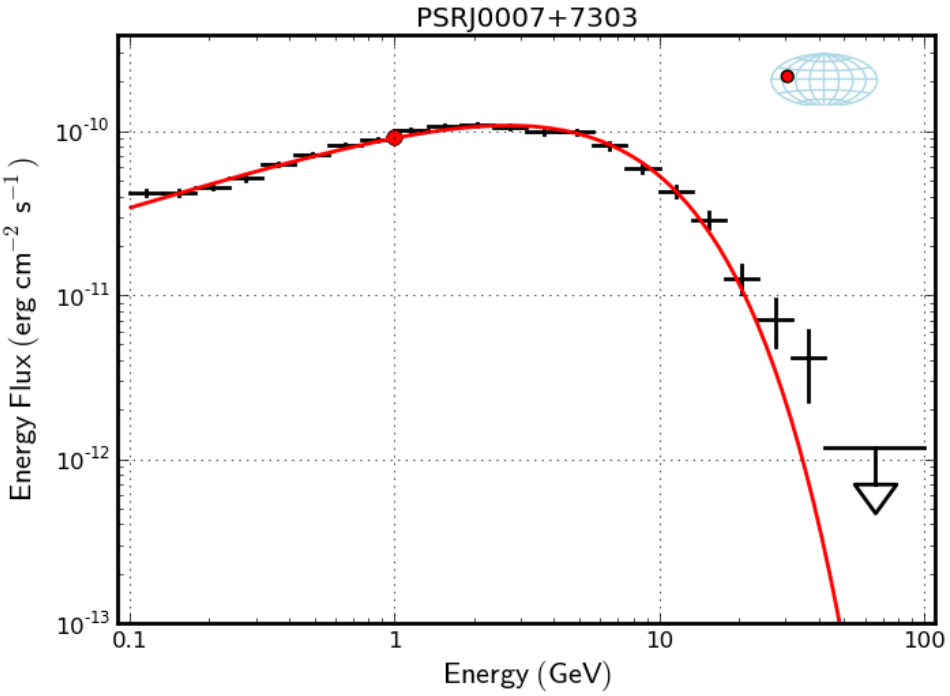

Figure 1.6 γ-ray spectral energy distribution of PSR J0007+7302, the red curve represents the best-fit spectral model PLEC described in Section 2.1.1.

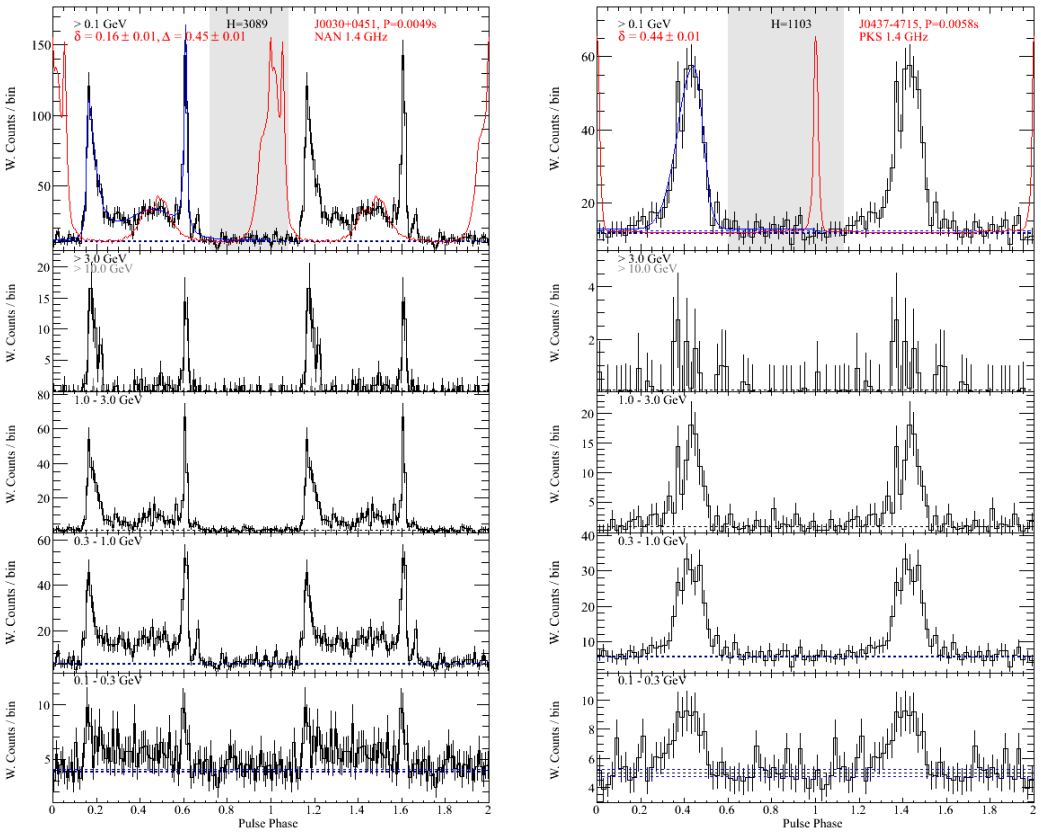

Figure 1.7 γ-ray pulse profiles of PSRs J0030+0451 and J0437−4715 shown in six energy bands (two rotations in phase are shown for clarity). The blue solid line is the best light curve fit, and the red solid line is the 1.4 GHz radio profile (reproduced from Abdo et al., 2013).

Table 1.2 Summary of the pulsar population

Category	Count	Sub-count	Fraction
Known rotational-powered (RPPs)	2694		
RPPs with measured $\dot{P} > 0$		2176	80%
RPPs with measured $\dot{E} > 3 \times 10^{33}$ erg s^{-}1		642	24%
Millisecond pulsars (MSPs, P $<$ 16 ms)	377		
Field MSPs		244	65%
MSPs in globular clusters		133	
Field MSPs with measured $\dot{E} > 3 \times 10^{33}$ erg s^{-1}		126	
Globular cluster MSPs with measured $\dot{E} > 3 \times 10^{33}$ erg s^{-1}		33	
Total known γ-ray pulsar	206		
Young or middle-aged		113	
Radio-loud γ-ray		57	28%
Radio-quiet γ-ray		56	27%
γ-ray MSPs (isolated + binary)		(20+73)=93	45%
Radio MSPs discovered from targeted search in unassoicated LAT sources with γ-ray pulsations	54	52	

pulsars and MSPs.

Another observation from the current γ-ray pulsar population is that all γ-ray MSPs found by *Fermi*-LAT are radio-loud. This is supported by the theory that MSPs have wide radio beams, which are harder to be missed compared to the γ-ray beams (Kramer et al., 1998; Manchester, 2005; Story et al., 2007; Ravi et al., 2010). However, one of the discoveries presented in Chapter 5 may change the above statement.

1.4.4 Blind searches with *Fermi*-LAT data

The remaining fraction of the γ-ray pulsars has been discovered by direct, blind searches of the *Fermi*-LAT data. Unlike from radio pulsars where a radio pulsar could be bright enough to be detected in few seconds, the low photon count makes the detection of γ-ray pulsars a long and challenging process. On average, we detect one γ-ray photon for every few thousand rotations of the pulsar. A detection therefore requires long integration time in order to gather enough pulsed photons.

The typical technique for finding a periodic signal in a dataset is the fast Fourier transform (FFT). A fully coherent FFT becomes memory intensive for lengthy datasets because the number of frequency bins in the FFT increases with the length of the observational time. In addition, pulsars gradually slow down as they radiate away energy, requiring the computation of tens of thousands of FFTs to scan a realistic P and $\dot{P}$ parameter space which makes FFT searches computationally intensive for blind searches in γ-ray.

A time-differencing method was developed that drastically reduced the size of the FFTs and the number of search trials was developed by calculating the differences between photon arrival times within a small window (Atwood et al., 2006; Ziegler et al., 2008). This incoherent technique enables the discovery of 24 γ-ray pulsars. Follow-up radio observations revealed that 21 of them are radio-quiet (Abdo et al., 2009b; Saz

Parkinson et al., 2010).

Pletsch et al. (2012b) extended the search in frequency and rotational spin-down to a 4-dimensional search including the sky position, using the metric formulation to ensure optimal sky coverage. A weighting algorithm (Kerr, 2011) was introduced to assign every photon a probability to reduces the trials previously needed to optimize the extraction region together with the energy range. This results in an enhanced sensitivity to the pulsation detection. This survey using the new photon weighting technique and search algorithm discovered nine more young γ-ray pulsars (Pletsch et al., 2012b). A further extension to search over binary parameters with constraints from optical wavelength resulted in the discovery of MSP PSR J1311−3430 (Pletsch et al., 2012a), the only binary MSP to be found through its γ-ray pulsations so far. Chapter 3 will give a description of the blind search algorithm used in our γ-ray blind search survey.

Even with these new methods, the computational cost of running a blind search increases as the *Fermi* mission continues. These searches become too expensive to run even on a dedicated computing cluster. To meet these computational costs, Pletsch et al. (2013) utilize the distributed volunteer computing system Einstein@Home (Allen et al., 2013). Einstein@Home was originally designed to search for gravitational waves (Abbott et al., 2008), with more than 60,000 currently active computers, Einstein@Home has a sustained computing power of > 2 PFLOP/s, comparable to the world's top 50 supercomputers. In order to search through the full parameter space, thousands of smaller chunks of "work units" are created to cover the full parameter space. These work units were then distributed to participant's computer to perform the actual search. Once the search of that work unit is finished, the result will then be sent back to the server. Four new radio-quiet pulsars were found by first Einstein@Home γ-ray pulsar survey Pletsch et al. (2013).

1.4.5 γ-ray pulsar candidate

Apart from the blind search technique, selecting suitable γ-ray sources for blind periodicity searches is one of the most critical factor for a successful survey. The main strategy to select pulsar candidates from the *Fermi* source catalogs has been revolved around the "pulsarness" of γ-ray sources, a combination of a suitably curved spectral shape and the lack of time variability on a monthly scale. A number of groups have developed different classification schemes using machine learning techniques (Lee et al., 2012; Mirabal et al., 2012; Saz Parkinson et al., 2016). The Third *Fermi* source catalog (3FGL; Acero et al., 2015) provides improved localizations and constrains on the spectral parameters, enabling more precise classification of γ-ray pulsar candidates. In Chapter 2, the method that we used for selecting γ-ray sources for the second Einstein@Home γ-ray blind search survey will be presented.

1.4.6 Radio-quiet fraction

γ-ray pulsars found in blind searches are mostly radio-quiet or have very low radio fluxes. Of those 41 pulsars detected via γ-ray blind searches from previous surveys, only four were detected in follow-up radio observations, as shown in Figure 3 in Abdo et al. (2013). This suggested that there may be a hidden population of radio-quiet γ-ray pulsars or MSPs among the unassociated LAT sources. For a radio-quiet pulsar, the radio beam does not sweep across or barely clips the Earth's line-of-sight. While the radio emission originates near the surface of the neutron star polar caps and extends in a narrow cone, the γ-ray emission originates in the magnetosphere and is spreads out in a wide fan shape (see Section 1.5). Prior to the launch of *Fermi*, Geminga served as the lone example of a radio-quiet γ-ray pulsar (Halpern & Holt, 1992), but this picture has been changed with the addition of many radio-quiet γ-ray pulsars found in γ-ray blind searches. This has a great impact on the theoretical modelling of the beaming fraction. Before *Fermi* was launched, the number of potential radio-quiet and radio-loud young γ-ray pulsars observable by *Fermi*-LAT was estimated to range from being roughly equal, to having a very high radio-quiet fraction (Harding et al., 2002, 2007). The current pulsar population suggests the former scenario, but as the mission continues and more radio-quiet γ-ray pulsars discoveries in blind searches suggests this fraction is subject to change.

1.5 Pulsar emission model

1.5.1 Magnetosphere

From the pulsed γ-ray emission observed up to 10 GeV by ERGET and *Fermi*-LAT, astrophysicists theorize that particles are accelerated to relativistic energies somewhere near the pulsar's surface. According to Faraday's law, a rotating magnetic field will induce an electric field. As proposed by Goldreich & Julian (1969), a very strong electric field induced by the rotating magnetic field (of the order of 10^{12} G) is greater than the gravitational potential and the work function of the material of the neutron star's surface. As a result, charges are striped out from the neutron star's surface and they are accelerated along magnetic field lines, gaining very high Lorentz factors of $10^5 - 10^7$. A plasma sphere filled with charges coming from the neutron star surface is called the magnetosphere which co-rotates with the pulsar.

The dipolar magnetic field lines are divided into two groups by the light cylinder. Magnetic field lines that close within the light cylinder are called closed field lines. The last closed field line defines the boundary of the closed field line region. Outside the closed field line region, field lines remain open as they leave the light cylinder. Charges are forced to co-rotate within the closed field line region, while charges outside the closed field line region flow freely outward as pulsar wind.

Furthermore, plasma within the magnetosphere are able to cancel the electric field parallel to the magnetic field everywhere except at a few locations. These spots (where $\vec{E} \cdot \vec{B} = 0$) are believed to exist above the surface at the magnetic pole and along the

null charge surface ($\vec{\Omega}\cdot\vec{B}=0$), where the sign of the co-rotation charge changes. These are the regions of particle acceleration occur and gives rise to the two major classes of high energy emission models, will be explained in the following sections.

1.5.2 Radiation Processes

Charged particles are accelerated to very high energies under the strong electric potential drop ($> 10^{12}\ V$) induced by the rotating magnetic field. The accelerated charged particles radiate at high energies and at radio frequencies as the combined result of curvature radiation, synchrotron radiation and inverse Compton Scattering.

Synchrotron radiation is produced when a charged particle moves in a magnetic field at relativistic velocities (the non-relativistic version is called cyclotron radiation). Charged particles with a non-zero velocity move along magnetic field lines in a helical path as a combination of circular motion around the magnetic field and the velocity component along the magnetic field. The cyclotron frequency,

$$\omega = \frac{eB}{\gamma m_{\rm e}} \tag{1.20}$$

describes the frequency of the circular orbit for a Lorentz factor $\gamma = \left(1-\left(\frac{v}{c}\right)^2\right)^{-1/2}$ (where v is the velocity) and the magnetic field strength B. For non-relativistic particles, the emission frequency is simply $2\pi\omega$, thus the spectrum consists of a single line. On the contrary, the characteristic frequency of emission is the critical frequency in the relativistic case

$$\nu_{\rm crit} = \frac{3\gamma^2 eB}{2m_{\rm e}} \tag{1.21}$$

for an electron. Above $\nu_{\rm crit}$, the spectrum is exponentially suppressed, the overall spectrum consists of a sum of cyclotron harmonics, which often peaks in the X-ray for typical neutron star magnetic field.

If the charged particle is moving in curved magnetic fields, curvature radiation is produced. The production of synchrotron radiation is due to the transverse motion of the charged particle in the magnetic field while the curvature radiation is due to the parallel component of the motion. The characteristic frequency of curvature radiation is obtained by replacing the radius of the gyration in synchrotron radiation r, given by

$$r = \frac{\beta c\gamma m_{\rm e}}{eB}, \tag{1.22}$$

with the radius of curvature $r_{\rm curvature}$ of magnetic field lines. This gives a critical frequency

$$\nu_{\rm crit} \sim \frac{\gamma^3 c}{r_{\rm curvature}}. \tag{1.23}$$

Assuming a dipolar field and an electron Lorentz factor of 10^7 (corresponding to TeV energies), γ-rays with energies in the range of few GeV can be generated by curvature

radiation.

Inverse Compton scattering is equivalent to the well-known Compton scattering process with a Lorentz boost. In this case, the electron is moving and energy is transferred to the photon. The mean photon energy after collision is found to increase with the squared of the electron Lorentz factor. Therefore, high frequency radio photons interacting with relativistic electrons with Lorentz factor $\gamma = 10^3 - 10^4$ are boosted up to X-ray energies. The photon energy boost is limited by the incident electron energy. However, assuming very high electron Lorentz factors, it is highly probable to obtain high energy γ-rays in the TeV energy range. A full treatment of the problem yields the Klein-Nishina formula for the scattering cross-section. This holds for all energies, while the Thompson cross-section can only be applied to photon energies below $\approx m_e c^2$.

1.5.3 Radio emission

The open field lines define a region called the polar cap on the neutron star surface, centred at the magnetic pole on the neutron star surface. The boundary of the polar cap is defined by the last open field line tangential to the light cylinder. Electrons in the polar cap are magnetically accelerated along the curved open field lines to very high energies, emitting curvature radiation. High-energy photons produced by curvature radiation interact with the strong magnetic field and lower-energy photons to produce electron-positron pairs that radiate more high-energy photons. The final result of this cascade process are bunches of charged particles that emit at radio wavelengths. The radio emission should form a cone centered on the magnetic axis. Depending on the cone structure (nested cone or patchy beam structure) and the line of sight, different number of radio pulse components can be observed. A detailed review of the radio emission mechanisms can be found in (Graham-Smith, 2003).

1.5.4 Models for γ-ray emission

The discovery of high energy emission from pulsars has provided evidence for non-thermal radiation from the magnetosphere. As mentioned in Section 1.2.2, high energy emission from pulsars can account for a large fraction of the rotational energy, while emission in the radio band contributes no more than 0.001% of the spin down power (see Figure 1.1). The existence of high energy emission implies a very efficient particle acceleration mechanism in the magnetosphere.

Several high energy emission and particle acceleration models have been proposed in the last few decades. They are roughly classified into three categories based on the location of the accelerator. Different emission regions are illustrated in Figure 1.8, with Polar Cap model being the closest to the neutron star surface, followed by the Slot Gap and the Outer Gap at larger distances from the neutron star surface. Note that the Polar Cap model has several difficulties in explaining the high energy γ-ray emission seen by *Fermi*-LAT. The emission pattern of the Polar Cap model predicts a near phase alignment of the radio and γ-ray profile, which failed to reproduce the widely separated γ-ray peaks profile observed by *Fermi*-LAT. Also the spectrum of

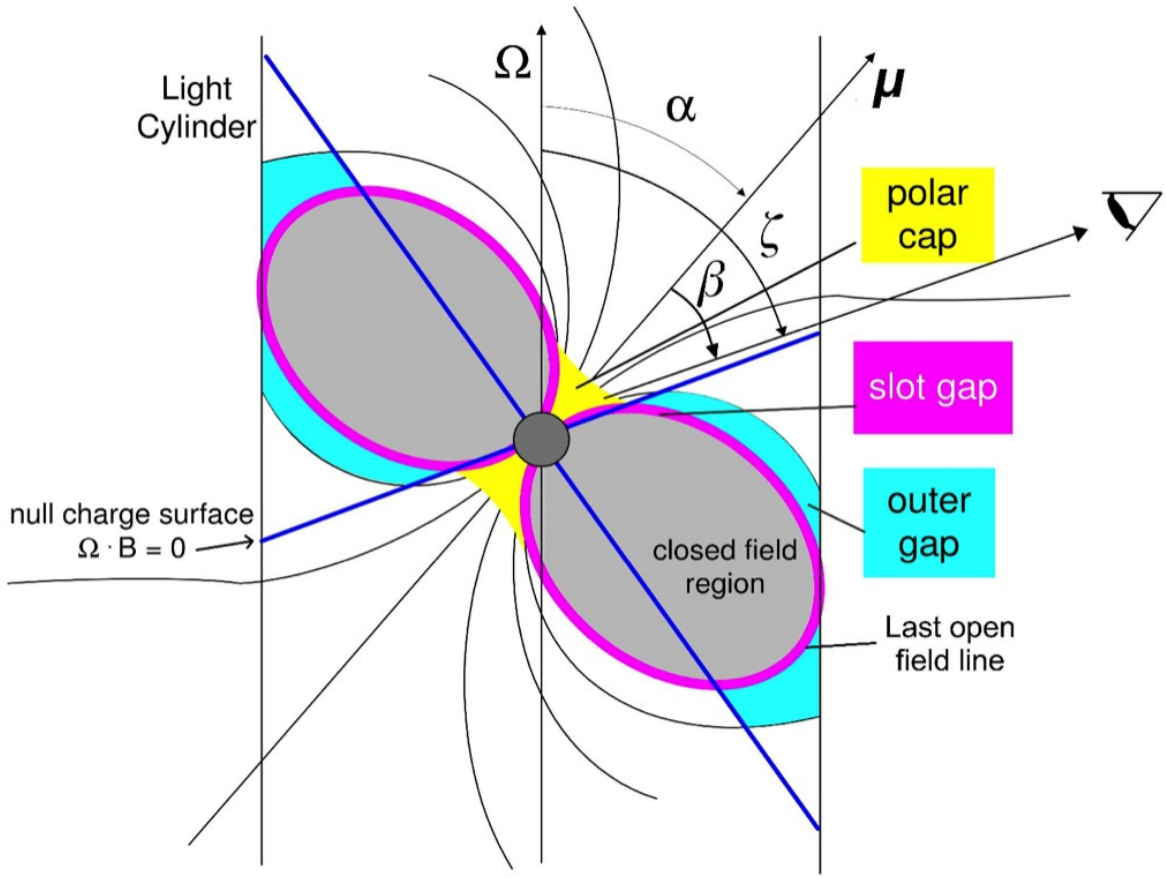

Figure 1.8 A schematic representation of the different geometric pulsar emission models. The Polar Cap model in yellow, the Slot Gap & Two-pole Caustic emission region in magenta, the Outer Gap region in cyan. The null charge surfaces are indicated by the dark blue lines. α is the inclination angle, the angle between the rotation ($\boldsymbol{\Omega}$) and magnetic axes ($\boldsymbol{\mu}$), $\boldsymbol{\zeta}$ is the angle between observer's line of sight and the rotation axis, and the impact angle ($\boldsymbol{\beta} \equiv |\boldsymbol{\zeta} - \boldsymbol{\alpha}|$). This figure is reproduced from Breed et al. (2015).

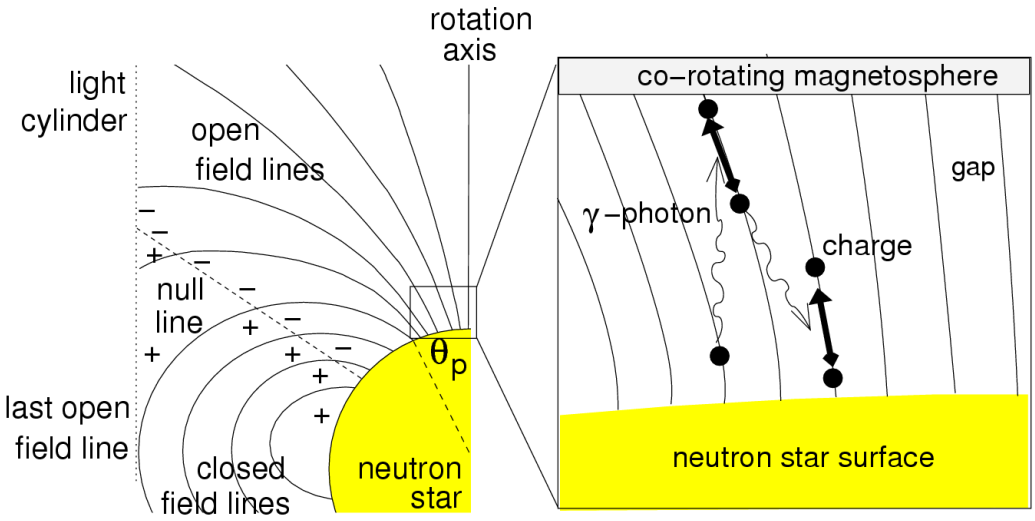

Figure 1.9 Schematic diagram of the pulsar magnetosphere. The zoom-in image illustrate the pair-creation cascades in the polar cap region as described in Section 1.5.1. (Lorimer & Kramer, 2005)

γ-ray photons generated from the polar cap region is expected to be relatively hard, and with a sharp cutoff faster than exponential cutoff due to the attenuation from one-photon pair creation (Harding, 2009), which was not observed in the current γ-ray pulsar population (Abdo et al., 2010a).

1.5.4.1 Slot gap and Two-pole Caustic models

The Slot Gap (SG) model (Muslimov & Harding, 2003, 2004a) is an extension of the polar cap model, in which the low-altitude acceleration region at the rim of the polar cap extends to higher altitude bounded by the the last open field line and the boundary of the pair plasma column. The low-altitude cascade in field lines within the slot gap will produce a narrow beam of high-energy emission while the high-altitude cascade above the interior edge of the slot gap will produce a broader hollow cone beam.

The Two-Pole Caustic (TPC) model (Dyks & Rudak, 2003) is a geometric realization of the SG model. In this model, the acceleration gap, which extends from each polar cap to the light cylinder, is thin and confined by the last open field line.

1.5.4.2 Outer gap model

In the Outer Gap (OG) model (see e.g. Cheng et al., 1986; Takata et al., 2010), the acceleration gap is located along the last closed field line between the “null charge" surface (where $\vec{\Omega}\cdot\vec{B}=0$) and the light cylinder (see Figure 1.5.4.2). Curvature or inverse Compton radiation are produced by accelerated primary particles along the magnetic field, and secondary electron-positron pairs are created when the γ-ray photons go

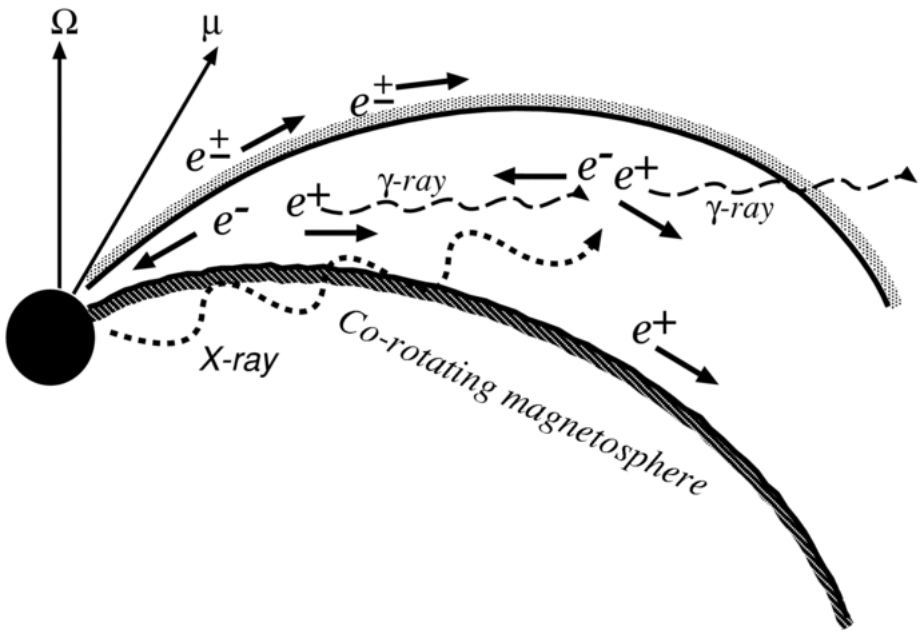

Figure 1.10 Schematic view of the outer gap accelerator as described in Section 1.5.4.2. The photon-photon pair-creation process in the outer magnetosphere produces the pairs in the gap uniformly. The pairs created by the magnetic pair-creation process further emit high energy photons via curvature radiation or inverse Compton scatters X-ray photons coming from the neutron star surface (Takata et al., 2010).

through a dense photon field the via photon-photon interaction ($\gamma + \gamma \rightarrow e^+ + e^-$). These pairs further emit high energy emission via Curvature radiation. In contrast to the polar cap model, the outer gap model predicts fan-like γ-ray beams. Thus, the outer gap model can easily predict typical γ-ray light curves with widely separated double peaks and "bridge" structures between two γ-ray peaks as seen from many pulsars.

1.5.4.3 Pair-starved Polar Cap model

First proposed by Muslimov & Harding (2004b), the development of the Pair-starved Polar Cap (PSPC) model is to serve as a possible γ-ray emission model for low-$\dot{E}$ pulsars. In which pair-production may be insufficient to screen the accelerating electric field. Thus allowing particles to be further accelerated to altitudes near the light cylinder, emitting curvature radiation. Muslimov & Harding (2004b) demonstrated that it is possible to accelerate particles to sufficiently high energies for production of γ-rays in this model.

It should be noted that the absence of narrow gaps will, generally, lead to much broader peaks with γ-ray features leading the radio as demonstrated by Venter et al. (2009).

1.5.4.4 Striped Wind model

The Striped Wind model (Coroniti, 1990; Pétri, 2012) is significantly different from all the previously described gap models. In this model, pairs are created in the magnetosphere and cool down before reaching the striped pulsar wind zone. In the pulsar wind zone, the magnetic field in the striped pulsar wind serves as an alternate energy reservoir via various magnetic reconnection processes. Therefore, the pulsar's spin-down power $\dot{E}$ is not the unique energy source of the accelerated particles. This means the observed γ-ray luminosity could exceed the spin-down power. γ-ray emission is due to synchrotron radiation from particles in the striped wind, thus well outside the magnetosphere, but not curvature radiation in the open field line region. This model is able to explain LAT pulsars with high γ-ray efficiency and reproduce the spectral index and γ-ray luminosity of the known γ-ray pulsar population (Pétri, 2012).

1.5.5 Mapping Emission Geometry

The pulse profile is the emission pattern observed over one pulsar rotation. By modelling the pulse profile, one can reveal the pulsar's orientation and constrain different γ-ray and radio emission models. The viewing geometry of a pulsar is defined by two angles, the magnetic inclination angle, α, and the angle between the observer's line-of-sight and the rotation axis, ζ. In general, it is possible to reproduce almost any light curve using some combination of model parameters and viewing geometry. Therefore it is very important to use all available information (i.e. radio and γ-ray) to restrict the parameter space and thus test the emission models.

The shape of the pulse profile depends on α, ζ and the emission model assumed. Different combinations of α and ζ will resulted in different pulse profiles, or even no

pulsed radio or γ-ray emission if none of the emission beams cross our line-of-sight. If we assume an emission model (e.g. TPC, OG and SG), one can simulate skymaps for both γ-ray and radio emissions, then we can extract the simulated light curve from the skymap for any given α and ζ. By comparing the observed light curve with the simulated light curve, a set of best-fit parameters (α, ζ) can be obtained. An example of simulated skymaps and light curves of a γ-ray pulsar (PSR J1823−3021A) using the so-called "altitude-limited" emission models are shown in Figure 1.11 and 1.12. A more detailed explanation of pulse profile modelling can be find in Johnson et al. (2014).

1.6 Scope and structure of this thesis

In this chapter, the current understanding of pulsars, especially on the development of γ-ray pulsar astrophysics is summarized. The main scopes of my PhD thesis were to identify pulsar-like γ-ray sources through their γ-ray properties, and to prepare the necessary dataset with the photon weight for the γ-ray blind search survey on the distributed volunteer computing system, Einstein@Home. In Chapter 2, the fundamentals of LAT data analysis and the details of selecting pulsar candidate using a machine learning algorithm will be presented. In Chapter 3, I outline the procedures to detect a pulsar in radio or γ-ray. In Chapter 4, I present the main results of the Einstein@Home γ-ray pulsar blind search survey. Chapter 5 highlights the results of 4 γ-ray pulsars found in the same survey. In Chapter 6, a targeted radio pulsar survey on unassoicated *Fermi*-LAT sources will also be presented. In Chapter 7, a summary of the thesis and the outlook of the field will be presented.

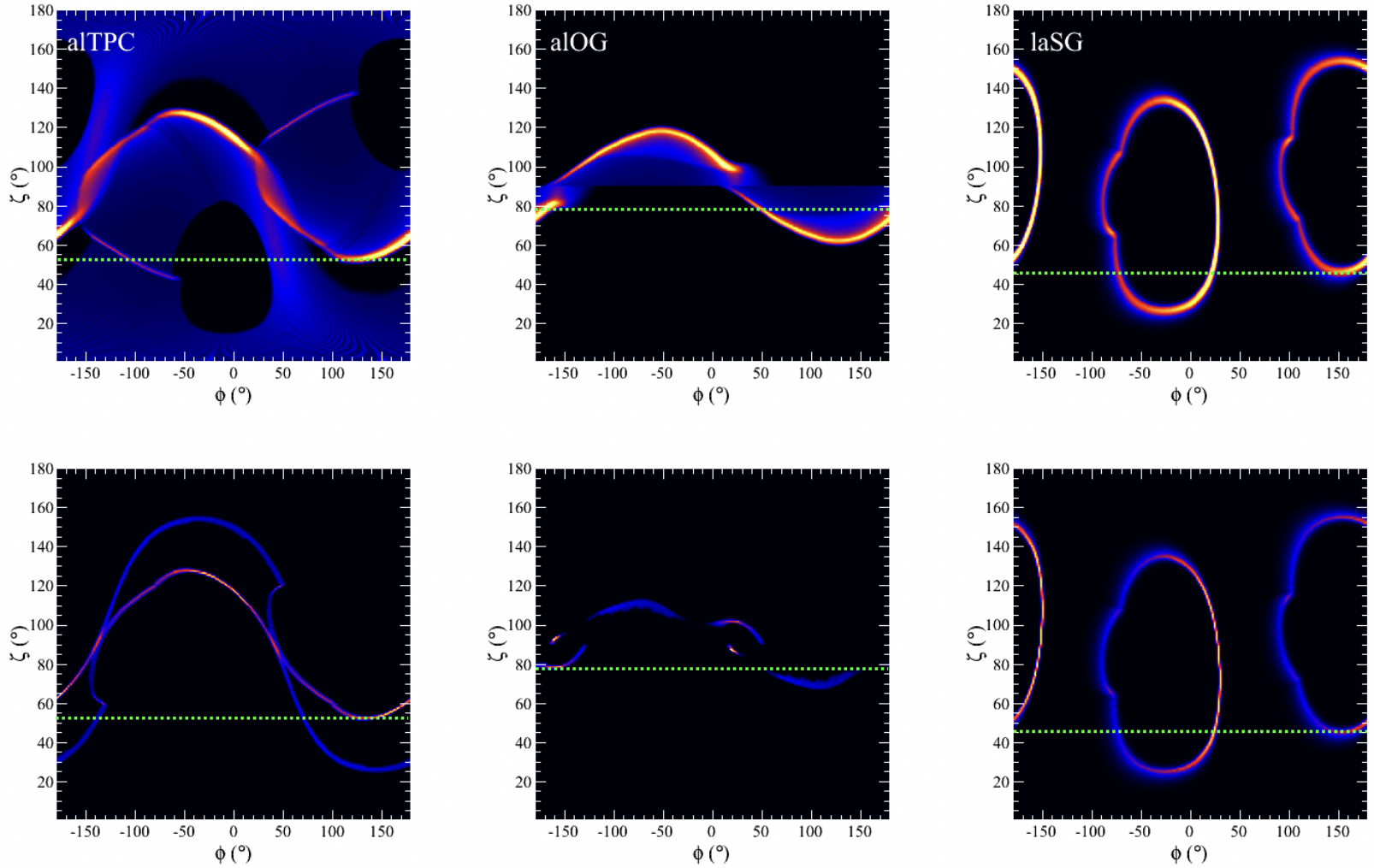

Figure 1.11 Simulated γ-ray (top) and radio (bottom) emission skymaps for PSR J1823−3021A fit with the altitude limited TPC model (alTPC) (left, α=46°), altitude limited OG model (alOG) (middle, α=42°), and low-altitude SG model (laSG) (right, α=78°) models are shown. The green dashed line in each panel denotes the best-fit ζ. The colour scale increases from black to blue to red to yellow to white. This figure is adopted from Johnson et al. (2014).

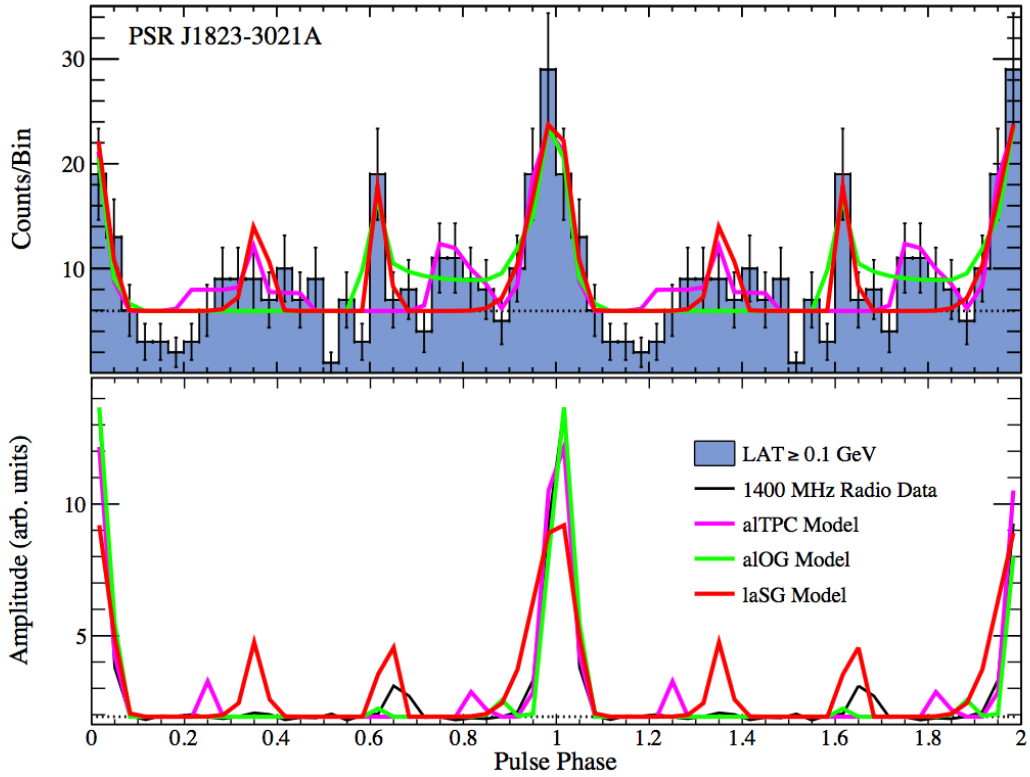

Figure 1.12 Best-fit γ-ray (top) and radio (bottom) light curves for PSR J1823−3021A, the solid green dashed line is the alOG model, and the solid pink line is the alTPC model, and the dash-dot, solid red line is the laSG model. This figure is adopted from Johnson et al. (2014).

Chapter 2

γ-ray "informatics"

Contents

In last chapter, I summarized the current understanding of pulsar, especially in the γ-ray regime - the population, observations, blind searches and emission models. In this chapter, the fundamentals of LAT data analysis using the *Fermi* Science Tools and the *Pointlike* package will be will also be present. discussed. The *Fermi* LAT Source Catalogs, which utilized the same LAT data analysis method described in this chapter, provided the necessary spectral, temporal and flux information for selecting pulsar candidates in our blind search survey (Chapters 4 and 5). The details of selecting pulsar candidate using a machine learning algorithm and the analysis pipeline for the blind search data preparation used in our γ-ray blind search survey will also be presented.

2.1 *Fermi* LAT data challenge

The *Fermi*-LAT is a pair-conversion telescope, which means when γ-ray photons hit the detector, they produce electron-positron pairs. Every time these charged particles produce ionization in the detector, they get counted as an "event". Information such as the position and the energy of the incident γ-ray photon can be reconstructed using the electron-positron path and energy deposition within the tracker and the calorimeter.

The LAT's angular resolution is limited by multiple scattering and bremsstrahlung. Multiple scattering, the effect of which is inversely proportional to the energy (E) (i.e. $1/E$), dominates the uncertainty in direction at lower γ-ray energies. This results in the LAT's energy-dependent point spread function (PSF) that must be taken into account in all analyses.

The efficiency of successful reconstruction of an incident photon and the dispersion distribution of its true observables can be characterized by the instrument response

function (IRF). The efficiency or the effective area, denoted as $\varepsilon(E, t, \vec{\Omega})$, is a function of energy, time and solid angle. Count rate in $\mathrm{d}E \times \mathrm{d}t \times \mathrm{d}\Omega$ can be obtained by multiplying the effective area by the flux density $\mathcal{F}$.

The dispersion matrix $P(E', t', \vec{\Omega}'|E, t, \vec{\Omega})$, is the probability of a photon with true energy E, position $\vec{\Omega}$ and time of arrival t, having a reconstructed energy E', a reconstructed direction $\vec{\Omega}'$ at a time t'. The dispersion matrix is a true probability density function and is normalized such that

$$\int\int\int \mathrm{d}E\ \mathrm{d}\vec{\Omega}\ \mathrm{d}t\mathcal{F}(E', t', \vec{\Omega}'|E, t, \vec{\Omega}) = 1. \tag{2.1}$$

The expected event rate τ in an infinitesimal bin is reconstructed to have an energy E' at a position Ω' and at a time $t^{'}$:

$$\tau(E', \vec{\Omega}', t'|\lambda) = \int\int\int \mathrm{d}E\ \mathrm{d}\vec{\Omega}\ \mathrm{d}t\mathcal{F}(E', t', \vec{\Omega}|\lambda)\varepsilon(E, t, \vec{\Omega})P(E', t', \vec{\Omega}'|E, t, \vec{\Omega}). \tag{2.2}$$

This integration is performed over all energies, solid angles and times.

The dispersion $P(E', t', \vec{\Omega}'|E, t, \vec{\Omega})$ can be simplified if we assume that the energy, spatial and temporal dispersion are not coupled. We can rewrite the dispersion into the following form:

$$P(E', t', \vec{\Omega}'|E, t, \vec{\Omega}) = \mathrm{PSF}(\vec{\Omega}'|E, \vec{\Omega})E_{\mathrm{disp}}(E'|E)T_{\mathrm{disp}}(t'|t). \tag{2.3}$$

The probability density of having a reconstructed position $\vec{\Omega}'$ given the real position of the incoming γ-ray $\vec{\Omega}$ is denoted as $\mathrm{PSF}(\vec{\Omega}'|E, \vec{\Omega})$. As mentioned previously, the PSF of LAT is a strong function of energy, as shown in Figure 2.1.

To evaluate the LAT response, a dedicated Monte Carlo simulation was performed by the instrument team (Atwood et al., 2009; Ackermann et al., 2012). A large number of γ-ray events are simulated in order to cover all possible photon inclination angles and energies with good statistics. This is based on the best available representation of the physical interactions, the instrument, and the on-board and ground processing to produce event classes (see Atwood et al., 2013).

2.1.1 Maximum-Likelihood Analysis of γ-ray data

Maximum-likelihood analysis is commonly used to analyse high energy astronomical data. The method was first introduced by Fisher (1925). Mattox et al. (1996) described the maximum-likelihood analysis framework to analyse EGERT data, from which the likelihood analysis of LAT data is built upon.

The likelihood $\mathcal{L}$ is the probability of obtaining the observed data, for a given set of model parameters:

$$\mathcal{L} = P(\mathrm{data}|\mathrm{model}). \tag{2.4}$$

For example, a model of the γ-ray sky contains a list of parameters λ. The likelihood function can be written as:

$$\mathcal{L} = \mathcal{L}(\lambda). \tag{2.5}$$

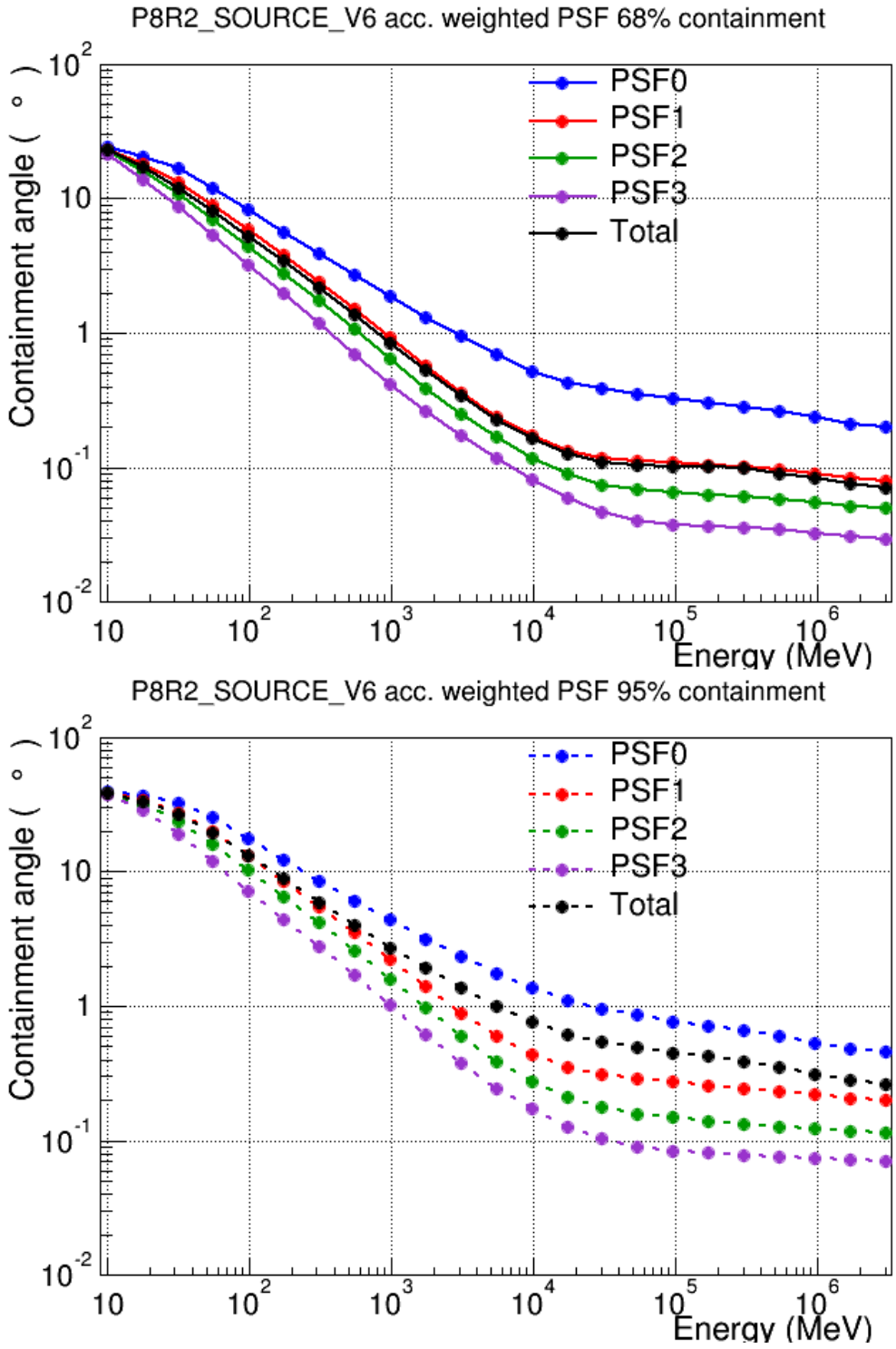

Figure 2.1 LAT 68% and 95% containment angles of the acceptance weighted (acc. weighted) PSF for both the front/back and PSF event types as a function of energy. PSF event type (PSF0/PSF1/PSF2/PSF3) indicate the quality of the reconstructed direction, the data is divided into quartiles, from the lowest quality quartile (PSF0) to the best quality quartile (PSF3) (see http://www.slac.stanford.edu/exp/glast/groups/canda/lat_Performance.html).

As the name suggests, the goal of the maximum-likelihood analysis is to obtain a set of parameters which gives the maximum likelihood value.

$$\lambda_{\rm max} = \arg \max_{\lambda} \mathcal{L}(\lambda). \tag{2.6}$$

The Test Statistic (TS) is defined as

$$\mathrm{TS} = -2\log(\mathcal{L}_{\rm max,0}/\mathcal{L}_{\rm max,1}), \tag{2.7}$$

where $\mathcal{L}_{\rm max,1}$ is the maximum likelihood value for a model with the additional γ-ray source at a specified location and $\mathcal{L}_{\rm max,0}$ is the maximum likelihood value for a model without an additional source (the "null hypothesis").

In the limit of a large number of counts, Wilks' theorem (Wilks, 1938) states that the TS for the null hypothesis is asymptotically distributed as $\chi^2_{\rm n}$, where n is the number of parameters characterizing the additional source. The square root of the TS is approximately equal to the detection significance for a given source.

In general, a model of the sky is composed of a set of sources, each source is characterized by its photon flux density $\mathcal{F}(E, t, \vec{\Omega}|\lambda)$ in terms of energy, time and position in the sky. The source model can be rewritten if the spatial and spectral part can be separated and are time independent,

$$\mathcal{F}(E, t, \vec{\Omega}|\lambda) = \frac{\mathrm{d}N}{\mathrm{d}E} \times \mathrm{PDF}(\Omega), \tag{2.8}$$

where $\mathrm{d}N/\mathrm{d}E$ is a function of energy and $\mathrm{PDF}(\Omega)$ is a function of position ($\vec{\Omega}$). The spectral part is described by dN/dE, a function of energy, which is modelled by simple mathematical functions. The simplest spectral model is a power law (PL) model:

$$\frac{\mathrm{d}N}{\mathrm{d}E} = N_0 \left(\frac{E}{E_0}\right)^{-\gamma}, \tag{2.9}$$

where N_0 and γ are the prefactor and the spectral index respectively, and E_0 is the energy scale or pivot energy which is often fixed since it is coupled with N_0.

A power-law with an exponentially cutoff (PLEC) model is mainly used to model γ-ray emission from pulsars:

$$\frac{\mathrm{d}N}{\mathrm{d}E} = N_0 \left(\frac{E}{E_0}\right)^{-\gamma} \exp\left(-\frac{E}{E_c}\right), \tag{2.10}$$

where $E_{\rm c}$ is the cutoff energy, beyond $E_{\rm c}$ the PLEC spectrum decreases exponentially.

For most of the LAT analysis, binned likelihood analysis is the preferred method to process long time-baseline data with bright background sources. In binned likelihood analysis, reconstructed events are binned in both position and energy. The number of photons in each bin is small and so the distribution is characterized by Poissonian statistic. The probability of a number of events in a given pixel is given by,

$$p_i = \frac{\theta_i^{n_i} e^{-\theta_i}}{n_i!}, \tag{2.11}$$

where n_i refers to the number of observed counts in pixel i and θ_i refers to the number of predicted counts in pixel i.

The likelihood for the model is the product of the probabilities for all pixels,

$$\mathcal{L} = \prod_i p_i. \tag{2.12}$$

The logarithm of the likelihood function takes the following form:

$$\log\mathcal{L} = \sum n_i \log(\theta_i) - \sum \theta_i - \sum \log(n_i!), \tag{2.13}$$

where the first term is an arbitrary additive constant, the second term is the total number of predicted counts and the third term is the model independent term. The log of the likelihood is often used because it changes less rapidly and the likelihood is additive, so that maximizing or calculating the change in the likelihood is easier.

2.1.2 *Fermi* Science-tools and the *Pointlike* package

To perform likelihood analysis on LAT data, *Fermi* Science-tools and the *Pointlike* package are often used. In the standard *Fermi* science tools, **gtselect** performs selection cuts on event data files; **gtbin** bins LAT events in position, time and energy based on user-specified cuts; **gtltcube** and **gtexpcube2** are used to compute the exposure for different energies based on the integrated lifetime according to the spacecraft position history; **gtsrcmap** convolves the source model components with the IRF; **gtdiffrsp** calculates the integral over the solid angle of a diffuse source model convolved with the IRF; **gtlike** performs unbinned or binned likelihood analysis of LAT data and **gttsmaps** calculates test-statistic map for source localization and detection. **gtsrcprob** computes source component probabilities for event data, which is used for the periodicity test (the details of the photon probabilities calculation will be discussed in Section 3.2.1). A summary of the *Fermi* Science-tools are presented in Figure 2.2.

If the analysis requires multiple iterations such as source finding, localization and computing large residual TS maps, the *Pointlike* package is often used. In the Science-tools framework, a uniform bin size for sky position is used for all energies, but the PSF of LAT is not uniform. At low energies, a large number of photons are expected to be found in each pixel but each photon is not very significant due to the poor angular resolution. At high energies, the number of photons is very limited but each is very significant as the angular resolution is much better at those energies. Making use of the fact that the LAT PSF is changing across energies, *Pointlike* scales the bin size so the bin size is always comparable to the PSF. At low energies, *Pointlike* is basically performing a binned likelihood analysis with larger bins while at high energies an unbinned likelihood analysis is performed. This adaptive bin sizing scheme gives a huge boost in efficiency. More details of the implementation of *Pointlike* can be found

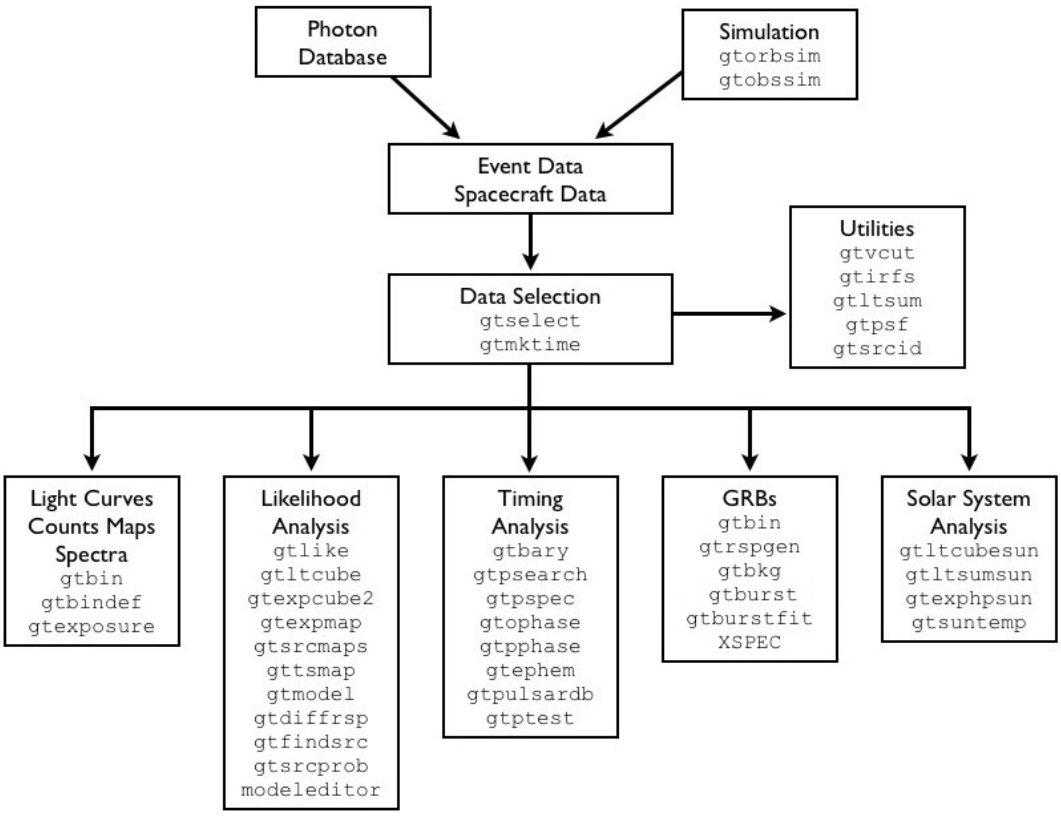

Figure 2.2 The general analysis flow using *Fermi* Science-tools is illustrated. Credit: NASA FSSC.

in Kerr (2010).

2.2 *Fermi* LAT Source Catalogs (0, 1, 2, 3-FGL)

Similar to all other space telescopes, *Fermi* has its own catalogs for sources. The LAT 4-year Point Source Catalog (hereafter 3FGL, Acero et al., 2015), which is the latest edition of the point source catalog, lists the properties of 3033 γ-ray sources detected (TS $>$ 25) by the LAT in the first four years of data taking. The 3FGL catalog is the successor to the previous point source catalogs which covered the first 3, 11 and 24 months of LAT data respectively (Abdo et al., 2009a, 2010a; Nolan et al., 2012).

γ-ray sources in the 3FGL catalog are categorized into different classes. Table 2.1 shows the breakdown of all the classes and Figure 2.3 shows the distribution of all the classified sources in the sky. The majority of the γ-ray sources are associated primarily with positional coincidence with known multi-wavelength counterparts, while some of them have firm identification through its correlated variability, angular extent or pulsation. The remaining 1010 sources (33.3 %), are unassociated.

Besides typical parameters such as positional errors and fluxes, the 3FGL catalog also lists sources' variability and spectral characteristics which are useful for source classification. These topics will be discussed in the following section.

2.3 Selecting pulsar candidates

From the currently known pulsar population, we have learned that γ-ray pulsars fluxes show no time variability (with the exception of PSR J2021+4026, Allafort et al., 2013) in general low in time variability, with a curved spectrum due to the shape of curvature radiation. There are two measurements in the 3FGL catalog to quantify these characteristics: *Curvature TS* and *Variability Index*. The *Curvature TS* represents the curviness of a given source when comparing the change of the likelihood. The *Variability Index* is the measurement of the source's variability on a monthly scale. The detailed explanations of these two parameters can be found from Acero et al. (2015). Figure 2.4 shows the monthly light curve and spectral energy distribution for a pulsar and a blazar in γ-ray, where they show very different temporal and spectral behaviours. Figure 2.5 shows the distribution of sources in *Variability Index* against *Curvature TS*: two distinct groups can be clearly identified in the figure, one is the pulsar population with low variability and curved spectrum, and the other one is the AGN population where high variability and flat spectrum are observed. Figure 2.4 shows two examples of the monthly fluxes and spectral energy distribution of a pulsar and an AGN.

Although using *Variability Index* and *Curvature TS* may seem good enough to identify pulsar candidates, Lee et al. (2012) pointed out that extra care needs to be taken as these two parameters are correlated with the detection significance of individual sources. A number of groups have developed different classification schemes using machine learning techniques (Lee et al., 2012; Mirabal et al., 2012; Saz Parkinson et al., 2016). In particular, Lee et al. (2012) have shown that including the γ-ray flux

Table 2.1 3FGL Source Classes

Description	Identified		Associated	
	Designator	Number	Designator	Number
Pulsar, identified by PSR pulsations	PSR	143	...	...
Pulsar, no pulsations seen in LAT yet	...	...	psr	24
Pulsar wind nebula	PWN	9	pwn	2
Supernova remnant	SNR	12	snr	11
Supernova remnant/pulsar wind nebular	...	...	spp	49
Globular cluster	GLC	0	glc	15
High-mass binary	HMB	3	hmb	0
Binary	BIN	1	bin	0
Nova	NOV	1	nov	0
Star-forming region	SFR	1	sfr	0
Compact steep spectrum quasar	CSS	0	css	1
BL Lac type of blazar	BLL	18	bll	642
FSRQ type of blazar	FSRQ	38	fsrq	446
Non-blazar active galaxy	AGN	0	agn	3
Radio galaxy	RDG	3	rdg	12
Seyfert galaxy	SEY	0	sey	1
Blazar candidate of uncertain type	BCU	5	bcu	568
Normal galaxy (or part)	GAL	2	gal	1
Starburst galaxy	SBG	0	sbg	4
Narrow-line Seyfert 1	NLSY1	2	nlsy1	3
Soft-spectrum radio quasar	SSRQ	0	ssrq	3
Total	...	238	...	1785
Unassociated	...	...	...	1010

Note: The designation "spp" indicates potential association with SNR or PWN. Designations shown in capital letters are firm identifications; lowercase letters indicate associations. In the case of AGNs, many of the associations have high confidence level (Acero et al., 2015).

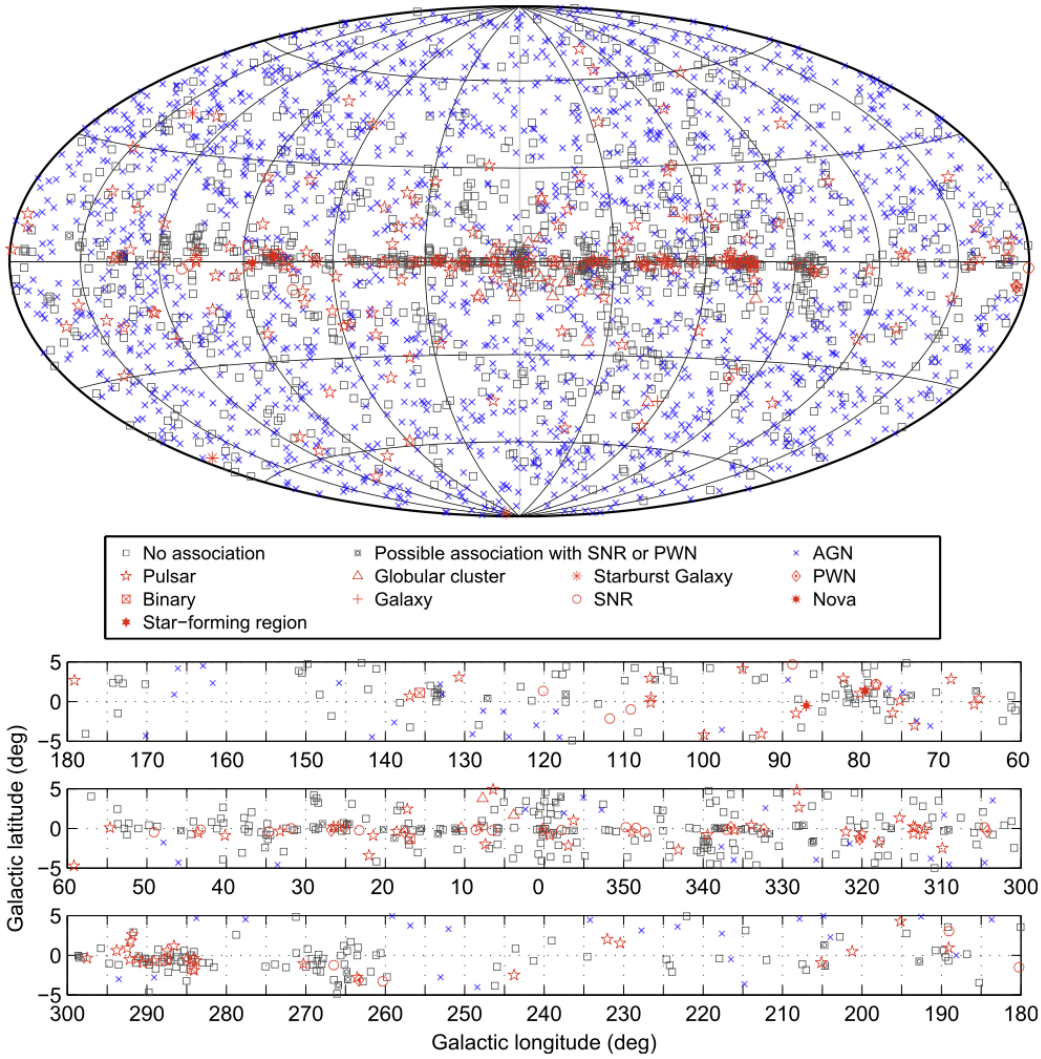

Figure 2.3 Full sky map (top) and zoomed in version of the inner Galactic region (bottom) showing their source classes (see Table 2.1). All AGN classes are plotted with the same symbol for simplicity (Acero et al., 2015).

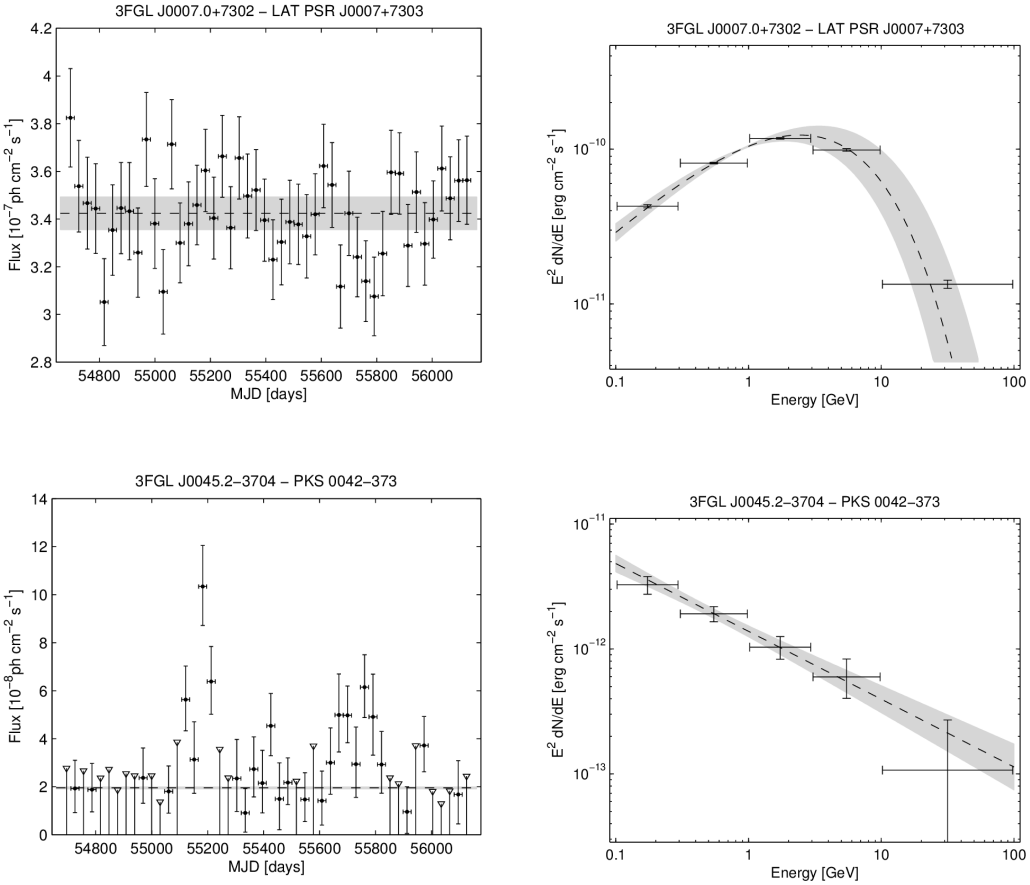

Figure 2.4 Upper left, upper right: monthly fluxes and spectral energy distribution for γ-ray pulsar 3FGL J0007.0+7302. Lower left, lower right: monthly fluxes and spectral energy distribution for γ-ray blazar 3FGL J0045.2−3704 (Acero et al., 2015).

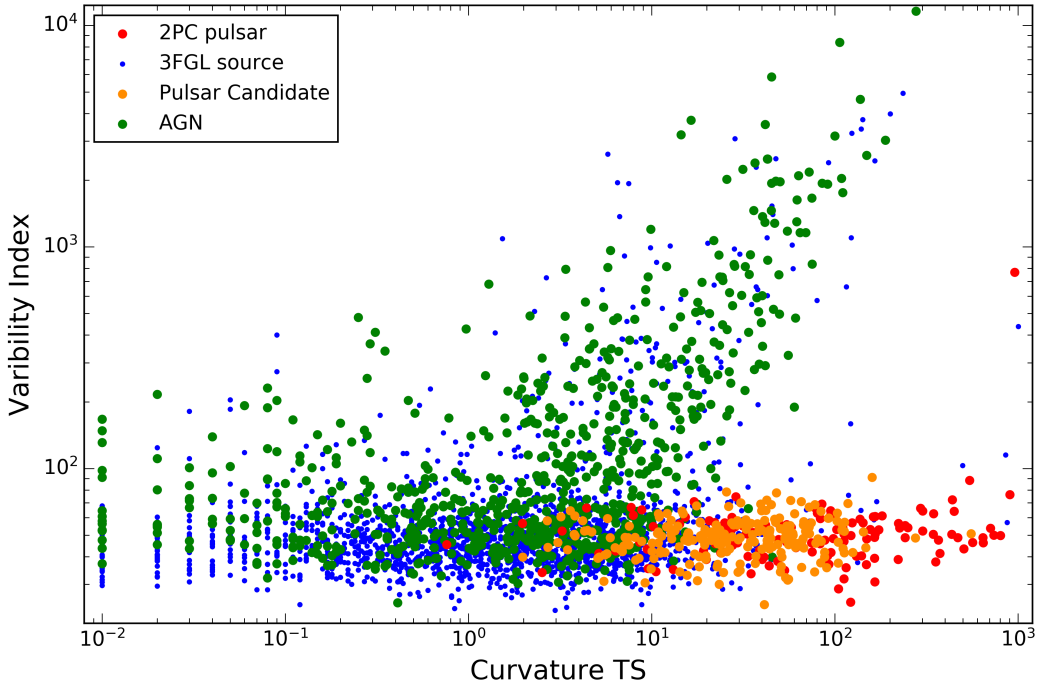

Figure 2.5 Curvature TS versus variability index for all 3FGL sources in blue dots, green dots are known AGNs, red dots are known pulsars and orange dots are pulsar candidates found by GMM with positive pulsar likelihood.

as a third dimension in the Gaussian Mixture Model (GMM) classification scheme can directly correct the above mentioned correlation.

GMM is an unsupervised machine learning algorithms based on Bayesian decision theory (Press et al., 2007). It assumes that data in the parameter space are a superposition of several Gaussian distributions, in our case the *Variability Index*, *Curvature TS* and flux at 1 GeV (F_{1000}). Following the classification scheme from Lee et al. (2012), I defined three Gaussian clusters in the preliminary 3FGL source catalog, the three Gaussians corresponds to Pulsars, AGNs and sources with low fluxes. Using Expectation-Maximization algorithm, parameters of each clusters were determined. I calculated the pulsar likelihood for all the 3FGL sources.

I ranked the 3FGL catalog sources according to the pulsar likelihood. In the ranked source list, the top 10% sources contain 70% known pulsar, the top 50% contain 97% of known pulsar. I selected 341 3FGL sources with positive logarithmic pulsar likelihood ($\log R_s$) values and no associated sources in the 3FGL catalog. The result is overlaid on Figure 2.5 together with the rest of the 3FGL sources, with label for known pulsars and AGNs. In this 341 sources, 118 of them were searched for periodicity and the results of this survey will be presented in Chapter 4 and 5.

2.4 Analysis pipeline

I assembled a spectral analysis pipeline based on the *Pointlike* analysis package (Kerr, 2010) and the *Fermi* Science-tools, allowing us to derive the spectral parameters of the search targets, and to assign good photon weights for the selected datasets. I considered LAT data recorded between 4 August 2008 and 6 April 2014 for our survey, and included photons recorded until 7 July 2015 after a few tens of sources had been searched (see Section 4.3.2).

For the initial datasets, I used the *Fermi* Science-tools[1] to extract Pass 8 Source class events, processed with the `P8_SOURCE_V3` instrument response functions (IRFs). The Science Tools, IRFs and models for the Galactic and extragalactic diffuse γ-ray emission used here are internal pre-release versions of the Pass 8 data analysis, which were the latest versions available to us when the survey began, The differences in the best-fit parameters are marginal, compared to the analysis with the most recent IRFs. Therefore, the weights as calculated with the old IRFs are also very similar. Specifications of follow-up data analyses are given in Section 4.4.

I used `gtselect` to select photons with reconstructed directions within 8° of the 3FGL positions, photon energies > 100 MeV and zenith angles $< 100°$. I only included photons detected when the LAT was operating in normal science mode, and when the rocking angle, the angle of the spacecraft Z-axis from zenith, of the spacecraft was less than 52°. Photons were then binned into 30 logarithmically-spaced energy bins, and with a spatial bin size of 0.1°.

For each 3FGL source, a spectral model for the source within the corresponding Region of Interests (RoIs) was constructed by including all 3FGL sources within 13°.

[1] http://fermi.gsfc.nasa.gov/ssc/data/analysis/software

Spectral parameters of point sources within 5° were allowed to vary. A binned maximum likelihood analysis was performed to measure the γ-ray spectra of the targeted sources, which were modelled with the PLEC model (see Section 2.1.1). The normalization parameters of the Galactic diffuse emission and the isotropic diffuse background components were left free in the fits. The best-fit source models from the likelihood analysis with `Pointlike` were used as inputs for `gtsrcprob` to determine the probabilities that the selected photons were indeed emitted by our targets.

In order to verify the goodness of the fits and check for possible issues in the likelihood results, I produced source significance TS maps and plots of the Spectral Energy Distribution (SED) for each analysed source. Detail discussion can be found in Section 4.3.1.

I eventually obtained datasets consisting of lists of photon arrival times, photon weights and spacecraft positions calculated at each photon time. The spacecraft positions are necessary to correct the arrival times for Doppler shifts caused by the motion of the telescope with respect to the sources. These datasets were then passed on to the blind search algorithm described in Chapter 3, to search for new pulsars among our target sources.

Chapter 3

Blind Search Techiques in Radio and Gamma-ray

Contents

Pulsar searches are primarily carried out at radio wavelengths. All-sky radio pulsar surveys have been done with different telescopes and different frequencies (from 0.3 - 5 GHz) around the globe. An ordinary radio pulsar can be detected in a short observing session, typically less than 30 minutes. The number of photons received per day from γ-ray pulsars is very low ($\sim$10 γ-ray photons per day). Because of the low photon counts, months or even years of continuous exposure is often needed to achieve a significant detection. Due to the aforementioned reason, the technique used in γ-rays is very different from those at radio wavelengths. In this chapter, the method for periodicity search in both radio and γ-ray used in this thesis are presented.

3.1 Periodicity search in radio

Radio pulsar searches can be divided into six steps: 1) data acquisition, 2) radio frequency interference removal, 3) de-dispersion, 4) periodicity search, 5) acceleration search, 6) candidate selection.

The two main pulsar searching software packages are PRESTO (Ransom, 2011) and SIGPROC (Lorimer, 2011). Both of them are capable of analysing different data formats from multiple telescopes. In my PhD project, PRESTO is used for the radio survey presented in Chapter 6.

3.1.1 Data acquisition

Signal coming from either outer space or Earth enters the receiver. The electromagnetic wave are converted into voltages and are amplified. The analogue signal coming from the receiver is converted into the digital with an Analogue-to-Digital converter. Depending on the specification of the backend, the digital signal can be stored as different format based on user's requirement. For example, one can change the time and frequency resolution to study fast rotating pulsars or variabilities in the interstellar medium (ISM). The most common data format for pulsar searches is filterbank. In the filterbank data format, multiple spectra are created by Fourier transforming chunks of signal recorded in a very short duration ($\sim$ ms). A typical filterbank for an hour of pulsar searching observation can take tens of GBs of storage spaces.

3.1.2 Radio Frequency Interference (RFI) removal

The receiver will pick up any signal that is at the right frequency from the right direction, regardless of its nature: whether it is from a radar, a TV tower or a cell phone. All of these unwanted artificial signals are considered as Radio Frequency Interference (RFI). RFI is usually much stronger than astronomical signals because it is originated from the vicinity of the receiver. RFI signals are often periodic becasue of the nature of producing an electrical signal, which can mimic pulsar's signal. Depending on the source, RFI can be persistent or transient, narrow band or broad band. If RFI are not treated properly, it will be mistaken for a pulsar candidate.

RFI needs to be removed as much as possible at the beginning of the search pipeline. As mentioned in Section 3.1.2, signals travelling through space experience a frequency-dependent delay called dispersion. For any signal which is produced on Earth, no dispersion should be observed. Making use of this nature of RFI, we first search for periodic signals in the Fourier domain with no de-dispersion applied (i.e. DM = 0), by doing this, periodic RFI signals can be masked out. To remove short bursts of RFI, a routine called *rfifind* in PRESTO creates a mask for a given observation by calculating and comparing the statistics with the data to pick out transient RFI. Figure 3.1 gives an example of the output of *rfifind*, which created a RFI mask based on the statistic criteria specified.

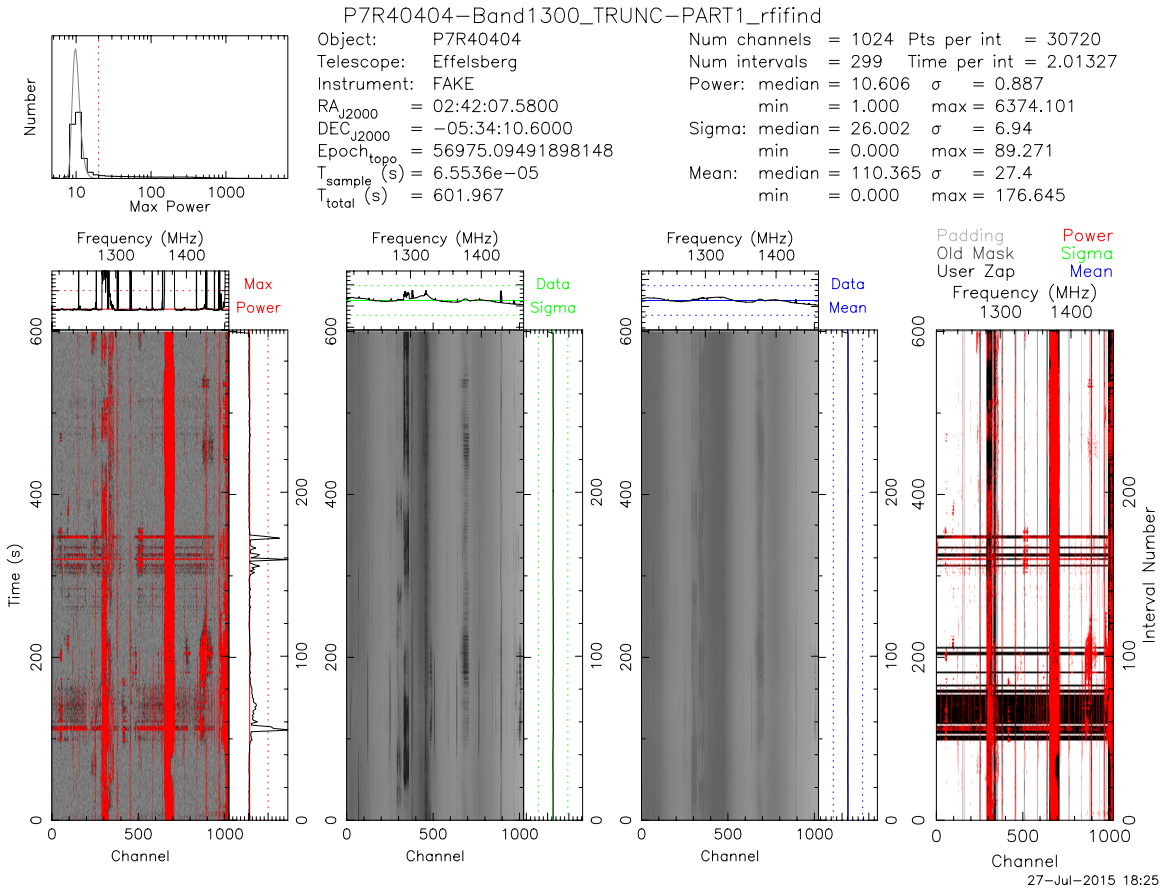

Figure 3.1 Example of RFI mitigation routine plot produced by **rfifind** for one of the observation taken for the radio pulsar survey in Chapter 6. Top-left: The distribution of the data in terms of the signal power. Top-right: Observation details including name, telescope, epoch, data time sampling and data statistics. Lower panels from left to right: The first plot is showing the periodic RFI in red. The second plot is showing the distribution of the data sigma. The second plot is showing the distribution data mean. The forth plot is showing the fraction of data is going to mask in black.

3.1.3 De-dispersion

After the RFI mask is created, the data is ready for further processing. The pulsar signal is dispersed in the ISM as explained in Section 1.2.6: the amount of the time delay is determined by the amount of free electrons along the line of sight, which is an unknown. In order to pick up the very weak signal from the pulsar, we need to correct for this time delay due to the ISM before performing any periodicity search. Essentially, we create numerous instances of the data with different DM values and perform a periodicity search in every DM trial.

So what should be the search range of DM and what should be used as the step size ΔDM? If the DM step is too fine, at some point the computational cost will increase without any gain in sensitivity. On the other hand, if the step is too coarse the signal might be lost if the true DM falls right in between two DM steps. The optimal DM step depends on the observing frequency ν, the bandwidth of the observation $\Delta\nu$ and the sampling time $t_{\rm samp}$, expressed in this formula (Lorimer & Kramer, 2005),

$$\Delta\mathrm{DM} = 1.205 \times 10^{-7}\ t_{\rm samp}\ \left(\frac{\nu^3}{\Delta\nu}\right)\ \ [\mathrm{pc\ cm^{-3}}]. \tag{3.1}$$

With the given ΔDM, the filterbank is then de-dispersed into a 1-D time series according to the list of pre-calculated DM values.

3.1.4 Periodicity search

The de-dispersed time series is then Fourier transformed into Fourier spectra to identify possible periodicities. This routine is done by the *realfft* routine which is based on the FFTW library[1], a commonly used library for performing fast Fourier transforms.

A radio pulse profile is never a perfect sinusoidal function, instead the radio pulse consists of a number of sharp components. In the Fourier domain, these components are translated into a number of harmonics, spreading the power of the original pulse signal. To recover the total power of the pulsed signal, a technique called harmonic summing, first developed by Taylor & Huguenin (1969), is used. The original Fourier spectrum is stretched by a factor 2, it is then added to the original Fourier spectrum, in this case, all the second harmonic power are added to the fundamentals. By repeating this process with stretching factors of 4, 8 or 16, most of the signal from harmonically related peaks can be recovered.

If the pulsar is in a binary system, the peak in the Fourier spectrum will be spread across multiple frequency bins because the pulsed signals are doppler-shifted depending on which part of the orbit the pulsar is at. The apparent period $P(t)$ and period derivative $\dot{P}(t)$ of the pulse can be described by,

$$P(t) = P_0\Big(1 + \frac{v_{\rm l}(t)}{c}\Big) \tag{3.2}$$

[1] http://www.fftw.org

and

$$\dot{P}(t) = \dot{P}_0 \frac{a_\mathrm{l}(t)}{c}, \tag{3.3}$$

where P_0 and $\dot{P}_0$ are the intrinsic spin period and derivative, $v_\mathrm{l}(t)$ and $a_\mathrm{l}(t)$ are velocity and acceleration component along the line of sight. This effect will be greater for higher accelerations, as the orbit gets tighter. To recover the pulsed signal from a binary system, Ransom et al. (2002) developed *accelsearch*, a routine in PRESTO. In *accelsearch*, the acceleration of the pulsar is assumed to be constant throughout the observation Δt_obs, this constant acceleration assumption is only good for approximately ∼10% of the orbit. With the given acceleration, the maximum number of frequency bins in the Fourier series that the power will spread into can be expressed as:

$$z_\mathrm{max} = \Delta t_\mathrm{obs}^2 \frac{a_\mathrm{l}(t)}{cP}, \tag{3.4}$$

where z_max determines how many additional Fourier bins are needed on both sides around the given frequency.

3.1.5 Pulsar candidate

To decide which peak found in the Fourier spectrum could be a pulsar candidate that is worth following up, a threshold in power or signal-to-noise (S/N) needs to be set. In the Fourier domain, the minimum signal-to-noise threshold $(\mathrm{S/N})_\mathrm{min}$ is

$$(\mathrm{S/N})_\mathrm{min} = \frac{\sqrt{\ln(n_\mathrm{trials})} - \sqrt{\pi/4}}{1 - \pi/4} \tag{3.5}$$

where n_trials corresponds to the number of bins in the Fourier spectrum, multiplied by the number of harmonic summing and the number of DM trials (Lorimer et al., 2006). If acceleration search is also performed, the number of acceleration trials also needs to be accounted for.

Across all the searched DMs, the number of potential candidates can reach over a thousand for the threshold we have set. In order to bring down the number of candidates, sifting algorithms are applied to remove duplicated candidates. A sifting routine typically looks for duplicated periodicities found at different accelerations and DMs, keeping only the most significant one. It also removes candidates which are harmonically related.

3.1.6 Folding and Confirmation

To visualize the candidate, folding the raw data according to the given period, period derivative and DM can generate a diagnostic plot, which provides useful information for human or artificial intelligence to assess if the candidate is a genuine detection. Such a plot contains the integrated pulse profile, the pulse strength across the observing frequency band and time, the S/N as a function of DM. Figure 3.2 shows an example of a diagnostic plot created by *prepfold*, a program in PRESTO, for one of the test

pulsars used in the radio pulsar survey in Chapter 6. From the diagnostic plot we can tell if the signal is broadband, if it is persistence in time and if it peaks at a certain DM. Due to the shear number of diagnostic plots produced in every observation, automatic evaluation with machine learning algorithms have been developed to further reduce the number of candidates required to be examines by eye or using artificial intelligence (AI) program. See for example, Pulsar Evaluation Algorithm for Candidate Extraction (PEACE) (Lee et al., 2013) and Pulsar Image-based Classification System (PICS) (Zhu et al., 2014). If the candidate passes all the above tests it will be re-observed to see if the same periodicity and DM can be found.

3.2 Periodicity search in γ-ray

Searching for pulsations in γ-rays is a totally different problem. As mentioned in Section 1.4.4, the challenge in detecting γ-ray pulsars is the low photon count: we detect one photon for every few thousand rotations of the pulsar. A detection therefore requires long integration time in order to gather enough pulsed photons ($\simeq$ years).

In order to search for gamma-ray pulsations, a phase model is needed to relate the photon arrival time to a rotational phase. For an isolated pulsar, the rotational phase can be described by expanding a Taylor series from a reference epoch t_0, for photon arrival time t at the solar system barycenter reference frame,

$$\Phi(t) = \Phi_0 + 2\pi \sum_{m=1} \frac{f^{(m-1)}}{m!}(t - t_{ref})^m, \tag{3.6}$$

where $f^{(m)}$ denotes the m-th time derivative of the pulsar's rotational frequency, f. The higher derivative terms are often measured for young pulsars but not old millisecond pulsar. For blind search purposes, it is sufficient to only include up to the 1st time derivative (i.e. assuming a constant spin-down rate $\dot{f} \equiv f^{(1)}$).

Also, due to the angular size of the unassociated gamma-ray point source, it is necessary to search through two sky positional parameters (R.A. α and Decl. δ), which makes the search parameter space four-dimensional (i.e. $f, \dot{f}, \alpha, \delta$).

In this section, the hierarchical 3-staged blind search scheme following the discussion from Pletsch & Clark (2014), which were used in Chapter 4 and 5, will be discussed.

3.2.1 Photon weighting technique

One of the key advances of the blind search algorithm is the use of the photon weight, describe in Kerr (2011). The ability to assign a weight according to the source's spectrum from likelihood analysis reduces the number of trials needed to optimize the extraction region together with the energy range. In this section, the principle of photon weight calculation will be briefly discussed.

Once again, we assumed the source is stationary. The exposure of the source at the position ($\vec{\Omega}_0$) is given by $\varepsilon(E, \vec{\Omega}_0)$ (cm^2 s), the expected differential rate in the unit of

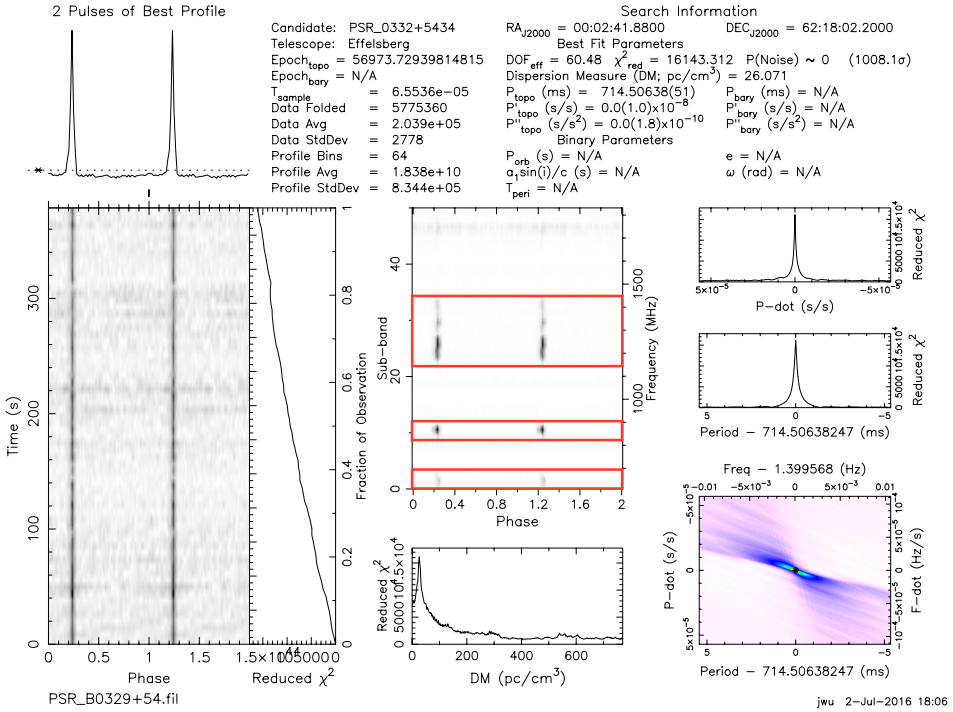

Figure 3.2 Example of candidate evaluation plot produced by **prepfold** for pulsar PSR J0332+5435 (B0329+54). Top-left: Integrated pulse, two rotations are shown for clarity. Top-right: Observational details including name, telescope, epoch, data time sampling, data statistics, position, period and period derivatives (for topocentric and barycentric references), and binary parameters if applicable. Lower-left: Plot showing the intensity as a function of rotational phase and observing time, together with a time evolution of the reduced χ^2 of the integrated profile. Middle-centre: Plot of the intensity as a function of rotational phase versus frequency, red boxes highlight the UBB usable bands. Middle-bottom: Reduced χ^2 as a function of trial DM. Lower-right: Plot of reduced χ^2 for the integrated profile as a function of folding period and period derivative. Middle-right: Two plots with one-dimensional projection from the plot shown in the lower-right panel.

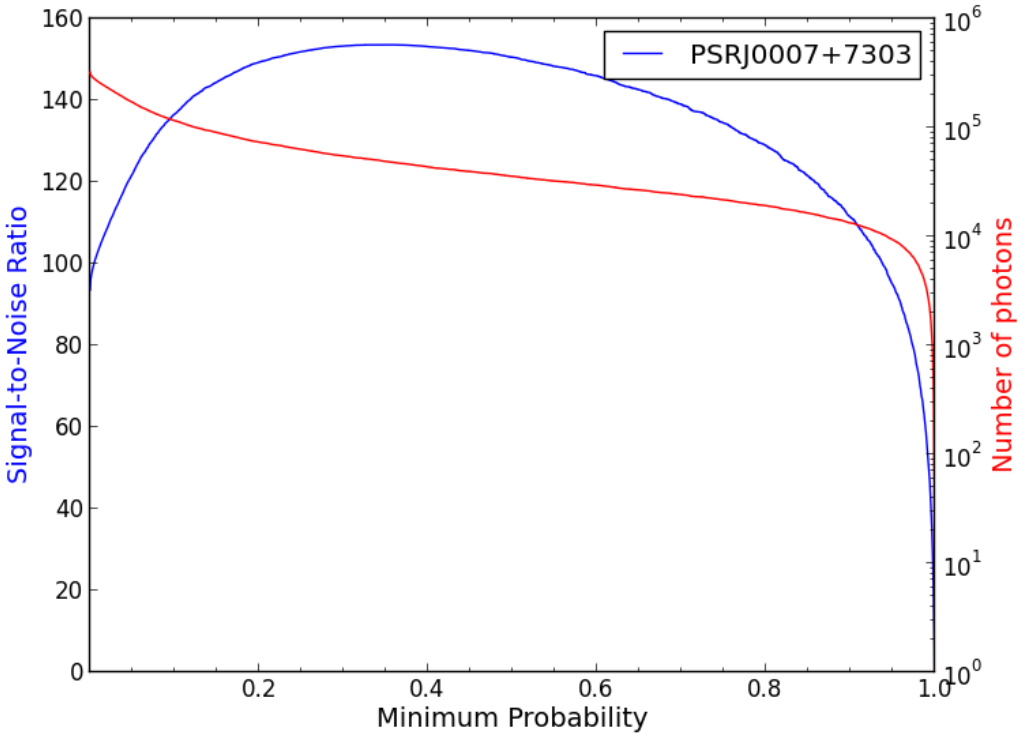

Figure 3.3 Minimum probability as a function of the signal-to-noise ratio (in blue) and number of photons (in red) for PSR J0007+7303 (CTA 1). The signal-to-noise ratio is defineed by the cumulative weight divided by the number of photons.

ph MeV^{-1} sr^{-1} in the detector from the jth source is

$$r_j(E, \vec{\Omega}_0) = \mathcal{F}(E, \vec{\lambda}_0)\varepsilon(E, \vec{\Omega}_0) f_{\mathrm{psf}}(\vec{\Omega}; \vec{\Omega}_0, E), \tag{3.7}$$

where $f_{\mathrm{psf}}(\vec{\Omega}; \vec{\Omega}_0, E)$ is the PSF of the instrument for the incident energy and position.

The probability of a photon with energy E at a position near $\vec{\Omega}$ that it originated at the jth source is

$$w_j(E, \vec{\Omega}|\vec{\lambda}) \equiv \frac{r_j(E, \vec{\Omega}, \vec{\lambda}_j)}{\sum_{i=1}^{N_s} r_i(E, \vec{\Omega}, \vec{\lambda}_i)}, \tag{3.8}$$

where N_s is the number of sources used in estimating the probability. For photon with position very close to the source and at high energy the weight can approach 1 as the LAT PSF gets narrower, Figure 3.3 shows the distribution of weight for one of the known γ-ray pulsar PSR J0007+7303.

By implementing the photon weight we can calculate the pulse significance with the weighted H-test using equation 4.14. The used of photon weight greatly improved our

sensitivity towards pulsed signal in our blind searches. As we are not longer suffered from the unknown optimal minimum photon energy and and search RoI size, which are not sensitive with the use of photon weights. Figure 3.4 shows the pulse profile of a gamma-ray pulsar with and without the use of photon weight.

3.2.2 Semi-coherent stage

The first stage of the search is a semi-coherent stage. A sliding coherent window with a length T is used to move across the full dataset. In our survey a lag window of 24 and 48 days is used to optimize the sensitivity and computational cost in the first and the second semi-coherent refinement stage. The semi-coherent detection statistic S_1, is defined as

$$S_1 = \frac{1}{\kappa_{S_1}} \sum_{j=1}^{N} \sum_{k\neq 1}^{N} w_j w_k e^{-i[\Phi(t_j)-\Phi(t_k)]} \hat{W}_T^{\mathrm{rect}}(\tau_{jk}) \tag{3.9}$$

where τ_{jk} is the time difference (or "lag") between the arrival times of the j-th and k-th photons and $\hat{W}$ is a step function with length T,

$$\hat{W}_T^{\mathrm{rect}}(\tau) = \begin{cases} 1, & |\tau| \leq T/2. \\ 0, & \text{othewise}, \end{cases} \tag{3.10}$$

and κ_{S_1} is a normalizing factor,

$$\kappa_{S_1} \sqrt{\sum_{j=1}^{N} \sum_{k\neq 1}^{N} w_j w_k \hat{W}_T^{\mathrm{rect}}(\tau)}, \tag{3.11}$$

so that the noise distribution of S_1 follows normal distribution with zero mean and variance.

By using the FFTW library, the semi-coherent detection statistic S_1 can be approximated as a discrete Fourier transform (DFT), which is more computationally efficient. In this stage the dataset will be searched over a range of frequencies f, spin-downs $\dot{f}$ and sky positions (α, δ), the step size and the sky-gird are determined using the metric formulation to ensure optimal coverage (Pletsch & Clark, 2014). S_1 is calculated in each FFT and the short-listed candidate with highest S_1 value will be passed to semi-coherent refinement stage which uses two times the original lag window to further reduce the number candidates before passing to the next stage.

3.2.3 Coherent follow-up

The list of candidates after the semi-coherent search is small enough for a fully coherent search. For the coherent stage, we extend the lag window to the size of the full dataset, and we evaluate the coherent detection statistic on a refined grid. The

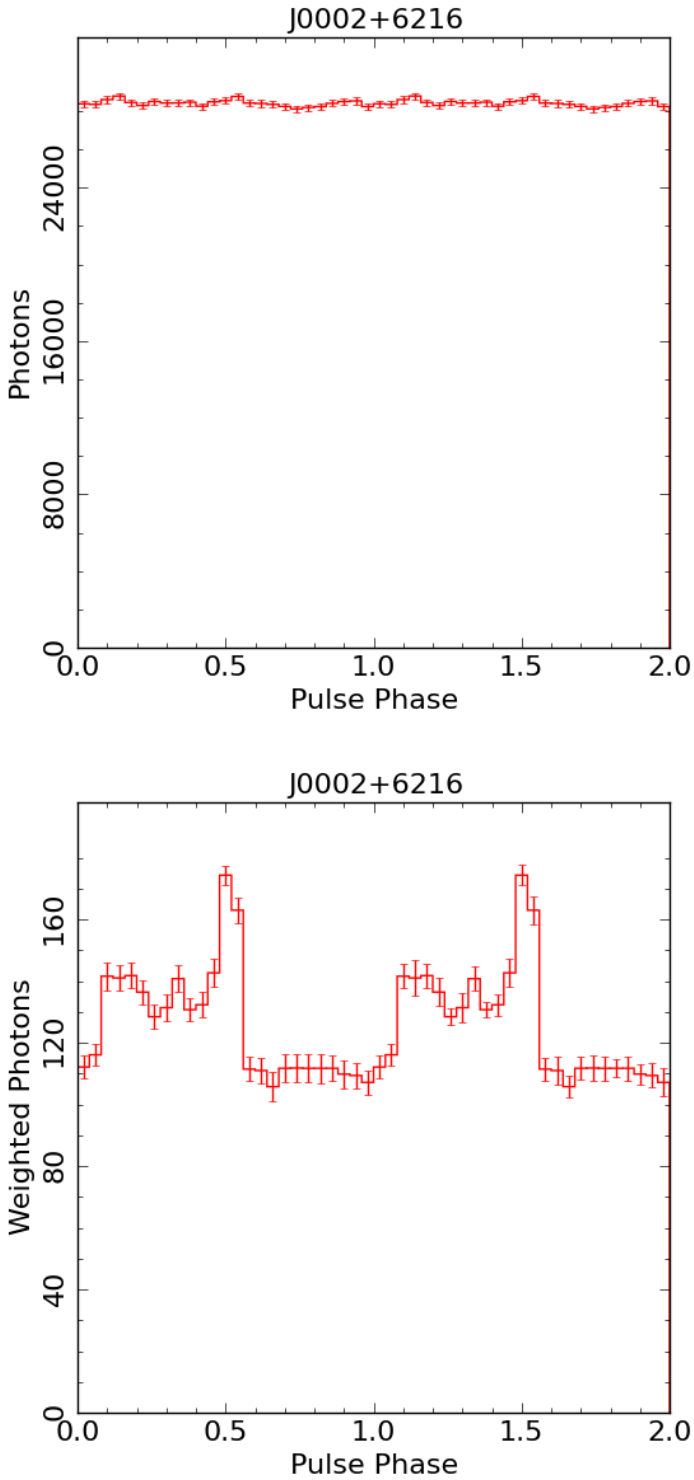

Figure 3.4 Top: Unweighted light curve for PSRs J0002+6216 using photons within 5° of the timing position. Bottom: Light curve using the same set of photons but with photon weight taken into account.

coherent detection statistic,

$$P_n = \frac{1}{\kappa^2}\left|\sum_{j=1}^{N} w_j e^{-in\phi(t_j)}\right|^2, \tag{3.12}$$

with the normalization constant κ,

$$\kappa^2 = \frac{1}{2}\sum_{j=1}^{N} w_j^2. \tag{3.13}$$

Only the fundamental power (i.e., n = 1) is considered at this stage. If the candidate's P_1 is statistically significant, it will proceed to the next refinement phase.

3.2.4 Higher signal harmonics

Significant candidates selected from the coherent follow-up will first have their location refined with the P_1 statistic using a very fine grid. Then a fully coherent search using the H-test on the further refined candidate is performed. H-test was developed by de Jager et al. (1989), which is designed to combine the coherent Fourier from higher harmonics from the pulsed signal with no prior knowledge of the pulse profile, by maximizing the number of combined harmonics M,

$$H = \max_{1\leq M\leq 20}\left(\sum_{n=1}^{M} P_n - 4M + 4\right). \tag{3.14}$$

After the refinement step, each candidate can be visualized with a set of diagnostic plots, illustrating the candidate signals and their evolution throughout the *Fermi*-LAT observation. An example of the diagnostic plots for a pulsar detected in our survey is shown in Figure 3.7. These diagnostic plots allow us to visually check if there is any signal hidden in the data despite the low coherent power due to timing noise.

3.3 Summary

This chapter has presented the method and technique for pulsar periodicities search in radio and γ-ray used throughout my PhD projects. The semi-coherent multi-staged algorithm described in this chapter is the most advanced blind search algorithm to date. Using this γ-ray blind search technique presented in this chapter, we discovered 17 γ-ray pulsars in our Einstein@Home γ-ray pulsar survey (Chapters 4 and 5). The methodology for RFI mitigation and radio periodicity searches presented in this chapter were used in a target radio pulsar survey in unassoicated *Fermi*-LAT sources at Effelsberg (Chapter 6).

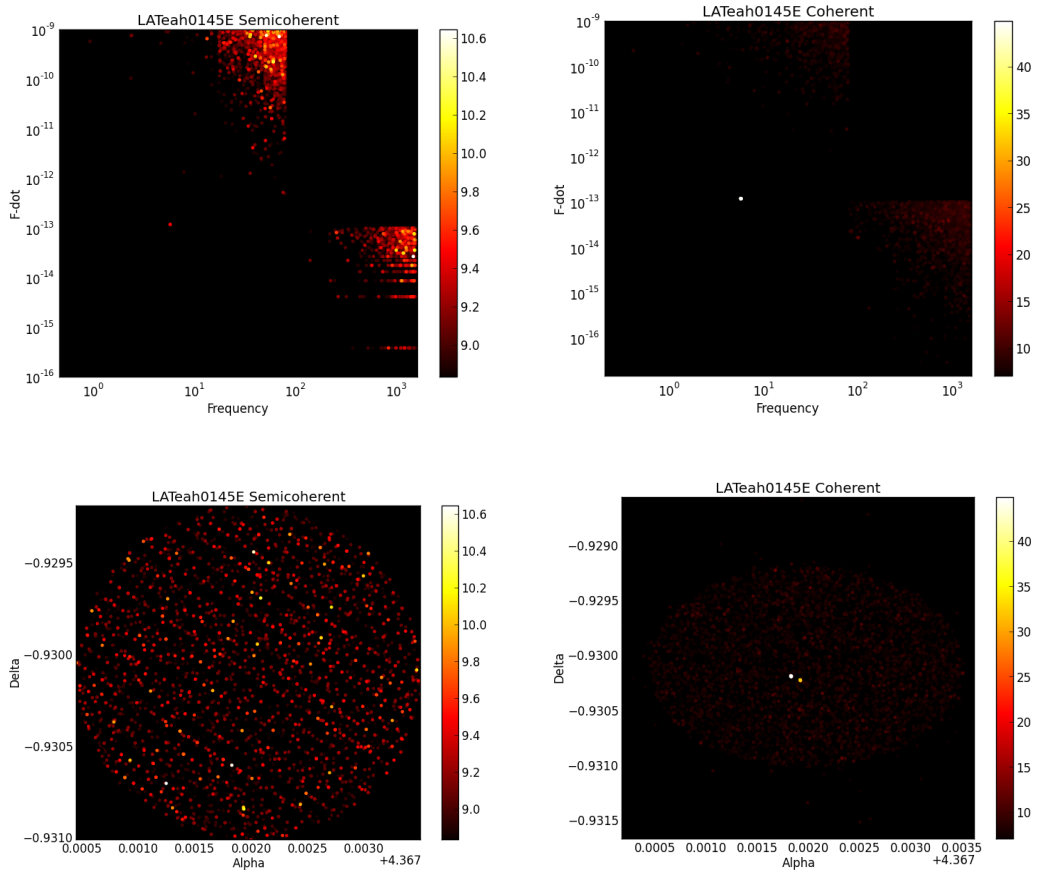

Figure 3.5 Upper left, upper right : $f - \dot{f}$ space in the semi-coherent stage and coherent stage for one of the detected pulsar. Lower left, lower right : Sky position of in semi-coherent stage and coherent stage. Colour scale indicates detection statistic S_1.

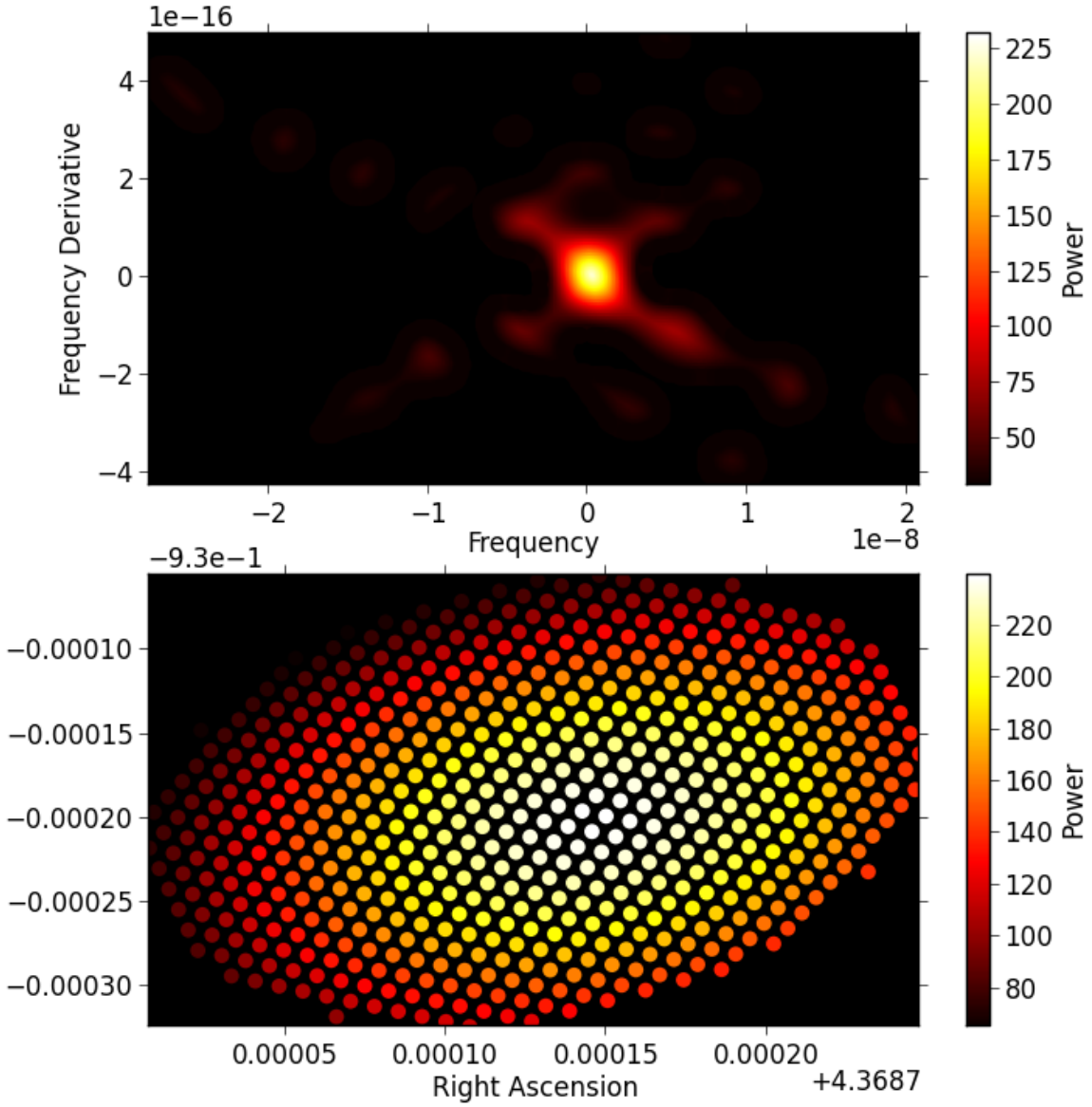

Figure 3.6 Refinement stage of the same pulsar candidate shown in Figure 3.5. Top: Detection significance maps in the $f - \dot{f}$ space. Bottom: Detection significance maps in the sky position.

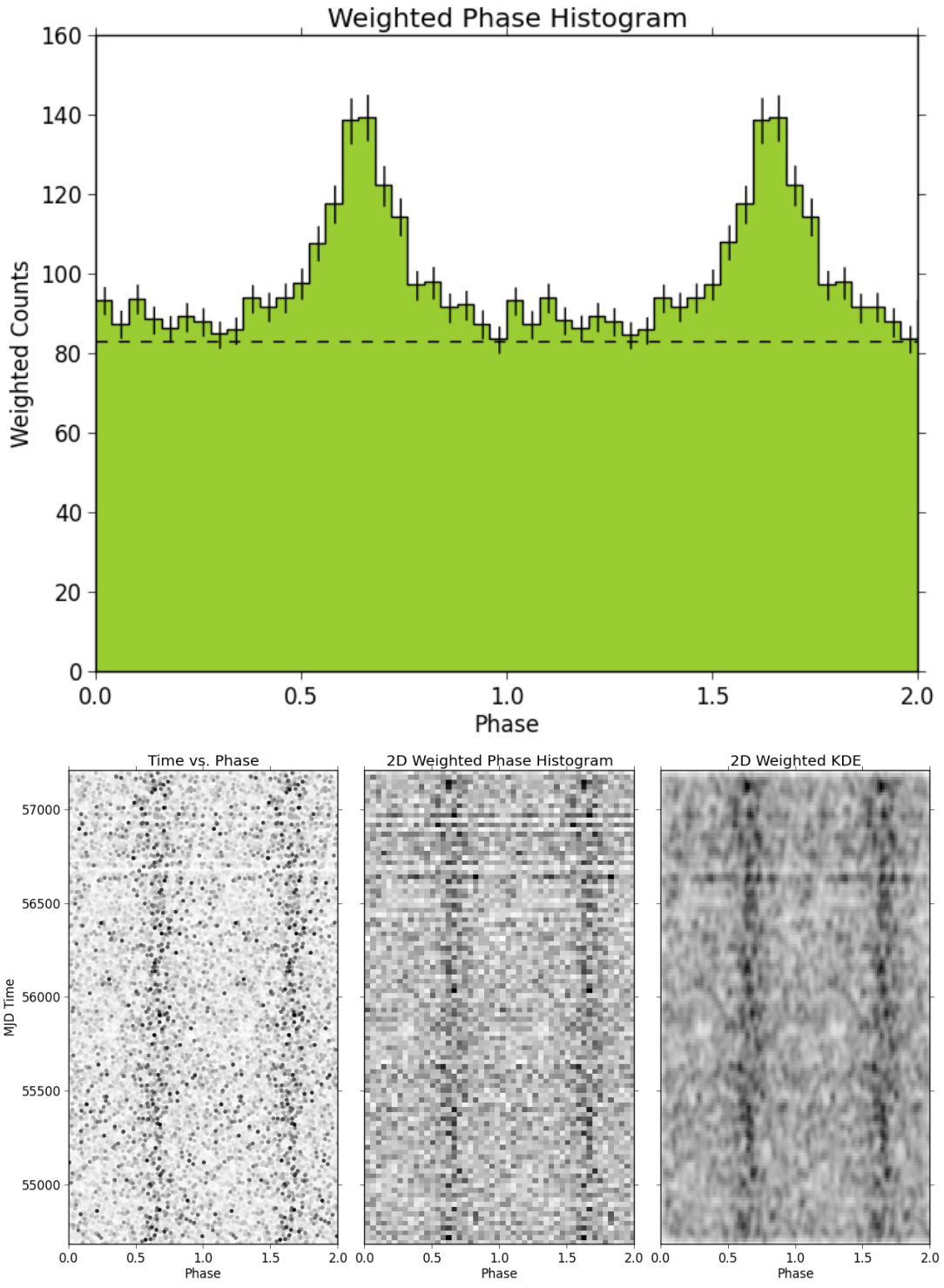

Figure 3.7 Top: Folded γ-ray profile from one of the detected pulsar, two rotations are shown for clarity. Bottom panels: Phase-time diagrams where the γ-ray photons are displayed with different methods. Bottom left: Each point represents one photon, with the intensity representing the photon weight. Bottom middle: 2D Weighted Histogram. Bottom right: 2D Weighted Kernel Density Estimation (KDE).

Chapter 4

The Einstein @ Home Gamma-Ray Pulsar Survey : 13 new discoveries

---

This chapter is based on an article accepted for publication to the Astrophysical Journal with the title:

The Einstein@Home Gamma-ray Pulsar Survey II. Source Selection, Spectral Analysis and Multi-Wavelength Follow-up

The text, figures, and tables have only been modified to match the style, spelling and format of the rest of this thesis.

I am the lead author of the article. My main contributions include selecting unassocicated 3FGL sources using the Gaussian Mixture Model described in Chapter 2, developing the data reduction pipeline for the blind search, including follow-up γ-ray spectral analysis. I also reduced the radio observations taken by Effelsberg.

The full list of authors is: **J. Wu**, C. J. Clark, H. J. Pletsch, L. Guillemot, T. J. Johnson, P. Torne, D. J. Champion, J. Deneva, P. S. Ray, D. Salvetti, M. Kramer, C. Aulbert, C. Beer, B. Bhattacharyya, O. Bock, F. Camilo, I. Cognard, A. Cuéllar, H. B. Eggenstein, H. Fehrmann, E. C. Ferrara, M. Kerr, B. Machenschalk, S. M. Ransom, S. Sanpa-Arsa and K. Wood

Abstract
We report on the analysis of 13 gamma-ray pulsars discovered in the Einstein@Home blind search survey using *Fermi* Large Area Telescope (LAT) Pass 8 data. The 13 new gamma-ray pulsars were discovered by searching 118 unassociated LAT sources from the third LAT source catalog (3FGL), selected using the Gaussian Mixture Model (GMM) machine learning algorithm on the basis of their gamma-ray emission properties being suggestive of pulsar magnetospheric emission. The new gamma-ray pulsars have pulse profiles and spectral properties similar to those of previously-detected young gamma-ray pulsars. Follow-up radio observations have revealed faint radio pulsations from two of the newly-discovered pulsars, and enabled us to derive upper limits on the radio emission from the others, demonstrating that they are likely radio-quiet gamma-ray pulsars. We also present results from modeling the gamma-ray pulse profiles and radio profiles, if available, using different geometric emission models of pulsars. The high discovery rate of this survey, despite the increasing difficulty of blind pulsar searches

in gamma rays, suggests that new systematic surveys such as presented in this article should be continued when new LAT source catalogs become available.

Contents

4.1 Introduction

Pulsars are rapidly rotating neutron stars with rotational periods ranging from more than 10 seconds to just a few milliseconds. Since their discovery in 1967 (Hewish et al., 1968), various pulsar surveys have discovered over 2600 pulsars [1]. While the large majority of the known pulsars have been detected in the radio, pulsars are occasionally detected at optical, infrared, UV, X-ray or even gamma-ray frequencies, enabling multi-wavelength studies (see, Swiggum et al., 2017; Mignani et al., 2017, for recent examples).

During the first eight years of operation, over 200 gamma-ray pulsars have been detected by the *Fermi* Large Area Telescope[2] (LAT, Atwood et al., 2009). The majority of the detected gamma-ray pulsars were first found in radio, either discovered from radio pulsar surveys or targeted radio observations of unassociated LAT sources (i.e. sources with no obvious counterparts at other wavelengths, see, e.g., Cognard et al., 2011; Keith et al., 2011; Ransom et al., 2011; Camilo et al., 2012; Guillemot et al., 2012a; Kerr et al., 2012; Barr et al., 2013; Bhattacharyya et al., 2013; Camilo et al., 2015; Cromartie et al., 2016). However, a substantial fraction of the gamma-ray pulsars have been discovered by direct, blind searches of the LAT data (e.g., Abdo et al., 2009b; Saz Parkinson et al., 2010; Pletsch et al., 2012b; Clark et al., 2015).

[1] http://www.atnf.csiro.au/research/pulsar/psrcat/
[2] See https://tinyurl.com/fermipulsars for the list of LAT-detected pulsars

Gamma-ray pulsars found in blind searches are interesting for many reasons. These pulsars are young and energetic with characteristic ages < 3 Myr and spin down power $\dot{E} > 10^{33}$ erg s^{-1}(see Figure 1 of the second *Fermi* LAT catalog of gamma-ray pulsars, hereafter 2PC, Abdo et al., 2013). These young energetic pulsars often have timing noise and glitches. This absence of timing coherence makes their pulsations more difficult to find in the low count-rate gamma-ray data acquired over time spans of years. The discovery of PSR J1906+0722 (Clark et al., 2015) demonstrated the ability of the improved semi-coherent blind search technique to detect pulsars even when the data contain timing noise and a substantial glitch. Such blind search methods can reduce the bias against the discovery of young and energetic radio-quiet pulsars in the current pulsar population.

Although the 41 pulsars found in previous blind gamma-ray searches represent a small fraction of the total pulsar population, this increasing population form a very distinct group with extremely faint or undetectable radio emission. Besides the possible detections of J1732−3131 (Maan et al., 2012) and Geminga (Maan, 2015), only four gamma-ray discovered pulsars have also been detected in radio, two of them being radio-loud (we follow the convention used in 2PC, i.e., pulsars are considered radio-quiet if their radio flux densities at 1400 MHz, S_{1400}, are smaller than 30 μJy), J1741−2054 and J2032+4127 (Camilo et al., 2009) and the remaining two, J0106+4855 (Pletsch et al., 2012b) and J1907+0602 (Abdo et al., 2010c), are considered radio-quiet.

To further increase the number of known gamma-ray pulsars, a new blind search of unidentified LAT sources with gamma-ray emission properties resembling known pulsars was initiated. This search has been conducted on the distributed volunteer computing system Einstein@Home[3] using the newly improved Pass 8 LAT data. This dataset provides a number of improvements such as better energy reconstruction and better background rejection (see Atwood et al., 2013) therefore increasing its sensitivity.

Based on their gamma-ray properties, we have selected and searched 118 unassociated LAT sources, resulting in the discovery of 17 pulsars. The results of this search are presented in two papers; Paper I (Clark et al., 2017) focused on the search method, sensitivity and temporal characteristics of the recent pulsar discoveries. In this second paper, we present the source selection scheme, the data preparation process, and detailed gamma-ray analyses and radio follow-up observations of the discoveries. In Section 4.2, we describe the method used for selecting gamma-ray sources for the blind search. Section 4.3 describes the analysis procedure we followed for preparing the gamma-ray data to be searched for pulsars. Gamma-ray, X-ray and radio follow-up analyses of the newly discovered pulsars are described in Section 4.4, and we conclude with a discussion of the properties of the new pulsars.

[3]https://einsteinathome.org

4.2 Source selection

4.2.1 3FGL catalog

The third catalog of LAT sources (hereafter 3FGL, Acero et al., 2015) lists the properties of 3033 gamma-ray sources detected by the LAT in the first four years of data taking. More than 30% of the 3FGL sources were unassociated at the time of publication. More than one hundred of these unassociated sources have been demonstrated to be previously unknown pulsars, discovered either in deep targeted radio observations or in blind searches using the LAT data. Due to the observing time and processing resources required for a timing search, identifying which of these sources are most likely to be pulsars has become a task of paramount importance. In contrast to several other classes of gamma-ray sources, pulsars have significant cutoffs in their emission spectra at energies of a few GeV and gamma-ray fluxes that are generally very stable (however see Allafort et al., 2013, for a counter-example); hence the curvature significance[4] ("Signif_Curve", S_c) and the variability index[5] ("Variability_Index", VI), which are respectively measures of the curvature of a source's spectrum and of its gamma-ray flux variability, have been successfully applied in previous similar surveys (e.g., Pletsch et al., 2012b).

We note that only a preliminary version of the 3FGL catalog was available when our survey was initiated. We therefore assessed the pulsar likelihood of the unassociated sources from this preliminary catalog. As a cross-check of our source selection results we have compared the data from the preliminary catalog with those from 3FGL, finding differences in one specific parameter only. These differences are discussed in the next section.

4.2.2 Pulsar candidate classification

Although using S_c and VI seems to be enough to identify pulsar candidates, extra care needs to be taken as these two parameters are correlated with the detection significance. A number of groups have developed different schemes for classifying sources, involving machine learning techniques (Lee et al., 2012; Mirabal et al., 2012; Saz Parkinson et al., 2016). In particular, Lee et al. (2012) have shown that including the gamma-ray flux as a third dimension in the pulsar classification scheme can directly correct the above-mentioned correlation. Applying the Gaussian Mixture Model (GMM) classification scheme from Lee et al. (2012), we used the VI, S_c and F_{1000} (gamma-ray flux above 1 GeV) parameters from the catalog to calculate the pulsar likelihood R_s for all the sources. A positive log R_s indicates that the source is likely to be a pulsar (see Lee et al., 2012, for a detailed discussion). A list of 341 sources with positive logarithmic pulsar likelihood (log R_s) values and no firm associations with any other astrophysical

[4] Significance (in σ units) of the fit improvement when assuming a curved spectral type (e.g., PLEC, see Section 4.3.1) instead of a simple power-law for the source of interest. Values greater than 4 indicate significant curvature.

[5] Index quantifying the variability of a source on a time scale of months. An index larger than 72.44 corresponds to a >99% confidence probability that the source of interest has a variable flux.

sources was obtained.

As mentioned in Section 4.2.1, the list of pulsar candidates was produced by analyzing a preliminary version of the 3FGL catalog. We verified that the characteristics of most of the sources from the preliminary catalog are identical to those from the final catalog. One difference concerns the definition of the spectral curvature Test Statistic (TS), $\mathrm{TS_{curve}}$, listed instead of the curvature significance in the preliminary version of the catalog, $S_c = \sqrt{\mathrm{TS_{curve}} \times \mathrm{R_{syst}}}$, where $\mathrm{R_{syst}}$ accounts for systematic uncertainties in the effective area. We verified that using $\mathrm{TS_{curve}}$ instead S_c as one of the inputs of the GMM does not affect our classification results.

4.3 Data preparation

4.3.1 The spectral analysis pipeline

One of the main difficulties in blind searches for gamma-ray pulsars is separating background emission from photons originating from the sources of interest. Due to the wide and energy dependent point-spread function of the LAT at low energies[6], neighboring sources within a few degrees of a given direction can raise the background level in the dataset considered for the search. In the past, blind searches often adopted a so-called "cookie cutter" to select photons and increase the signal-to-noise ratio, i.e., they restricted the region of interest (RoI) by selecting events with reconstructed directions found within, say, $\sim 1°$of the considered sky location. Although this technique can efficiently separate source and background photons for some bright pulsars or pulsars in regions of low background contamination, most of the young gamma-ray pulsars are located near the Galactic plane, where the diffuse background emission is strong and where the effectiveness of the cookie cutter selection method decreases. Kerr (2011) mitigated this problem by proposing a photon-weighting technique, which uses information about the spectrum of the targeted source and the instrumental response of the LAT. Probabilities that photons originate from the source can then be calculated, relaxing the need to select narrow sky regions and greatly improving our sensitivity to weak periodic signals.

Consequently, accurately determining the spectra of the sources we want to search for pulsations is key for calculating photon weights and thereby increasing the signal-to-noise ratio. We assembled a spectral analysis pipeline based on the `Pointlike` analysis package (Kerr, 2010), allowing us to derive the spectral parameters of the search targets, and to assign good photon weights for the selected datasets. We initially considered LAT data recorded between 2008 August 4 and 2014 April 6 for our survey, and included photons recorded until 2015 July 7 after a few tens of sources had been searched (see Section 4.3.2). We used the *Fermi* Science Tools[7] to extract Pass 8 Source class events, processed with the `P8_SOURCE_V3` instrument response functions (IRFs). The Science Tools, IRFs and models for the Galactic and extragalactic diffuse gamma-ray emission used here are internal pre-release versions of the Pass 8 data analysis,

[6] https://www.slac.stanford.edu/exp/glast/groups/canda/lat_Performance.htm
[7] http://fermi.gsfc.nasa.gov/ssc/data/analysis/software

which were the latest versions available to us when the survey began, The differences in the best-fit parameters are marginal, compared to the analysis with the most recent IRFs. Therefore, the weights as calculated with the old IRFs are also very similar. Specifications of follow-up data analyses are given in Section 4.4. We used `gtselect` to select photons with reconstructed directions within 8°of the 3FGL positions, photon energies > 100 MeV and zenith angles $< 100°$. We only included photons detected when the LAT was operating in normal science mode, and when the rocking angle of the spacecraft was less than 52°. Photons were then binned into 30 logarithmically-spaced energy bins, and with a spatial bin size of 0.1°.

For each 3FGL target, a spectral model for the sources within the corresponding RoIs was constructed by including all 3FGL sources within 13°. Spectral parameters of point sources within 5°were allowed to vary. A binned maximum likelihood analysis was performed to measure the gamma-ray spectra of the targeted sources, which were modeled with exponentially cut-off power laws ("PLEC" spectral shapes), of the form:

$$\frac{dN}{dE} = K \left(\frac{E}{1 \text{ GeV}} \right)^{-\Gamma} \exp\left(-\frac{E}{E_{\text{cut}}} \right), \tag{4.1}$$

where K is a normalization factor, E_{cut} is the cutoff energy and Γ is the photon index. The above expression accurately reproduces the phase-averaged spectral properties of the majority of known gamma-ray pulsars (see, e.g., 2PC). The normalization parameters of the Galactic diffuse emission and the isotropic diffuse background components were left free in the fits. The best-fit source models from the likelihood analysis with `Pointlike` were used as inputs for `gtsrcprob`, to determine the probabilities that the selected photons were indeed emitted by our targets.

In order to verify the goodness of the fits and check for possible issues in the likelihood results, we produced source significance TS maps and plots of the Spectral Energy Distribution (SED) for each analyzed source. For some of the sources, the best-fit cut-off energies were suspiciously high and were in particular much higher than those of known gamma-ray pulsars. These sources have spectra with low curvature, and could potentially be associated with Supernova Remnants (SNRs) or Pulsar Wind Nebulae (PWNe) which are known to have harder spectra than pulsars. For some sources a very high cutoff energy close to the upper bound of 1 TeV used for the fit was found, suggesting low spectral curvature. In some cases the best-fit photon index Γ was close to 0. These low photon indices were found for sources with low TS values. We flagged these problematic sources, but included them in the survey despite the abnormal spectral results since we may still be able to detect pulsations from these sources. We note that SEDs for the latter sources were generally consistent with 3FGL results. In addition, for a small number of 3FGL sources our analysis failed to converge, possibly because of complicated sky regions. Those sources were removed from the target list, and will be revisited in the future. As a result, the original target list was trimmed down to 118 sources, which are listed in the table in the Appendix.

We eventually obtained datasets consisting of lists of photon arrival times to be searched for pulsations, photon weights, and spacecraft positions calculated at each

photon time, which are necessary to correct the arrival times for Doppler shifts caused by the motion of the telescope with respect to the sources. These datasets were then passed to the blind search algorithm, for searching for new pulsars among our target sources.

4.3.2 Relocalization

Following the first few discoveries (summarized in Section 4.3.3), we noticed that the timing positions of a few pulsars (see Paper I for the timing positions of the discovered pulsars) were well outside the 95% confidence regions from the 3FGL catalog. The observed discrepancies could be caused by the fact that 3FGL catalog positions were determined using 4 years of Pass 7 reprocessed data, while we used 5.5 years of Pass 8 data, which have higher angular resolution. To mitigate this discrepancy we relocalized the sources using `Pointlike`, by varying the sky coordinates of the sources until the maximum likelihood was found. The results of the relocalization analysis for the new pulsars are given in Table 4.1.

In most cases, the relocalized positions are closer to the pulsar timing positions than the catalog ones. In addition, the 95% semi-major axes of the relocalized positions are smaller than in 3FGL. Although this implies a smaller number of trials in sky position for the blind search, leading to a greatly reduced overall computational cost, the true pulsar positions may still fall outside of the error ellipses. In some cases, the timing position is found to be out of both the 3FGL error ellipse and the ellipse from our analysis. From the 47^{th} source onwards, we therefore adopted the relocalized positions with three times the 1-σ Gaussian uncertainty reported by `Pointlike` to obtain a more conservative sky coverage, and also extended our dataset by including photons recorded until 2015 July 7 when the relocalization was done. The inaccurate source locations might have resulted from the imperfect Galactic background model.

4.3.3 Search summary

The blind search survey of the sources listed in the appendix, described in detail in Paper I, enabled the discovery of 17 gamma-ray pulsars. Clark et al. (2015) reported on the discovery of PSR J1906+0722, an energetic pulsar with a spin frequency of 8.9 Hz which suffered one of the largest glitches ever observed for a gamma-ray pulsar. Clark et al. (2016) later presented the discovery of PSR J1208−6238, a 2.3 Hz pulsar with a very high surface magnetic field and a measurable braking index of about 2.6. Paper I and the present paper report on 13 young, isolated gamma-ray pulsars also found in this survey. The new pulsars have rotational periods ranging from ∼79 ms to 620 ms. They are all energetic, with spin-down powers between about 10^{34} erg s^{-1} and 4×10^{36} erg s^{-1}. Among these, PSRs J1057−5851 and J1827−1446 are the slowest rotators among currently known gamma-ray pulsars. PSR J1844−0346 experienced a very large glitch in mid-2012 (see Paper I for details). In the next sections we describe dedicated follow-up studies of these 13 pulsars. Finally, we note that two more pulsars were found in this survey: PSRs J1035−6720 and J1744−7619. These two pulsars will

be presented in a separate publication (Clark et al., 2017 submitted).

4.4 Follow-up Analysis

4.4.1 Spectral Analysis

After selecting the 13 pulsars, we performed dedicated spectral analyses with extended datasets in order to characterize their spectral properties with extra sensitivity. We used updated Pass 8 (P8R2) event selections and updated IRFs for events recorded from 2008 August 4 until 2015 September 9. The sizes of the RoIs around each pulsar were extended to 15°to collect more gamma-ray photons for the follow-up analysis, and we selected photon energies > 100 MeV and zenith angles $< 90°$. The more restrictive zenith angle cut was used to better reject events from the Earth's limb in support of spectral analysis down to 100 MeV. In our dedicated spectral analyses we used the `gll_iem_v06.fits`[8] map cube and `iso_P8R2_SOURCE_V6_v06.txt`[9] template for modeling the Galactic diffuse emission and the isotropic diffuse background, to match with the current recommendations (Acero et al., 2016a). The numbers of point sources in the models were increased to include all 3FGL sources within 20°. The details of the timing analysis using these extended datasets, including the determination of timing and positional parameters, are presented in Paper I. For the spectral analysis of the 13 pulsars we used the positions obtained from pulsar timing. In order to further minimize contamination from the diffuse background or from neighboring sources, we restricted our datasets to the pulsed part of the pulse profiles. To determine the "on" and "off"-pulse phase regions of the pulse profiles, we selected gamma-ray photons with weights above 0.05 and constructed unweighted pulse profiles, which we then analyzed with the Bayesian Block decomposition method described by Scargle et al. (2013). Bayesian Blocks represent a model of time series of events generated by an inhomogeneous Poisson process, involving a sequence of constant flux levels. This method is useful for discriminating random flux changes from real ones, but it is not a physical representation of the pulse profiles. The on- and off-pulse regions are shown in Figure 4.1. We selected photons in the on-pulse regions and performed spectral analyses of these restricted datasets. We determined the significance of the spectral cutoff ($\mathrm{TS_{cut}}$) by comparing the change in log likelihood when using a simple power-law model for the spectra of the pulsars instead of assuming the PLEC model, as follows: $\mathrm{TS_{cut}} = -2 \log \Delta\mathcal{L}$. The results of the spectral analysis of the on-pulse data are given in Table 4.2; the corresponding SEDs are displayed in Figure 4.2, and the best-fit cutoff energy and power-law index values are shown in Figure 4.3 along with those of 2PC pulsars.

To search for unpulsed magnetospheric pulsar emission or emission from a putative PWN associated with the pulsar we conducted analyses of the off-pulse phases of the datasets. Point-like test sources were added to the spectral models at the locations of

[8] https://fermi.gsfc.nasa.gov/ssc/data/analysis/software/aux/gll_iem_v06.fits
[9] https://fermi.gsfc.nasa.gov/ssc/data/analysis/software/aux/iso_P8R2_SOURCE_V6_v06.txt

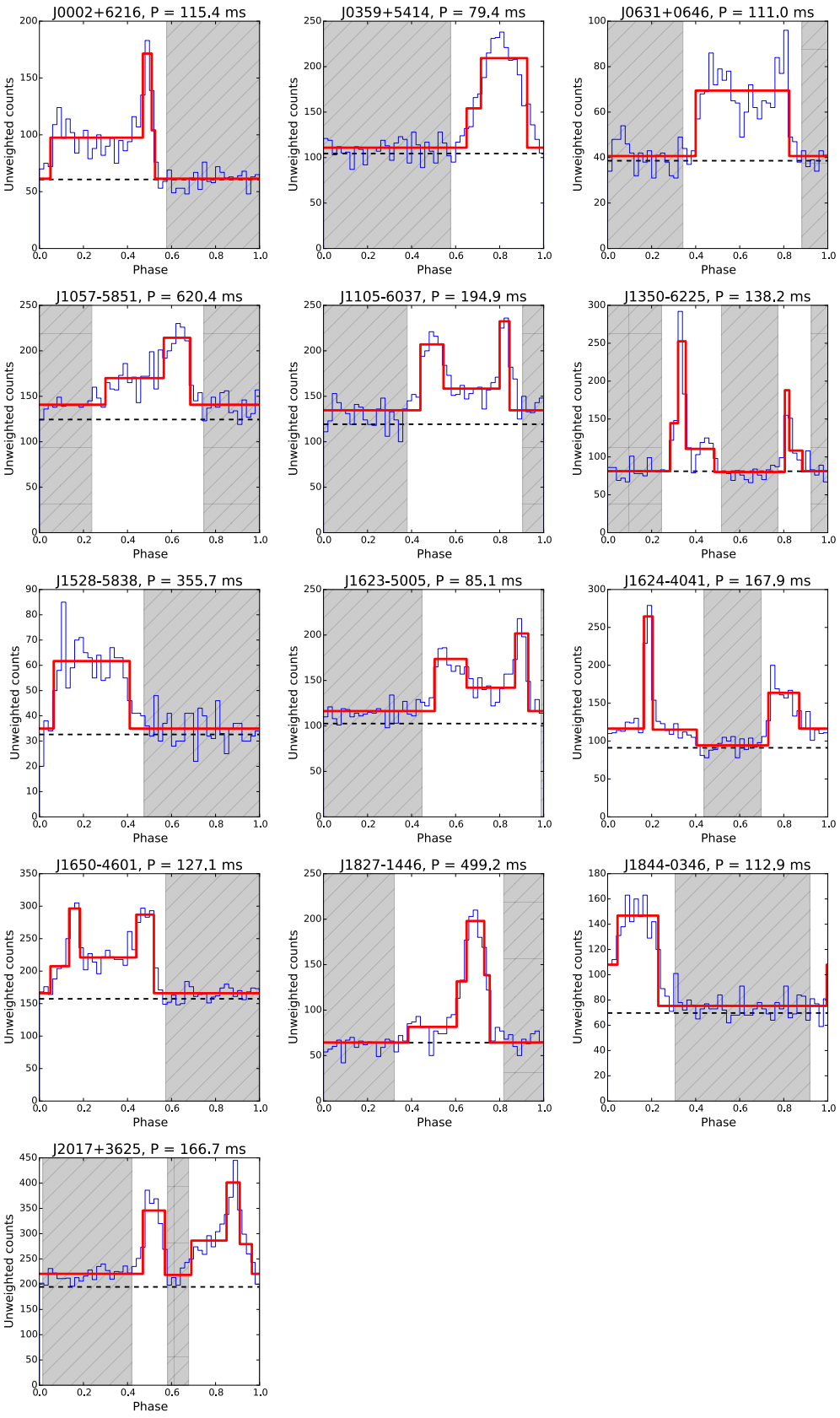

Figure 4.1 Results of the decomposition of gamma-ray pulse profiles into Bayesian blocks, as discussed in Section 4.4.1. Blue histograms represent the pulse profiles, red lines the Bayesian block decompositions, and shaded regions the off-pulse phase intervals determined from this analysis. Dashed black lines represent the estimated background levels, calculated as $B = \sum_i^N (1 - w_i)$ where w_i is the weight associated with photon i (Guillemot et al., 2012b).

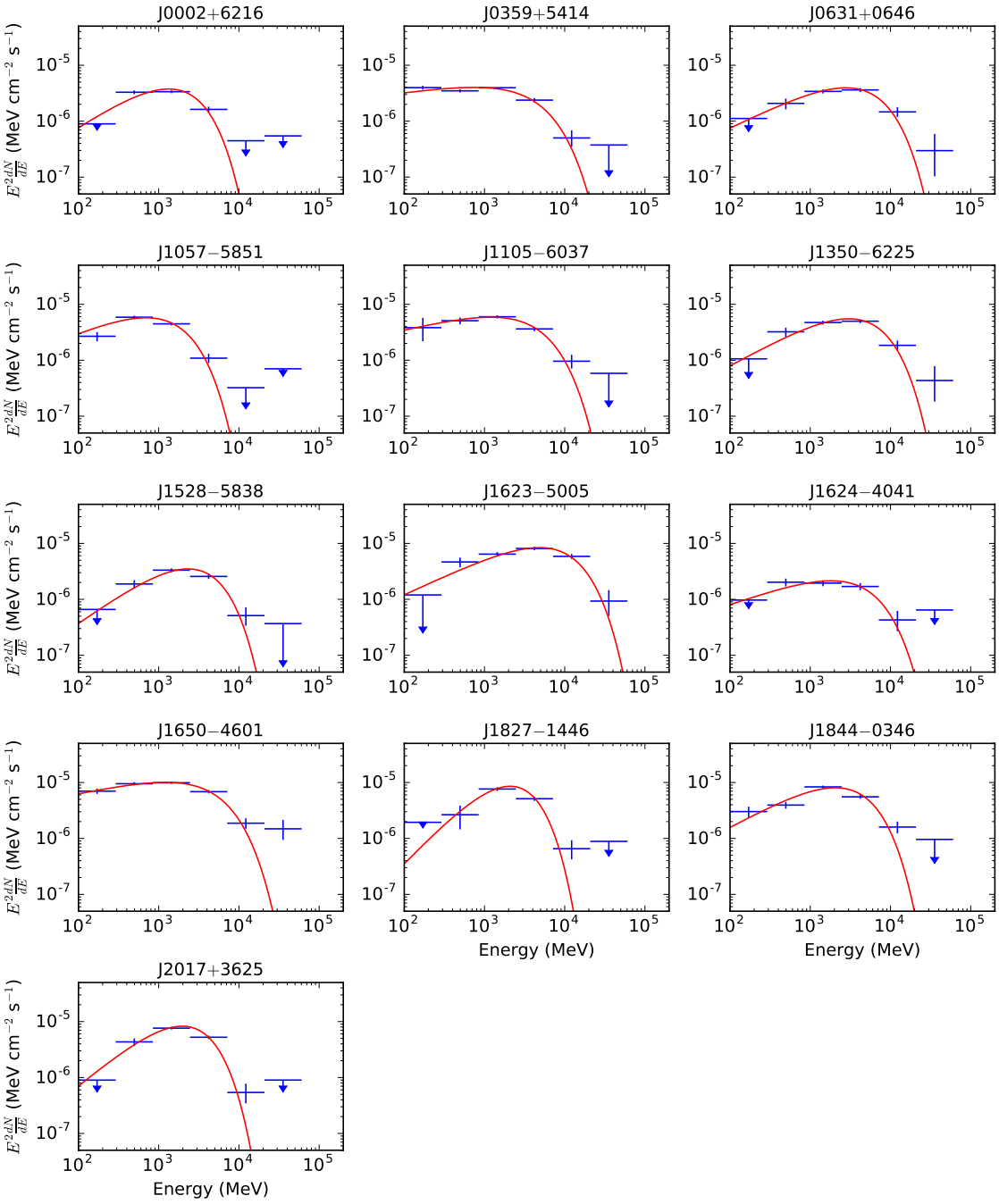

Figure 4.2 Spectral energy distributions for the 13 Einstein@Home pulsars presented in this paper. The best-fit spectral models obtained by analyzing the full energy range are shown as red lines. 95% confidence upper limits are calculated for energy bins with TS values below 4.

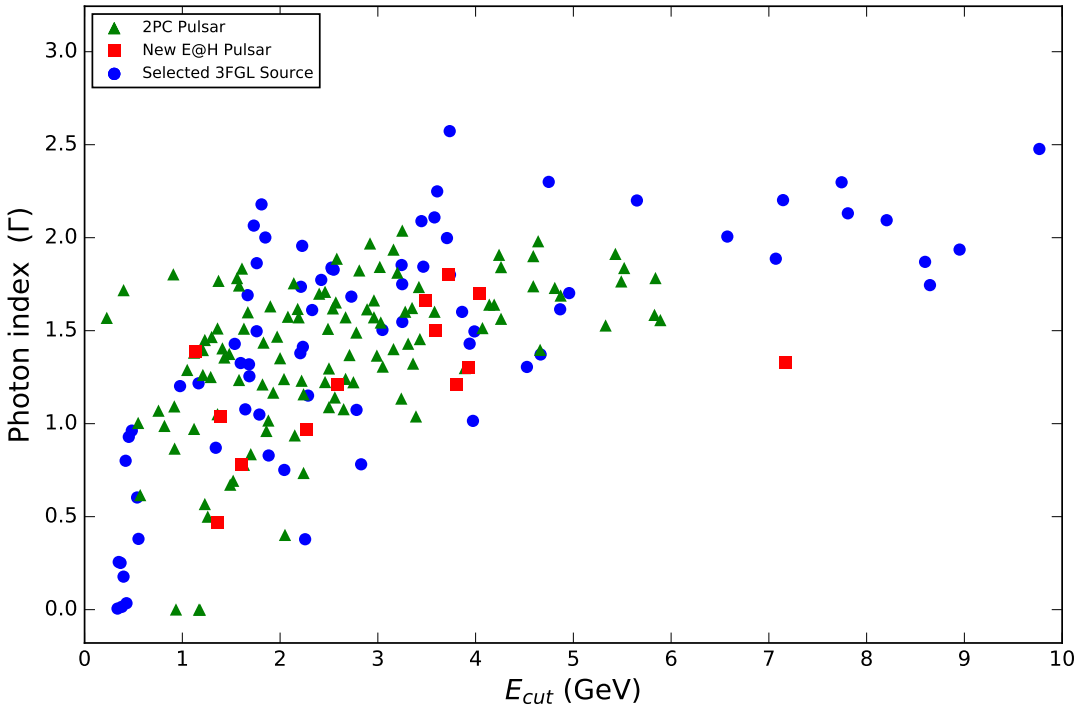

Figure 4.3 Best-fit power-law index Γ versus cutoff energy E_{cut} for the new pulsars (red squares), other selected 3FGL sources (blue circles) and known gamma-ray pulsars from 2PC (green triangles). 3FGL sources with cutoff energies above 10 GeV are not plotted and uncertainties are not displayed, to improve readability.

the pulsars, and the spectral properties of these sources were determined by running new likelihood analyses. We alternatively assumed a simple power-law model and a PLEC model for the test sources, in order to test for spectral curvature. Significant off-pulse emission was detected for PSRs J1623−5005, J1624−4041 and J2017+3625, with evidence for spectral curvature suggestive of magnetospheric emission from the pulsars, as can be seen from Table 4.3. Such off-pulse pulsar emission is not atypical for known gamma-ray pulsars (see, e.g., 2PC); nevertheless, small, un-modeled spatial fluctuations in the bright diffuse background emission could also account for this emission. Detailed analyses with extended datasets and comparisons of the best-fit spectral parameters with those of other known gamma-ray pulsars with off-pulse emission are necessary to firmly establish PSRs J1623−5005, J1624−4041 and J2017+3625 as pulsars exhibiting gamma-ray emission at all phases. The on-pulse emission was then re-fitted with the addition of sources detected in the off-pulse region scaled to the on-pulse interval with the normalization and spectral parameters fixed.

We characterized the pulse profiles displayed in Figure 5 of Paper I by fitting the weighted profiles to Gaussian or Lorentzian profiles, depending which gave a higher log likelihood. The derived peak multiplicities and gamma-ray peak separations are reported in Table 4.4. Most of the new pulsars show double-peaked profiles, with well-separated components that are typical of young gamma-ray pulsar light curves (see 2PC). Two of the 13 newly-discovered pulsars, PSRs J0002+6216 and J0631+1036, are detected in the radio band (see Section 4.4.2). For these pulsars we measured the phase offset between the radio peak and the first gamma-ray peak.

4.4.2 Radio counterpart searches

The new pulsars were searched for radio pulsations by reanalyzing archival observations from previous targeted radio surveys of *Fermi* LAT unassociated sources, or by conducting new dedicated observations. Because we have timing parameters for the new pulsars, the only parameter to search for when analyzing the radio observations is the Dispersion Measure (DM), a quantity representing the integrated column density of free electrons along the line of sight to the pulsars, causing radio waves to arrive at different times depending on the frequency. Radio observations were therefore folded at the periods determined from the gamma-ray timing (see Paper I) and searched in DM values only, resulting in a reduced number of trials compared to a typical radio pulsar search.

The list of telescopes and backends used is given in Table 4.5. For each observing configuration we give the gain G, the central frequency, the frequency bandwidth ΔF, the sensitivity degradation factor β, the number of polarizations n_p, the half width at half maximum of the radio beam (HWHM) and the receiver temperature $T_{\rm rec}$. Table 4.6 lists the radio observations processed in our follow-up study. Sensitivities were calculated using the modified radiometer equation given in Lorimer & Kramer (2005):

$$S_{\rm min} = \beta \frac{5 T_{\rm sys}}{G\sqrt{n_p t_{\rm int} \Delta F}} \sqrt{\frac{W}{P-W}} \tag{4.2}$$

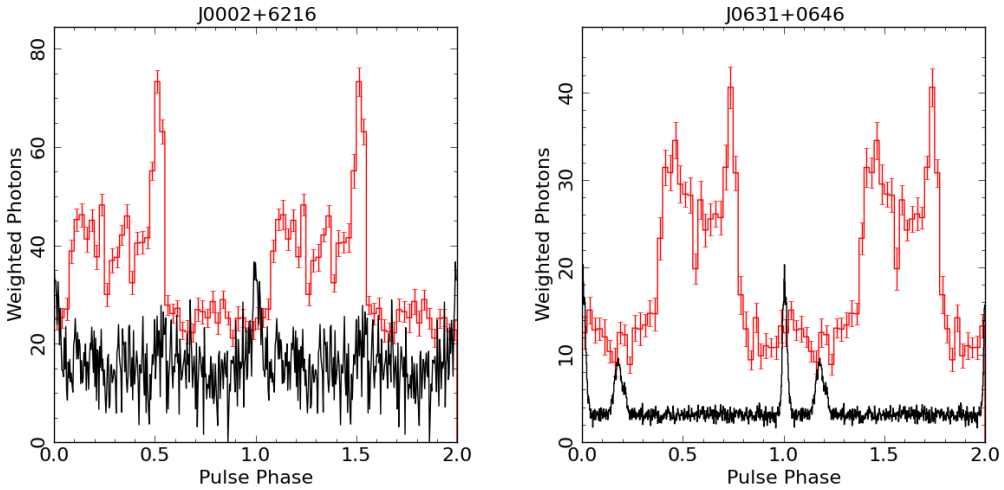

Figure 4.4 Radio and gamma-ray pulse profiles for PSRs J0002+6216 (left) and J0631+0646 (right). Weighted LAT gamma-ray pulse profiles (in red) were produced by selecting photons with weights greater than 0.05. Radio profiles (in black) correspond to 1.4 GHz observations made with the Effelsberg telescope for J0002+6216 and the Arecibo telescope for J0631+0646. Uncertainties in DM converted to uncertainties in the phase offset between the radio and gamma-ray peaks correspond to ∼1% of the rotational periods.

where a value of 5 is assumed for the threshold signal-to-noise ratio for a detection, $T_{\rm sys} = T_{\rm rec} + T_{\rm sky}$, $t_{\rm int}$ is the integration time, P is the rotational period and W is the pulse width, assumed to be $0.1 \times P$. The quantity $T_{\rm sky}$ is the temperature from the Galactic synchrotron component, estimated by scaling the 408 MHz map of (Haslam et al., 1982) to the observing frequency, assuming a spectral index of -2.6. For some observations the pointing direction was offset from the actual sky location of the pulsar. In those cases the flux density limit $S_{\rm min}$ as calculated using Equation (2) was divided by $e^{-(\theta/{\rm HWHM})^2/1.5}$, where θ is the offset. For the majority of pulsars we failed to detect pulsations in the radio data and placed limits on their radio flux densities.

For two pulsars, PSRs J0002+6216 and J0631+0646, the analysis resulted in the detection of significant radio pulsations. PSR J0002+6216 was detected in a 2-hr observation conducted at 1.4 GHz with the Effelsberg radio telescope, with a DM of 218.6(6) pc cm^{-3}. PSR J0631+0636 was detected with Arecibo at 327 MHz and at 1.4 GHz in ∼70 min observations, and was also seen with Effelsberg at 1.4 GHz during a 2-hr follow-up observation. The best determined DM value from the Arecibo 327 MHz observation was 195.2(2) pc cm^{-3}. Phase-aligned radio and gamma-ray pulse profiles for PSRs J0002+6216 and J0631+0646 are displayed in Figure 4.4. In both cases the gamma-ray emission is seen to lag the weak radio emission, as commonly observed in other radio and gamma-ray pulsars and suggesting radio and gamma-ray emissions having different magnetospheric origins (see, e.g., 2PC).

4.4.3 Pulse profile modeling

Using photons selected within 5°radius around the pulsars, we constructed weighted counts pulse profiles with 90, 60, or 30 bins if the weighted H-test TS, the statistical test for pulsation significance (de Jager et al., 1989), for a given pulsar was ≥1000, between 100 and 1000, or <100, respectively. For PSRs J0002+6216 and J0631+0646 with radio detections, we re-binned the radio pulse profiles to have the same number of bins as the corresponding gamma-ray profile. We performed likelihood fits, minimizing $-\ln\mathcal{L}$ where $\mathcal{L}$ is the likelihood value, of the gamma-ray pulse profile or the combination of the radio and gamma-ray pulse profiles, of all 13 pulsars using the geometric simulations and fitting technique of Johnson et al. (2014).

Following Clark et al. (2016), we used simulations with $P = 100$ ms and $\dot{P} = 10^{-15}$ s s^{-1} and constructed likelihood values using a χ^2 statistic. Each pulsar was fit using the outer gap (OG, e.g., Cheng et al., 1986) and the slot gap (e.g., Muslimov & Harding, 2003, 2004a) models, where we used the two-pole caustic model (TPC, Dyks & Rudak, 2003) as a geometric representation of the slot gap. For both models we use the vacuum retarded dipole solution for the magnetic field geometry (Deutsch, 1955). The simulations were produced with 1°resolution in both the magnetic inclination angle (α) and observer angle (ζ) and a resolution of 1% of the polar cap opening angle in emitting and accelerating gap widths. For radio simulations, we assumed a frequency of 1400 MHz with the conal geometry and emission altitude of **?**).

The best-fit results for all but PSR J0631+0646 are given in Table 4.7; estimated uncertainties are quoted at the 95% confidence level but note that systematic error estimates from the fitting method (see Johnson et al., 2014) and/or from fitting only the gamma-ray profiles (Pierbattista et al., 2015) could be as large as 10°. Johnson et al. (2014) noted that it was necessary to renormalize the $\Delta\ln\mathcal{L}$ surface, making the best fit approximately correspond to a reduced χ^2 value of 1, in order to have more realistic confidence contours. In some cases, however, we found that this renormalization was unnecessary, either having no effect on the estimated uncertainties or shrinking them. We denote the pulsars for which we did not renormalize the likelihood surface with a † in column 1 of Table 4.7. For each model, we also estimated the beaming fraction f_Ω (as defined, e.g., in Watters et al., 2009; Venter et al., 2009) for the best-fit geometry, used when calculating the gamma-ray luminosity.

For each pulsar with no radio detection, we examined the simulated radio sky map at 1400 MHz, and evaluated the model predictions for the best-fit geometry, in regard to expected radio loudness; the predictions are indicated in columns 6 and 11 of Table 4.7. The model predictions are: 'L' for radio-loud, meaning the predicted geometry has the radio cone clearly and strongly intersecting our line of sight; 'F' for radio-faint, meaning the predicted geometry has our line of sight either narrowly missing the cone or clipping the very edge suggesting only weak emission would be detected; and 'Q' for radio-quiet, meaning the predicted geometry has our line of sight clearly missing the radio cone. The radio-faint sources are of particular interest as searches at frequencies lower than 1400 MHz, where the cone is predicted to be larger (e.g., Story et al., 2007), may yield detections. Following Johnson et al. (2014), we conservatively consider one model to

be significantly favored over another, for a given pulsar, if the $\ln \mathcal{L}$ value is greater by at least 15; however, in some cases the best-fit geometry for the TPC model clearly predicts a radio-loud pulsar where none has been detected and we therefore claim the OG model is favored, regardless of the $\Delta \ln \mathcal{L}$ value. In particular, this is the case for PSRs J0359+5414, J1528−5838, and J1827−1446. For J1350−6225, both the TPC and OG model predict a radio-loud pulsar, with a near-orthogonal rotator viewed near the spin equator, either casting doubts on the models or raising questions concerning the non-detection. In modeling the "radio-quiet" pulsars in 2PC, Pierbattista et al. (2015) similarly found some solutions where the line of sight was near enough to the magnetic axis that we might expect to intersect the radio emission cone. These authors used a different fitting technique but similar simulations. This may further suggest that our results regarding the aforementioned pulsars point to issues with the models and not with the non-dections in radio.

Our joint gamma-ray and radio fits of PSR J0631+0646 did not produce acceptable results: the standard approach tended to ignore the radio data. Following Johnson et al. (2014), we decreased the radio uncertainty value in order to increase its importance in the likelihood but this proved ineffective, leading to fits that ignored the gamma-ray data. Under the assumption that the difficulty was in matching the observed phase lag between the radio peak and the gamma-ray peaks, we followed Guillemot et al. (2013) in allowing the phase of the magnetic pole in the radio and gamma-ray simulations to be different by as much as 0.1 (following realistic simulations of the pulsar magnetosphere by Kalapotharakos et al., 2012, which suggested an offset of the low-altitude polar gap from the outer magnetosphere by up to this amount). These new fits were, similarly, unsatisfactory. We investigated relaxing the maximum phase offset condition and found more acceptable fits with offsets of ∼0.3 in phase for both the TPC and OG models. The maximum phase offset of 0.1 is inferred from Kalapotharakos et al. (2012) by comparing predicted light curves from the vacuum retarded dipole geometry to models with increasing conductivity and finally full force-free models. It seems implausible that this offset could be a factor of 3 larger than predicted in the force-free simulations. Our different attempts to model the radio and gamma-ray profiles jointly being unsuccessful we do not report modeling results for PSR J0631+0646 in Table 4.7. New approaches for modeling this pulsar's emission geometry are needed. For instance, based on the work of Kalapotharakos et al. (2014), it is possible that gamma-ray emission from the current sheet outside the light cylinder could explain the extra phase lag for PSR J0631+0646 as their simulations did tend to show larger radio to gamma-ray phase lags.

4.4.4 Luminosity, distance and gamma-ray efficiency

The fraction of their energy budgets that pulsars convert into gamma-ray radiation is a key question for understanding pulsar emission mechanisms. This requires converting the measured energy flux in gamma rays G_{100} (see Table 4.2 for the values) into the gamma-ray luminosity, with the relation $L_\gamma = 4\pi f_\Omega G_{100} d^2$ where d is the distance. As discussed in Section 4.4.2, most of the 13 Einstein@Home pulsars considered in this

study are undetected in radio. For these pulsars we therefore cannot use the DM to infer distances, e.g., using the NE2001 model of free electrons in the Galaxy (Cordes & Lazio, 2002). We can however calculate "heuristic" distances, d_h, and luminosities, L^h_γ, as follows:

$$d_h = \sqrt{L^h_\gamma / 4\pi G_{100}}, \tag{4.3}$$

where

$$L^h_\gamma = \sqrt{\dot{E}/10^{33}\text{erg s}^{-1}} \times 10^{33} \text{ erg s}^{-1}, \tag{4.4}$$

i.e., assuming that the gamma-ray luminosity scales as $\sqrt{\dot{E}}$ for these young pulsars (see 2PC) and assuming a typical geometrical factor f_Ω of 1. Heuristic distances for the 13 pulsars are given in Table 4.4. In most cases the values suggest that the pulsars lie at small or intermediate distances, as is also the case for the majority of known gamma-ray pulsars.

From the radio detections of PSRs J0002+6216 and J0631+0646 we could determine DM values and use the NE2001 model to extract the DM distances given in Table 4.4. For both pulsars the NE2001 distance is very large. The distance for PSR J0002+6216 of 7.7 kpc leads to a gamma-ray efficiency $\eta = L_\gamma/\dot{E}$ of about 120%. For PSR J0631+0646 a conversion efficiency of 100% is found for a distance of about 6.7 kpc. The NE2001 model therefore probably underestimates the density of free electrons along the lines of sight to these pulsars. Interestingly, the recently-published model for the distribution of free electrons in the Galaxy of Yao et al. (2017) finds DM distances of 6.3 kpc and 4.6 kpc for PSR J0002+6216 and J0631+0646, respectively. The latter distance values lead to realistic efficiency estimates below 100% (81% and 90% respectively).

4.4.5 X-ray counterpart searches

We re-analyzed archival X-ray observations to search for counterparts to the new gamma-ray pulsars and to characterize their X-ray spectra. All our targets except PSR J1827−1446 have adequate coverage by at least one of the major contemporary observatories operating in the soft X-ray band: *Swift* (Burrows et al., 2005), *XMM-Newton* (Strüder et al., 2001; Turner et al., 2001) and *Chandra* (Garmire et al., 2003). The X-ray coverage ranges from few-ks shallow snapshots with *Swift* to orbit-long, deep observations by *Chandra* and *XMM-Newton*. Almost all the detected pulsars have been observed by *Swift* as part of a systematic survey of the gamma-ray error boxes of the unidentified *Fermi* LAT sources (Stroh & Falcone, 2013).

We reduced and analyzed the *XMM-Newton* data through the most recent release of the *XMM-Newton* Science Analysis Software (SAS) v15.0. We performed a standard data processing, using the `epproc` and `emproc` tools, and screening for high particle background time intervals following Salvetti et al. (2015). For the *Chandra* data analysis we used the Chandra Interactive Analysis of Observations (CIAO) software version 4.8. We re-calibrated event data by using the `chandra_repro` tool. *Swift* data were

processed and filtered with standard procedures and quality cuts[10] using FTOOLS tasks in the HEASOFT software package v6.19 and the calibration files in the latest Calibration Database release.

We performed a standard data analysis and source detection in the 0.3−10 keV energy range of the *XMM-Newton*-EPIC, *Chandra*-ACIS and *Swift*-XRT observations (e.g., Salvetti et al. 2015 and Marelli et al. 2015). We preferred the XMM and Chandra observatories if the same field has been observed because of the better performance in terms of effective area and spatial resolution. For each of the X-ray counterparts we performed a spectral analysis using XSPEC v12.9. After extracting response matrices and effective area files, we extracted X-ray fluxes by fitting the spectra with a power-law (PL) model using either a χ^2 or the C-statistic (Cash, 1979) in the case of low counts (< 100 photons) and negligible background. For sources characterized by low statistics (typically ≤ 30 photons), we fixed the column density to the value of the Galactic N_H integrated along the line of sight (Dickley & Lockman 1990) and scaled for the heuristic distance and, if necessary, set the X-ray PL photon index (Γ_X) to 2. All quoted uncertainties on the spectral parameters are reported at the 1σ confidence level. For each pulsar we computed the corresponding gamma-ray-to-X-ray flux ratio. As reported in Marelli et al. (2015), this could give important information on the nature of the detected pulsar. Finally, for all undetected ones, we computed the 3σ X-ray detection limit based on the measured signal-to-noise ratio, assuming a PL spectrum with $\Gamma_X = 2$ and the integrated Galactic N_H, scaled for the heuristic distance. The detailed results of these analyses are reported in Table 4.8.

Out of the 13 gamma-ray pulsars, we detected a significant X-ray counterpart for six. PSR J0002+6216, PSR J1105−6037 and PSR J1844−0344 were detected with *Swift*-XRT. These sources are listed in the First Swift XRT Point Source (1SXPS) Catalogue (Evans et al., 2014) as 1SXPS J000257.6+621609, 1SXPS J110500.3−603713 and 1SXPS J184432.9−034626, respectively. These sources are located at (α, δ) (J2000) = (0.7404°, +62.2692°), (166.2515°, −60.6203°) and (281.1371°, −3.7740°) with 90% confidence error circles of 4.9″, 6.4″ and 2.7″. Owing to the long *Chandra* exposure time, we clearly detected both the pulsar and the associated nebula of PSR J0359+5414. The pulsar is located at (α, δ) = (59.8586°, +54.2486°) with a 90% confidence error circle of 1″. The nebula is approximately elliptical, with semi-major and semi-minor axes of $\sim 15''$ and $\sim 7''$, respectively, roughly centered on the pulsar position. The nebula is well fitted by an absorbed PL model with photon index equal to 1.4±0.2 and unabsorbed flux in the 0.3−10 keV energy band of $(1.3\pm0.3)\times10^{-14}$ erg cm^{-2} s^{-1}. We also detected the counterpart for PSR J2017+3625 at (α, δ) = (304.4827°, 36.4189°), with a 2″ error, from analysis of a *Chandra* observation. From *XMM-Newton* data we detected two possible counterparts for PSR J1624−4041 at $\sim 13''$ from the gamma-ray pulsar position. The two plausible X-ray counterparts are located at (α, δ) = (246.0372°, −40.6931°) and (246.0459°, −40.6899°) with both a 0.8″ statistical plus 1.5″ systematic error. We report both counterparts in Table 4.8, as *src1* and *src2*, respectively.

[10]More detail in: http://swift.gsfc.nasa.gov/docs/swift/analysis/

4.5 Discussion

A total of 17 gamma-ray pulsars have been discovered among the 118 3FGL sources we have selected for the search, based on their gamma-ray emission properties being suggestive of pulsar emission. The high discovery rate of about 15% is comparable to that of previous similar surveys, of $\sim$ 8–12% (Abdo et al., 2009b; Pletsch et al., 2012b, 2013) even though we are searching fainter and fainter LAT sources. The improved semi-coherent blind search technique, the new Pass 8 LAT data, and the improved source selection and localization likely played an important role in the success of the survey. It is interesting to note that a number of sources in our list had already been searched for pulsations in the past. For example, comparing the sky locations searched in our survey with those analyzed in previous Einstein@Home or *Atlas* surveys (Pletsch et al., 2012b, 2013), we find that about 27% (32 / 118) of our sources had already been searched, and 11 of these have now been found to be gamma-ray pulsars. The multiple improvements in our new gamma-ray blind survey enumerated above likely explain the detections of these pulsars. Similarly, seven of the new discovered pulsars (PSRs J0002+6216, J0631+0646, J1035−6720, J1057−5851, J1105−6037, J1623−5005 and J1624−4041) fall below the sensitivity limit of the previously used search algorithm (see Section 5.1 of Paper I for more details).

Comparing our target list with the best pulsar candidates from Saz Parkinson et al. (2016) who also used machine learning techniques for classifying 3FGL unassociated sources, we find a relatively high overlap of about 60%. Interestingly, PSRs J0631+0646 and J1827−1446, discovered in our survey, do not appear in their list. In the case of PSR J0631+0646 this could be caused by the possible association with a nearby supernova remnant, while for PSR J1827−1446 the source detection significance of $\sim 9.1\sigma$ is simply under the 10σ threshold set by Saz Parkinson et al. (2016) for constructing their list. The good overlap between the two target lists makes us confident that we have selected and searched 3FGL sources likely powered by unknown pulsars.

The spectral properties (photon indices Γ and cutoff energies $E_{\rm cut}$) for the surveyed sources, for the 13 new gamma-ray pulsars and for pulsars from the 2PC catalog are displayed in Figure 4.3. The photon indices and cutoff energies of the new Einstein@Home pulsars are very similar to those of 2PC pulsars, a natural consequence of the source selection procedure described in Section 4.2.2. This is confirmed by a Kolmogorov-Smirnov test, which finds a $\sim$90% probability that the two samples are drawn from the same parent distribution. The GMM algorithm used for classifying 3FGL sources therefore seems to have efficiently selected pulsar candidates among unassociated sources, which is further supported by the fact that $\sim$ 80% of the discovered pulsars were found in the top half of Table 4.9. The gamma-ray fluxes of the new pulsars are generally lower than those of 2PC pulsars found in blind searches, also unsurprisingly.

Possible reasons for the non-detections of pulsars in other 3FGL unassociated sources listed in Table 4.9 are that these sources could be pulsars with low pulse fractions or broad gamma-ray pulse profiles, for which the sensitivity of the search algorithm is lower (see Section 3 of Paper I for a detailed discussion of the search sensitivity). They could also be pulsars with high timing noise, or they could be mil-

lisecond pulsars in binary systems. A number of sources in our list were indeed recently identified as candidate binary MSPs after we started our search: for instance, 3FGL J0212.1+5320 (Li et al., 2016), 3FGL J0744.1−2523 (Salvetti et al., 2017) and 3FGL J2039.6−5618 (Salvetti et al., 2015). The discovery of pulsars in binary systems in gamma rays requires initial guesses of the orbital parameters, from, e.g., optical or X-ray observations (see, e.g., Pletsch et al., 2012a). If all searched sources are indeed gamma-ray pulsars, then we would expect a good number of them to be in binaries, based on the 2PC pulsar population.

As can be seen from Figure 4.3 and Table 4.9, a number of sources included in our survey had Γ and/or $E_{\rm cut}$ parameters higher than those of 2PC pulsars. These sources were selected by the GMM based on their low variability and moderate curvature indices. Although the gamma-ray emission properties of these sources seem different from those of 2PC pulsars *a priori*, we included them in the survey for completeness but failed to find new pulsars in any of them. One possibility for the future would be to train the GMM not to select these peculiar sources, or to continue searching in order not to miss pulsars with large spectral index and/or cutoff values. In any case, half of the searched sources from Table 4.9 have Γ and $E_{\rm cut}$ parameters resembling those of 2PC pulsars, and are thus still prime targets for pulsation searches.

Of the 13 new pulsars reported in this article, only two have been detected in radio. The deep radio follow-up observations conducted as part of this project placed tight constraints on the flux densities of the undetected pulsars. Only six young pulsars among the 54 discovered in blind searches of the LAT data have so far been detected as radio pulsars. The many non-detections in radio are not surprising, given that past radio pulsar surveys have covered the entire sky with moderate sensitivity (see, e.g., Cordes et al., 2006; Keith et al., 2010; Barr et al., 2013; Boyles et al., 2013; Deneva et al., 2013). PSRs J0002+6216 and J0631+0646, both detected in radio, are however perfect examples of pulsars with low radio flux densities that would be missed in the short integration times of traditional radio pulsar surveys. The LAT was therefore crucial for the discovery of all these young pulsars, and blind search surveys are clearly key for completing the population of young and energetic gamma-ray pulsars. The discovery of these 13 pulsars with Einstein@Home brings the total number of non-recycled gamma-ray pulsars to 112, of which $\sim 54\%$ are radio-loud. The fraction thus remains similar to that reported in 2PC. As the *Fermi* mission continues it will be interesting to see how this fraction evolves, as it is a powerful discriminant of pulsar emission models.

Recently, Fermi-LAT Collaboration (2017) released a catalog of resolved point sources in a $40^\circ \times 40^\circ$region around the Galactic center direction. By selecting spectrally curved sources and comparing the spectral energy distributions of these point sources with those of a large sample of 3FGL sources, they could identify pulsar-like candidates from these new Galactic bulge sources. These sources are also prime targets for future blind pulsation searches.

4.6 Conclusions

Using information from a preliminary version of the 3FGL catalog of *Fermi* LAT sources, we have selected 118 targets with pulsar-like emission properties. We produced Pass 8 LAT datasets for each of the sources, and these datasets were then searched for pulsations with a multi-stage blind search algorithm, utilizing the volunteer computing system Einstein@Home. This survey led to the discovery of 17 pulsars, of which 13 are presented in this article, and the other pulsars have been or will be published elsewhere.

On-pulse and off-pulse gamma-ray spectral analyses were conducted for each of the new pulsars.The gamma-ray emission properties of the 13 newly discovered pulsars reported in this paper are similar to those of other young gamma-ray pulsars, such as those from the 2PC catalog. Radio follow-up observations were carried out, resulting in the detections of two of them with low radio flux densities. The pulse profiles of the 13 new pulsars were fit using the TPC and OG models. For some of the pulsars, radio emission is predicted by the models but is still undetected in follow-up or archival observations.

The increased sensitivity of the blind search algorithm, the improved Pass 8 LAT data, and improved source selection and relocalization pipeline enabled us to maintain a relatively high detection rate, compared to previous similar surveys. Nevertheless, for a number of the 3FGL sources with clear pulsar-like properties selected for the search, we were unable to find a pulsar. These sources remain excellent targets for future searches. New systematic surveys such as the one presented in this paper and in Paper I are warranted, and so are blind searches for millisecond pulsars in binary systems, which at the moment can only be searched using external constraints on the orbital parameters from observations at other wavelengths.

Table 4.1 Relocalization results

PSR	3FGL Source	r_{95} (3FGL)	r_{95} (new)	$\Delta_{\rm 3FGL}$	$\Delta_{\rm new}$
J0002+6216	J0002.6+6218	$3.6'$	$2.0'$	$2.7'$	$1.3'$
J0359+5414	J0359.5+5413	$2.4'$	$1.8'$	$1.8'$	$0.6'$
J0631+0646	J0631.6+0644	$2.8'$	$1.8'$	$4.1'$	$1.6'$
J1057−5851	J1056.7−5853	$5.2'$	$2.5'$	$4.4'$	$2.9'$
J1105−6037	J1104.9−6036	$2.7'$	$1.5'$	$0.7'$	$0.8'$
J1350−6225	J1350.4−6224	$2.4'$	$1.6'$	$2.0'$	$2.3'$
J1528−5838	J1528.3−5836	$3.3'$	$1.7'$	$1.7'$	$0.1'$
J1623−5005	J1622.9−5004	$1.5'$	$1.0'$	$1.7'$	$1.5'$
J1624−4041	J1624.2−4041	$2.7'$	$1.6'$	$0.9'$	$1.4'$
J1650−4601	J1650.3−4600	$2.1'$	$1.3'$	$1.0'$	$0.9'$
J1827−1446	J1827.3−1446	$3.7'$	$1.6'$	$1.2'$	$0.7'$
J1844−0346	J1844.3−0344	$3.4'$	$1.6'$	$2.8'$	$2.3'$
J2017+3625	J2017.9+3627	$2.1'$	$1.2'$	$2.4'$	$0.9'$

Note: Results of the relocalization analysis discussed in Section 4.3.2. For each of the 13 new pulsars reported in Paper I, column 2 lists the name of the 3FGL source in which the pulsar was discovered. Columns 3 and 4 list the semi-major axis of the 3FGL source error ellipse at 95% confidence (r_{95}) and the semi-major axis value from our analysis. The r_{95} (new) values are based on statistical uncertainties only. Columns 5 and 6 list the offset between pulsar timing positions and 3FGL positions ($\Delta_{\rm 3FGL}$) and the offset between pulsar timing positions and new positions ($\Delta_{\rm new}$).

Table 4.2 On-pulse spectral parameters

PSR	TS	TS_{cut}	Γ	E_{cut} (GeV)	Photon Flux, F_{100} (10^{-8} ph cm^{-2}s^{-1})	Energy Flux, G_{100} (10^{-11} erg cm^{-2}s^{-1})
J0002+6216	975	145	1.04 ± 0.16 ± 0.14	1.39 ± 0.21 ± 0.07	2.8 ± 0.3 ± 0.8	2.6 ± 0.2 ± 0.4
J0359+5414	1610	93	1.80 ± 0.07 ± 0.10	3.72 ± 0.61 ± 0.26	8.4 ± 0.6 ± 2.0	5.6 ± 0.2 ± 0.8
J0631+0646	881	81	1.30 ± 0.17 ± 0.12	3.93 ± 0.84 ± 0.33	2.9 ± 0.6 ± 0.6	3.7 ± 0.3 ± 0.3
J1057−5851	813	123	1.39 ± 0.16 ± 0.05	1.13 ± 0.19 ± 0.09	7.9 ± 0.9 ± 0.8	5.0 ± 0.3 ± 0.5
J1105−6037	1084	94	1.66 ± 0.11 ± 0.04	3.49 ± 0.60 ± 0.26	8.3 ± 1.2 ± 0.4	6.4 ± 0.5 ± 0.4
J1350−6225	704	85	1.21 ± 0.16 ± 0.44	3.80 ± 0.70 ± 1.13	4.2 ± 0.8 ± 4.1	6.0 ± 0.4 ± 2.1
J1528−5838	593	87	0.97 ± 0.07 ± 0.36	2.27 ± 0.12 ± 0.43	2.2 ± 0.5 ± 1.3	3.0 ± 0.3 ± 0.7
J1623−5005	854	106	1.33 ± 0.01 ± 0.29	7.17 ± 0.17 ± 1.48	4.7 ± 0.1 ± 3.3	8.1 ± 0.2 ± 2.0
J1624−4041	255	31	1.50 ± 0.21 ± 0.38	3.59 ± 1.07 ± 0.85	1.6 ± 0.8 ± 0.9	1.6 ± 0.5 ± 0.5
J1650−4601	1368	83	1.70 ± 0.10 ± 0.07	4.04 ± 0.71 ± 0.59	15.9 ± 1.4 ± 4.6	12.3 ± 0.6 ± 2.3
J1827−1446	818	134	0.47 ± 0.28 ± 0.32	1.36 ± 0.22 ± 0.15	3.7 ± 0.7 ± 1.0	5.8 ± 0.5 ± 0.6
J1844−0346	840	75	1.21 ± 0.22 ± 0.23	2.59 ± 0.53 ± 0.41	8.3 ± 1.9 ± 2.6	9.5 ± 0.9 ± 1.5
J2017+3625	1148	216	0.78 ± 0.15 ± 0.22	1.61 ± 0.18 ± 0.18	4.7 ± 1.3 ± 1.3	6.2 ± 1.1 ± 1.2

Note: Binned maximum likelihood spectral fit results for the 13 Einstein@Home gamma-ray pulsars. For each pulsar, columns 2 and 3 list the TS of the source, and the cutoff TS for the exponentially cut-off model over a simple power-law model. Columns 4 and 5 list the best-fit photon index Γ and cutoff energy E_{cut}. The next two columns give the on-pulse phase-averaged integral photon and energy fluxes in the 0.1 to 100 GeV band, F_{100} and G_{100}, scaled to full interval values. The first reported uncertainties are statistical, while the second uncertainties are systematic, determined by re-analyzing the data with bracketing IRFs and artificially changing the normalization of the Galactic diffuse model by ±6%, as described in Acero et al. (2016b).

Table 4.3 Off-pulse spectral parameters

PSR	TS	TS_{cut}	Γ	E_{cut} (GeV)
J1623−5005	57	18	*	0.87 ± 0.07 ± 0.21
J1624−4041	47	10	1.02 ± 0.95 ± 0.96	1.33 ± 1.23 ± 0.41
J2017+3625	215	88	0.69 ± 0.06 ± 0.06	0.59 ± 0.01 ± 0.06

Note: Results of the maximum likelihood analysis of the off-pulse phase ranges of pulsars with significant off-pulse emission, as discussed in Section 4.4.1. Column 1 lists the name of the pulsar. Columns 2-5 list the TS of the source in the off-pulse phase range, the test statistic TS_{cut} of an exponentially cut-off model over a simple power-law model, the photon index Γ and energy cutoff E_{cut}.
$*$ Although the spectral index is consistent with zero, the well-defined E_{cut} allows integration to a finite total flux.

Table 4.4 Pulse shape parameters and derived pulsar parameters

PSR	Peaks	δ	Δ	Off-pulse phase range	$\dot{E}$ (10^{33}erg s^{-1})	DM distance (kpc)	Heuristic distance, d_h (kpc)
J0002+6216	2	0.171 ± 0.011	0.361 ± 0.012	0.59–1.00	153	7.7, 6.3	2.0
J0359+5414	1	...	...	0.00–0.58	1318	...	2.3
J0631+0646	2	0.469 ± 0.013	0.278 ± 0.013	0.83–0.31	104	>42.2, 4.6	1.5
J1057−5851	1	...	...	0.75–0.24	17	...	0.8
J1105−6037	2	...	0.317 ± 0.006	0.90–0.38	116	...	1.2
J1350−6225	2	...	0.485 ± 0.002	0.92–0.24, 0.52–0.77	133	...	1.3
J1528−5838	2	...	0.243 ± 0.022	0.48–1.00	22	...	1.1
J1623−5005	2	...	0.352 ± 0.005	0.99–0.45	267	...	1.3
J1624−4041	2	...	0.429 ± 0.003	0.44–0.70	39	...	1.8
J1650−4601	2	...	0.331 ± 0.005	0.48–1.00	291	...	1.1
J1827−1446	2	...	0.256 ± 0.008	0.82–0.32	14	...	0.7
J1844−0346	1	...	...	0.31–0.92	4249	...	2.4
J2017+3625	2	...	0.374 ± 0.004	0.02–0.42, 0.58–0.68	12	...	0.7

Note: Columns 2-5 list the gamma-ray peak multiplicity, radio-to-gamma-ray phase lag (δ), gamma-ray peak separation (Δ) for pulse profiles with two components, and definition of the off-pulse phase interval, for each pulsar considered in our study. Uncertainties on δ and Δ are statistical only. Column 6 gives the spin-down power for each pulsar. Column 7 lists the DM distances for the radio-detected pulsars J0002+6216 and J0631+1036 as inferred with the NE2001 model of Cordes & Lazio (2002) and the model of Yao et al. (2017). The last column lists the heuristic distance, described in Section 4.4.4.

Table 4.5 Definition of Radio Observation Codes

Obs Code	Telescope	Gain (K Jy^{-1})	Frequency (MHz)	Bandwidth ΔF (MHz)	β	n_p	HWHM (arcmin)	$T_{\rm rec}$ (K)
AO-327	Arecibo	11	327	68	1.12	2	6.3	116
AO-ALFA	Arecibo	10	1400	100	1.12	2	1.5	30
AO-Lwide	Arecibo	10	1510	300	1.12	2	1.5	27
Eff-7B	Effelsberg	1.5	1400	240	1.05	2	9.1	22
Eff-L1	Effelsberg	1.5	1400	240	1.05	2	9.1	22
GBT-820	GBT	2.0	820	200	1.05	2	7.9	29
GBT-S	GBT	1.9	2000	700	1.05	2	3.1	22
GMRT-322	GMRT	1.6	322	32	1	2	40	106
GMRT-610	GMRT	1.6	607	32	1	2	20	102
Nancay-L	Nancay	1.4	1398	128	1.05	2	2×11	35
Parkes-AFB	Parkes	0.735	1374	288	1.25	2	7	25
Parkes-BPSR	Parkes	0.735	1352	340	1.05	2	7	25
Parkes-DFB4	Parkes	0.735	1369	256	1.1	2	7	25

Note: Radio telescopes and backend parameters used for follow-up observations of the new pulsars, described in Section 4.4.2.

Table 4.6 Radio Search Observations of the New Pulsars

Target PSR	Obs Code	Date	$t_{\rm int}$ (min)	R.A. (J2000)	Decl. (J2000)	Offset (arcmin)	$T_{\rm sky}$ (K)	$S_{\rm min}$ (μJy)
J0002+6216	GBT-S	2013 Feb 28	28	00:02:40.3	62:16:44.0	2.2	0.9	Detected
	Eff-L1	2015 Feb 14	120	00:02:58.1	62:16:09.6	0.0	2.4	Detected
J0359+5414	Eff-7B	2010 May 25	32	03:59:35.8	54:10:40.8	4.5	2.0	34
	Eff-7B	2010 Jul 17	60	03:59:31.5	54:11:44.1	3.3	2.0	23
	GBT-S	2012 Nov 17	40	03:59:36.3	54:12:56.5	2.5	0.8	18
	GBT-S	2013 Mar 17	7	03:59:36.3	54:12:56.5	2.5	0.8	42
	Eff-L1	2015 Feb 14	115	03:59:26.0	54:14:55.6	0.0	2.0	15
J0631+0646	Eff-L1	2015 Feb 13	120	06:31:52.4	06:46:15.3	0.0	1.8	Detected
	AO-327	2015 Mar 15	75	06:31:52.4	06:46:14.0	0.0	78.4	Detected
	AO-Lwide	2015 Jun 14	69	06:31:52.4	06:46:14.0	0.0	1.5	Detected
J1057−5851	Parkes-DFB4	2015 Aug 05	70	10:57:09.3	−58:51:11.0	0.1	3.9	49
	Parkes-DFB4	2015 Aug 06	51	10:57:09.3	−58:51:11.0	0.1	3.9	58
J1105−6037	Parkes-DFB4	2015 Aug 05	70	11:05:00.5	−60:37:15.6	0.0	5.7	52
	Parkes-DFB4	2015 Aug 06	60	11:05:00.5	−60:37:15.6	0.0	5.7	56
J1350−6225	Parkes-AFB	2010 Nov 19	145	13:49:36.0	−62:24:00.0	8.1	10.5	110
	Parkes-BPSR	2010 Nov 19	144	13:49:36.0	−62:24:00.0	8.1	10.9	86
	Parkes-DFB4	2015 Sep 05	433	13:50:44.5	−62:25:43.7	0.0	10.6	24
	Parkes-DFB4	2015 Sep 13	500	13:50:44.5	−62:25:43.7	0.0	10.6	23
J1623−5005	Parkes-BPSR	2010 Nov 19	144	16:22:48.0	−50:06:00.0	2.7	16.9	45
	Parkes-AFB	2010 Nov 19	88	16:22:48.0	−50:06:00.0	2.7	16.2	74
J1624−4041	Parkes-AFB	2009 Dec 02	120	16:24:06.2	−40:40:48.0	1.0	4.1	41
	GBT-S	2009 Dec 23	30	16:24:06.0	−40:40:48.0	1.0	1.5	15
	Parkes-AFB	2010 Jul 18	120	16:24:03.0	−40:42:56.0	1.9	4.1	43
	Parkes-AFB	2010 Jul 26	120	16:24:03.0	−40:42:56.0	1.9	4.1	43
	Parkes-AFB	2010 Nov 12	60	16:24:03.0	−40:42:56.0	1.9	4.1	60
	GMRT-610	2011 Feb 15	60	16:24:03.8	−40:41:20.4	1.2	34.4	297
	Parkes-AFB	2012 Jul 12	60	16:24:09.0	−40:40:23.0	1.1	4.1	58
	GMRT-322	2012 Jul 12	60	16:24:09.0	−40:40:23.0	1.1	178.6	618
	Parkes-AFB	2012 Dec 17	60	16:24:09.0	−40:40:23.0	1.1	4.1	58
J1650−4601	Parkes-BPSR	2010 Nov 21	144	16:50:48.0	−46:06:00.0	6.9	14.4	74
	Parkes-AFB	2010 Nov 21	139	16:50:48.0	−46:06:00.0	6.9	13.8	96
J1827−1446	GBT-820	2014 Apr 21	35	18:27:20.2	−14:46:01.2	1.2	33.2	60
	Eff-L1	2015 Feb 14	120	18:27:24.6	−14:46:25.4	0.0	8.3	19
J1844−0346	Eff-7B	2010 May 15	32	18:44:15.4	−03:42:46.8	5.7	11.8	53
	Eff-7B	2010 Jul 30	60	18:44:21.8	−03:42:03.6	5.2	11.8	37
	Eff-7B	2010 Jul 31	60	18:44:21.8	−03:42:03.6	5.2	11.8	37
	GBT-S	2012 Nov 17	22	18:44:26.2	−03:45:21.6	2.0	4.7	24
	Eff-7B	2015 Aug 27	120	18:44:33.0	−03:46:32.0	0.0	11.8	21
J2017+3625	Nancay-L	2010 May 05	65	20:17:55.8	36:25:08.0	0.0	4.6	50
	Nancay-L	2010 May 11	47	20:17:55.8	36:25:08.0	0.0	4.6	58
	GBT-S	2010 May 13	60	20:17:59.0	36:25:19.0	0.7	1.8	10
	GBT-820	2011 Jan 15	45	20:17:57.6	36:27:36.0	2.5	18.6	43
	AO-ALFA	2015 May 11	20	20:17:54.2	36:23:24.0	1.8	4.6	34
	AO-327	2015 Jun 24	15	20:17:55.9	36:27:32.4	2.4	202.7	170
	AO-327	2015 Jun 25	15	20:17:55.9	36:27:32.4	2.4	202.7	170
	Eff-7B	2015 Aug 27	120	20:17:55.8	36:25:08.0	0.0	4.6	17
	AO-327	2015 Nov 16	28	20:17:55.9	36:25:08.4	0.0	202.7	113
	AO-Lwide	2015 Nov 17	33	20:17:55.9	36:25:08.4	0.0	3.8	5

Note: Radio observations of the new pulsars. In the cases of PSRs J0002+6216 and J0631+0646, radio pulsations were detected (see Section 4.4.2).

Table 4.7 Light Curve Modeling Results

PSR	TPC $-\ln\mathcal{L}$	TPC α (°)	TPC ζ (°)	TPC f_Ω	TPC Radio Flag	OG $-\ln\mathcal{L}$	OG α (°)	OG ζ (°)	OG f_Ω	OG Radio Flag
J0002+6216	110.26	64^{+3}_{-2}	54 ± 2	1.05 ± 0.04	···	105.70	69^{+8}_{-1}	58^{+25}_{-1}	$1.08^{+0.05}_{-0.27}$	···
J0359+5414†	39.88	1 ± 1	2 ± 1	$19.62^{+0.01}_{-8.52}$	L	38.04	80^{+8}_{-6}	24 ± 4	$1,01^{+0.09}_{-0.41}$	Q
J1057−5851†	32.62	57^{+2}_{-3}	40^{+7}_{-2}	$0.95^{+0.05}_{-0.18}$	F	42.94	$65^{+2}+-1$	28^{+1}_{-2}	$0.76^{+0.10}_{-0.03}$	Q
J1105−6037	46.11	61^{+4}_{-27}	49^{+21}_{-7}	$0.98^{+0.05}_{-0.31}$	F	67.40	8^{+5}_{-2}	71^{+4}_{-1}	$0.99^{+0.01}_{-0.09}$	Q
J1350−6225	79.42	82^{+2}_{-4}	85^{+1}_{-2}	0.82 ± 0.10	L	48.16	90 ± 9	88^{+1}_{4}	0.70 ± 0.03	L
J1528−5838†	29.71	2 ± 1	2 ± 1	$3.77^{+0.01}_{-0.28}$	L	27.21	9^{+9}_{-6}	74^{+6}_{-3}	$0.95^{+0.04}_{-0.09}$	Q
J1623−5005	31.28	32^{+2}_{-1}	68 ± 1	$0.62^{+0.02}_{-0.01}$	Q	58.83	9^{+12}_{-1}	72^{+3}_{-1}	$0.21^{+0.19}_{-0.01}$	Q
J1624−4041	86.57	71^{+2}_{-5}	58^{+1}_{-5}	1.13 ± 0.03	F	72.90	86 ± 1	68 ± 1	$1.02^{+0.02}_{-0.01}$	F
J1650−4601	46.30	13^{+2}_{-7}	69 ± 1	$0.47^{+0.01}_{-0.09}$	Q	54.13	11^{+2}_{-4}	74^{+6}_{-3}	$0.21^{+0.19}_{-0.16}$	Q
J1827−1446†	52.65	1 ± 1	2 ± 1	$69.16^{+0.01}_{-5.67}$	L	45.04	75^{+1}_{-11}	26^{+5}_{-1}	$1.34^{+0.01}_{-0.71}$	Q
J1844−0346†	23.06	10 ± 1	68 ± 1	0.49 ± 0.07	Q	22.08	79^{+6}_{-4}	22^{+1}_{-3}	$0.99^{+0.31}_{-0.39}$	Q
J2017+3625	168.10	23 ± 5	69 ± 1	$0.52^{+0.16}_{-0.01}$	Q	127.47	16^{+12}_{-5}	80^{+1}_{-5}	$0.23^{+0.10}_{-0.04}$	Q

Light curve fitting results for all pulsars except PSR J0631+0646. Column 1 gives the pulsar name, a † indicates that the $\Delta\ln\mathcal{L}$ surface was not renormalized. Column 2 (7) gives the best-fit $-\ln\mathcal{L}$ value for the TPC (OG) model. Columns 3, 4, and 5 (8, 9, and 10) give the best-fit α and ζ with corresponding f_Ω for the TPC (OG) model. For pulsars without a radio detection, column 6 (11) gives a radio-loudness prediction from the best-fit geometry for the TPC (OG) model: L = radio-loud, F = radio-faint, and Q = radio-quiet; see the text for details.

Table 4.8 Summary of the pulsar X-ray spectral parameters

PSR	X-ray observatory[a]	Exposure (ksec)	N_H (10^{21} cm^{-2})	Γ_X	F_X[b] (10^{-14} erg cm^{-2} s^{-1})	G_{100}/F_X[c]
J0002+6216	*Swift*	9.2	1.0[c]	2[c]	$4.3^{+1.9}_{-2.4}$	600^{+760}_{-200}
J0359+5414	*Chandra*	29.7	2.0±1.1	2.7±0.3	0.96±0.20	5800±1500
J0631+0646	*Swift*	3.5	0.4[c]	2[c]	<9.1	>400
J1057–5851	*Chandra*	10.1	3.0[c]	2[c]	<0.25	>20000
J1105–6037	*Swift*	16	1.0[c]	2[c]	$4.8^{+1.9}_{-1.4}$	1300^{+550}_{-380}
J1350–6225	*Swift*	5.4	1.4[c]	2[c]	<8.1	>740
J1528–5838	*Swift*	6	0.7[c]	2[c]	<6.2	>480
J1623–5005	*XMM-Newton*	85.4	4.0[c]	2[c]	<2.0	>4100
J1624–4041	*XMM-Newton*	31.0	2.0[c]	(src1) 0.7±0.2 (src2) 2.0±0.4	3.7±0.7 1.0±0.3	430±100 1600±690
J1650–4601	*Swift*	3.5	1.0[c]	2[d]	<10.8	>1100
J1827–1446	–	–	–	–	–	–
J1844–0344	*Swift*	82	2.4[c]	2[c]	7.6±1.3	1300±260
J2017+3625	*Chandra*	10.0	1.0[c]	2[c]	1.7±0.7	3600±2600

Results of the analysis of archival X-ray observations. Columns 1 and 2 list the pulsar name and the X-ray observatory. Columns 3-5 list the duration of the exposure, and for each X-ray counterpart the best-fit column density and photon index. The following two columns give the unabsorbed X-ray flux in the 0.3–10 keV energy band, and the gamma-ray-to-X-ray flux ratio. All uncertainties are reported at the 68% confidence level.

[a]We report only the X-ray observatory used for the spectral analysis.
[b]When the X-ray counterpart is not detected, we report the minimum X-ray unabsorbed flux required for a 3σ detection.
[c]Gamma-ray energy fluxes in 0.1–100 GeV are used to calculate the gamma-ray-to-X-ray flux ratio.
[d]Due to the low statistics in these sources, we fixed this parameter in the spectral analysis as described in the text.

Table 4.9: Ranked source list

3FGL Name	Searched R.A. (J2000)	Searched Decl. (J2000)	Search Radius (arcmin)	VI	TS_{curve}	TS_{cut}	E_{cut} (GeV)	Γ	TS	log R_S	Class
J1745.3−2903c	17:45:22.32	−29:03:46.80	2.05	48.42	275.2	378.7	2.2	1.4	3407	18.85	...
J1746.3−2851c	17:46:22.51	−28:51:45.72	2.12	57.06	113.0	364.7	4.0	1.5	2373	14.31	pwn
J2017.9+3627	20:17:56.33	+36:27:32.76	3.10	39.86	179.3	198.9	1.9	1.4	1876	13.61	...
J1839.3−0552†	18:39:23.52	−05:52:53.76	3.07	37.43	83.7	135.1	2.3	1.2	714	13.26	...
J1906.6+0720†	19:06:41.14	+07:20:02.04	3.33	41.70	87.9	68.6	7.0	2.0	1580	12.51	...
J1910.9+0906†	19:10:58.61	+09:06:01.80	1.55	52.13	53.2	17.4	41.7	2.1	4790	12.31	snr
J1636.2−4734†	16:36:16.49	−47:34:49.08	4.58	54.63	106.0	47.1	7.1	1.9	1180	12.28	snr
J1848.4−0141	18:48:28.39	−01:41:33.72	7.27	52.63	109.0	13.8	9.8	2.5	1457	11.81	...
J1405.4−6119†	14:05:25.46	−61:19:00.48	2.83	43.93	61.1	19.7	8.2	2.1	1671	11.39	...
J1111.9−6038†	11:11:58.44	−60:38:27.96	1.96	46.69	81.4	58.5	10.4	1.9	3624	11.36	spp
J1748.3−2815c	17:48:22.20	−28:15:32.04	2.73	34.06	77.4	68.6	4.7	1.4	489	11.26	...
J1622.9−5004†	16:22:54.31	−50:04:31.08	2.17	54.35	72.4	73.3	8.0	1.6	891	10.21	...
J0223.6+6204†	02:23:37.46	+62:04:51.96	3.51	41.77	86.3	182.6	1.8	1.5	1089	9.78	...
J1823.2−1339†	18:23:16.90	−13:39:04.68	2.60	47.54	29.7	47.4	9.0	1.9	1004	9.72	...
J1745.1−3011	17:45:11.30	−30:11:57.84	6.17	59.68	92.7	88.8	0.6	0.4	459	9.69	spp
J1800.8−2402†	18:00:53.18	−24:02:06.36	3.13	46.65	36.4	21.3	11.3	1.7	575	9.69	...
J1749.2−2911	17:49:15.58	−29:11:34.44	7.21	41.77	50.9	43.6	1.6	1.3	265	9.62	...
J1306.4−6043†	13:06:27.50	−60:43:54.12	2.48	35.69	65.9	42.6	8.6	1.7	1108	9.59	...
J1104.9−6036†	11:04:59.42	−60:36:32.76	4.10	43.09	77.4	64.6	3.6	1.7	769	9.42	...
J0634.1+0424	06:34:06.79	+04:24:22.32	9.77	42.87	123.3	60.2	1.8	2.2	1421	9.41	...
J1552.8−5330	15:52:50.90	−53:30:47.16	6.98	46.44	56.6	50.3	1.8	1.0	210	9.26	...
J1747.0−2828†	17:47:05.98	−28:28:54.84	3.65	90.61	159.7	135.3	2.5	1.8	1676	9.22	...
J1650.3−4600	16:50:23.76	−46:00:50.76	3.14	55.06	54.6	55.0	4.8	1.8	897	9.19	...
J2323.4+5849	23:23:28.85	+58:49:09.48	1.49	40.07	62.4	39.1	26.4	1.6	2568	9.17	snr
J1625.1−0021†	16:25:07.06	−00:21:30.96	3.38	37.31	104.3	201.4	1.9	0.8	1778	8.98	...
J1714.5−3832	17:14:34.27	−38:32:55.68	2.65	68.77	39.3	23.3	14.7	2.2	2649	8.95	snr
J1857.9+0210†	18:57:57.65	+02:10:13.44	5.41	50.62	42.8	50.5	3.2	1.9	601	8.89	...
J1056.7−5853	10:56:42.86	−58:53:45.60	7.77	35.71	88.2	126.1	1.1	1.5	596	8.83	...
J1026.2−5730	10:26:14.33	−57:30:59.76	4.85	50.42	54.7	58.1	2.3	1.6	493	8.26	...
J1742.6−3321	17:42:39.60	−33:21:22.32	6.00	48.24	67.1	24.4	2.5	1.8	411	8.20	...

Continued on next page

3FGL Name	Searched R.A. (J2000)	Searched Decl. (J2000)	Search Radius (arcmin)	VI	TS_{curve}	TS_{cut}	E_{cut} (GeV)	Γ	TS	log R_S	Class
J1844.3−0344†	18:44:23.93	−03:44:48.48	5.09	44.78	37.0	70.9	1.9	0.8	468	8.12	...
J1101.9−6053	11:01:55.46	−60:53:45.96	7.49	23.32	40.8	61.3	2.4	1.8	519	7.95	spp
J2038.4+4212	20:38:29.95	+42:12:30.60	5.30	45.67	51.1	95.8	0.5	0.6	340	7.92	...
J1849.4−0057	18:49:25.30	−00:57:06.48	3.55	45.11	23.8	16.6	13.5	2.0	674	7.86	snr
J1112.0−6135	11:12:04.03	−61:35:03.12	8.87	55.72	84.6	35.8	1.7	1.7	293	7.84	...
J1754.0−2538	17:54:02.02	−25:38:54.96	2.62	66.89	72.4	107.3	4.0	1.0	500	7.73	...
J0854.8−4503†	08:54:50.59	−45:03:41.76	4.37	44.94	47.5	54.9	5.0	1.7	737	7.68	...
J1857.2+0059	18:57:14.28	+00:59:10.68	3.82	57.14	32.6	113.2	4.5	1.3	383	7.67	...
J1740.5−2843	17:40:30.00	−28:43:01.20	5.87	46.42	25.6	24.2	3.6	2.2	700	7.66	...
J1744.1−7619†	17:44:10.85	−76:19:42.96	3.12	51.73	112.5	169.2	2.1	1.2	1759	7.61	...
J1035.7−6720†	10:35:42.24	−67:20:00.60	3.34	47.01	80.6	120.2	2.3	1.4	1336	7.39	...
J1843.7−0322	18:43:42.77	−03:22:37.92	7.67	70.63	65.5	54.5	3.7	2.6	1113	7.37	...
J0359.5+5413†	03:59:31.46	+54:13:19.20	3.66	33.63	42.2	84.1	2.6	1.6	800	7.19	...
J1624.2−4041†	16:24:14.26	−40:41:11.40	4.02	50.80	58.8	74.2	2.8	1.6	945	7.18	...
J1740.5−2726	17:40:32.28	−27:27:00.00	8.30	43.15	39.9	31.1	1.8	2.0	401	7.04	...
J1827.3−1446	18:27:20.16	−14:46:01.92	5.54	40.00	18.2	83.5	2.5	1.4	483	6.96	...
J2032.5+3921	20:32:29.78	+39:25:20.60	3.69	49.41	46.2	34.1	0.4	0.8	233	6.95	...
J1638.6−4654	16:38:40.16	−46:54:06.33	2.24	77.58	48.0	46.8	3.7	1.8	614	6.84	spp
J1925.4+1727	19:24:58.98	+17:24:41.84	7.38	47.33	42.2	22.3	1.2	1.2	157	6.70	...
J1857.9+0355	18:58:03.73	+03:55:08.04	3.45	55.58	31.5	29.6	1.6	1.1	146	6.55	...
J1208.4−6239†	12:08:26.89	−62:39:26.13	1.56	64.44	39.2	52.0	4.9	1.8	874	6.43	...
J1350.4−6224†	13:50:34.69	−62:23:43.53	1.71	58.24	41.3	90.8	2.4	0.7	357	6.41	...
J1037.9−5843*	10:38:01.49	−58:44:20.62	4.29	38.88	24.9	163.9	0.4	0.0	391	6.32	...
J2112.5−3044†	21:12:32.39	−30:43:58.53	1.39	51.84	69.0	151.0	2.8	1.1	1805	6.25	...
J1636.2−4709c	16:36:22.32	−47:09:53.05	4.41	57.44	13.7	4.4	–	2.3	541	6.17	spp
J1358.5−6025	13:58:24.20	−60:25:30.56	2.44	53.16	32.8	21.1	5.7	2.2	639	6.15	...
J1048.2−5928	10:48:40.66	−59:26:03.43	3.98	65.78	101.1	60.4	1.5	1.4	381	6.11	...
J2034.6+4302	20:34:58.42	+43:05:08.99	6.30	41.40	50.7	112.7	0.4	0.3	324	6.11	...
J1754.0−2930†	17:54:14.33	−29:32:08.04	3.72	59.67	49.8	38.4	2.2	2.0	498	6.06	...
J1214.0−6236†	12:14:10.04	−62:36:16.69	1.98	58.02	20.3	15.7	13.1	2.2	789	6.05	spp
J1652.8−4351	16:52:32.63	−43:56:50.10	6.40	64.55	31.0	62.0	1.3	0.9	184	6.00	...

Continued on next page

3FGL Name	Searched R.A. (J2000)	Searched Decl. (J2000)	Search Radius (arcmin)	VI	TS_{curve}	TS_{cut}	E_{cut} (GeV)	Γ	TS	log R_S	Class
J1317.6−6315	13:17:35.62	−63:17:18.00	2.96	50.53	25.0	37.0	2.7	1.7	347	5.99	...
J2039.4+4111	20:39:45.84	+41:09:34.39	3.61	45.39	48.2	98.1	0.3	0.3	249	5.91	...
J1852.8+0158*	18:52:27.92	+02:01:37.54	4.17	54.52	12.1	0.2	–	2.8	838	5.89	...
J0631.6+0644	06:31:49.76	+06:44:46.66	1.93	43.04	26.6	37.2	4.6	1.6	676	5.84	spp
J1840.1−0412*	18:40:06.15	−04:11:35.22	2.95	30.14	15.9	0.0	–	2.5	416	5.83	spp
J1928.9+1739	19:29:02.93	+17:34:58.90	9.16	47.86	26.9	12.0	3.6	2.1	235	5.79	...
J0225.8+6159	02:26:20.37	+62:00:10.48	3.49	46.69	28.8	29.7	2.2	1.7	473	5.77	...
J0002.6+6218†	00:02:48.88	+62:16:54.71	2.25	48.02	58.0	80.3	1.8	1.5	716	5.76	...
J1740.5−2642	17:40:41.52	−26:39:52.98	4.29	33.42	23.2	34.1	2.5	1.8	222	5.74	...
J1834.5−0841*	18:34:31.66	−08:40:15.75	4.02	57.10	0.5	0.1	–	2.2	287	5.72	snr
J2042.4+4209	20:42:39.77	+42:09:19.64	11.48	49.90	27.1	27.4	0.5	1.0	185	5.68	...
J1814.0−1757c	18:13:24.52	−17:53:55.97	5.83	56.91	8.8	7.4	–	2.3	662	5.59	...
J2041.1+4736†	20:41:08.34	+47:35:50.81	2.01	56.28	38.0	15.9	10.3	2.3	967	5.53	...
J1047.3−6005	10:47:21.66	−60:05:11.01	6.22	49.04	22.3	16.4	3.0	1.5	115	5.52	...
J2039.6−5618	20:39:36.25	−56:17:12.94	1.82	34.60	30.4	60.3	3.9	1.6	1266	5.47	...
J1900.8+0337	19:00:37.96	+03:39:10.57	3.94	45.87	44.9	4.7	–	2.3	186	5.42	...
J0855.4−4818	08:55:18.44	−48:14:13.02	10.69	33.84	53.0	66.4	0.5	0.9	288	5.39	...
J1747.7−2904	17:47:51.94	−29:01:49.54	2.95	65.34	10.3	124.7	7.1	2.2	666	5.37	...
J0541.1+3553	05:40:47.47	+35:54:40.72	8.53	35.17	37.3	33.0	1.8	1.9	329	5.34	...
J1549.1−5347c*	15:48:38.12	−53:44:00.33	5.02	51.64	10.9	0.1	–	2.9	1172	5.27	spp
J1039.1−5809	10:38:25.85	−58:08:23.45	13.63	37.46	24.7	23.4	1.7	1.3	107	5.23	...
J1831.7−0230	18:31:33.96	−02:31:25.54	5.83	31.11	17.8	2.1	–	2.7	421	5.23	...
J1702.8−5656†	17:02:45.00	−56:54:39.46	1.88	58.78	46.9	53.1	3.4	2.1	1917	5.19	...
J1736.0−2701*	17:36:07.44	−27:03:29.55	6.88	38.45	25.2	23.7	0.3	0.0	80	5.18	...
J2023.5+4126*	20:23:24.65	+41:27:31.08	4.35	48.95	78.1	36.7	0.4	0.0	93	5.12	...
J1758.8−2346	17:59:09.58	−23:47:19.28	3.69	41.80	11.8	5.4	–	1.9	218	5.01	...
J2004.4+3338*	20:04:22.03	+33:39:29.46	1.47	50.29	13.5	0.0	–	2.4	708	5.01	...
J0212.1+5320	02:12:12.29	+53:20:49.61	1.58	51.47	45.9	82.0	3.3	1.5	1442	5.01	...
J1901.1+0728	19:01:09.32	+07:30:01.23	3.29	55.34	25.8	10.5	6.6	2.0	134	4.88	...
J1503.5−5801	15:03:39.92	−58:00:43.22	3.88	67.48	26.3	18.7	3.7	2.0	359	4.85	...
J1850.5−0024	18:50:31.56	−00:24:33.69	4.83	64.27	14.6	2.8	–	2.3	216	4.76	...
J0933.9−6232†	09:34:00.41	−62:32:57.43	1.77	59.20	88.0	125.9	2.0	0.8	907	4.73	...

Continued on next page

3FGL Name	Searched R.A. (J2000)	Searched Decl. (J2000)	Search Radius (arcmin)	VI	TS_{curve}	TS_{cut}	E_{cut} (GeV)	Γ	TS	log R_S	Class
J1620.0−5101	16:19:48.66	−51:00:57.34	4.03	50.48	9.7	1.0	–	2.1	121	4.72	...
J1726.6−3530c	17:26:32.27	−35:33:37.61	5.18	60.31	11.9	1.8	–	2.6	335	4.67	...
J1919.9+1407	19:20:11.19	+14:11:54.53	7.95	67.73	17.6	0.3	–	2.7	642	4.66	...
J1119.9−2204†	11:19:59.45	−22:04:25.17	1.80	62.62	103.2	156.9	1.7	1.3	1949	4.63	...
J0907.0−4802*	09:07:18.05	−47:58:38.32	10.11	40.75	29.3	28.0	0.4	0.2	123	4.58	...
J1718.0−3726	17:18:02.10	−37:26:50.06	1.02	41.58	1.5	2.0	–	2.1	593	4.55	snr
J1859.6+0102	18:59:39.72	+01:00:15.56	5.43	68.61	18.9	13.1	3.5	1.8	150	4.40	...
J2035.0+3634	20:35:02.11	+36:32:12.74	1.88	52.58	39.2	57.5	2.8	0.8	401	4.39	...
J1345.1−6224	13:44:43.61	−62:28:30.64	5.12	58.30	12.8	1.3	–	2.7	568	4.39	spp
J0744.1−2523	07:44:06.64	−25:25:17.47	1.97	61.34	40.9	55.3	3.2	1.8	666	4.27	...
J0426.7+5437	04:26:33.79	+54:35:00.35	3.01	51.83	63.9	59.0	1.7	2.1	1235	4.27	...
J1539.2−3324†	15:39:20.23	−33:24:56.62	1.64	57.87	102.9	129.3	2.3	0.4	694	4.22	...
J1641.1−4619c*	16:41:00.45	−46:19:46.25	1.87	39.43	0.7	0.2	–	2.3	292	4.15	spp
J1528.3−5836	15:28:23.37	−58:38:05.98	1.87	68.72	44.9	41.4	4.0	1.6	452	4.14	...
J1857.9+0355	18:58:03.73	+03:55:08.04	3.45	41.47	11.2	32.2	2.2	1.4	131	4.13	...
J1855.4+0454	18:55:12.72	+04:55:38.38	4.46	38.60	6.6	4.4	–	2.4	193	4.12	...
J1650.0−4438c*	16:49:48.42	−44:38:58.44	6.63	58.81	1.0	0.1	–	3.1	843	4.02	...
J0901.6−4700	09:01:40.90	−46:52:10.77	7.02	55.10	30.0	52.7	1.0	1.2	221	4.02	...
J1329.8−6109	13:29:57.92	−61:08:00.95	2.45	55.66	22.5	21.1	4.9	1.6	246	3.91	...
J1639.4−5146	16:39:25.17	−51:46:04.03	1.39	58.03	4.2	2.8	–	2.3	945	3.85	...
J1833.9−0711*	18:34:10.57	−07:11:34.47	3.12	82.07	1.6	0.4	–	2.3	482	3.85	spp
J1814.1−1734c	18:14:07.87	−17:36:39.99	2.96	50.07	7.1	5.3	–	1.4	83	3.73	...
J1139.0−6244	11:39:07.61	−62:46:04.02	2.31	29.45	7.5	16.5	8.6	1.9	278	3.71	...
J1626.2−2428c	16:26:25.40	−24:31:36.54	4.74	46.87	15.9	7.8	–	2.1	392	3.66	...
J1212.2−6251	12:12:18.06	−62:53:31.51	2.84	53.70	1.4	12.9	45.8	2.4	426	3.45	spp

Note: List of the 118 3FGL sources with log $R_S > 0$ searched for gamma-ray pulsars using Einstein@Home, ranked by their probability to be pulsars according to the GMM analysis presented in Section 4.2.2. Sources marked with a † symbol were searched in a previous Einstein@Home & *Atlas* survey for gamma-ray pulsars. Sources for which suspiciously low or high cutoff energies were measured are marked with asterisks. We highlight in bold face the 3FGL sources in which pulsars were discovered in this survey. The discovery and analysis of PSRs J1906+0722 and J1208−6238 are presented in Clark et al. (2015) and Clark et al. (2016), while PSRs J1035−6720 and PSR J1744−7619 discovered in 3FGL J1035.7−6720 and 3FGL J1744.1−7619 will be presented in a future publication. Columns 2 to 4 list the searched position and radius. Columns 5 and 6 give the variability index, VI, and curvature TS, TS_{curve}, from a preliminary version of the 3FGL catalog. Columns 7 to 10 give the TS of the spectral cutoff (TS_{cut}), the cutoff energy (E_{cut}), the photon index (Γ) and the source TS value from our binned maximum likelihood analysis with `Pointlike`; cutoff energies are listed for sources with $TS_{cut} > 9$. Column 11 lists the pulsar likelihood value from our GMM analysis. Column 12 lists association flags from the 3FGL catalog: "pwn" and "snr" labels indicate possible associations with pulsar wind nebulae (PWN) and supernova remnants (SNR) respectively, sources with class "spp" are special cases with potential PWN or SNR associations. Sources below the horizontal line were searched with relocalized positions, as mentioned in Section 4.3.2.

Chapter 5

Discovery Highlights From *Einstein@Home*

In Chapter 4, I described the discovery of 13 new Einstein@Home pulsars presented in Clark et al. (2017) and Wu et. al. (2017, accepted). Four more pulsars were found as part of the 118 3FGL sources searched in the Einstein@Home γ-ray pulsar blind search survey. Due to their unique timing characteristics, further individual studies were carried out and follow-up analysis result were presented separately. Contents presented in this chapter are based on three publications as part of the Einstein@Home γ-ray pulsar blind search survey (Clark et al., 2015; Clark et al., 2016, Clark et al., 2017, submitted). The collection of pulsars presented in this chapter demonstrated the quality of the source selection algorithm, the performance of the search algorithm and the importance of finding pulsars in γ-rays. My main contributions in these publications are initial source selection, preparation of the search dataset, follow-up phase-averaged and off-pulse γ-ray spectral analysis and the interpretation of the spectral analysis result. Search datasets used in this chapter were produced using the method described in Section 4.3.1., with follow-up analysis with the method described in Section 4.4.1.

Section 5.1 corresponds to an article published on the Astrophysical Journal Letter with the title: PSR J1906+0722: An Elusive γ-ray Pulsar, C. J. Clark, H. J. Pletsch, ***J. Wu****, et al. ApJL, Vol. 809, 1, 2015*

Section 5.2 corresponds to an article published on the Astrophysical Journal Letter with the title: The Braking Index of A Radio-quiet Gamma-ray Pulsar, C. J. Clark, H. J. Pletsch, ***J. Wu****, et al. ApJL, Vol. 832, 1, 2016*

Section 5.3 corresponds to an article submitted to Science Advance with the title: Einstein@Home Discovers a Radio-quiet Gamma-ray Millisecond Pulsar, C. J. Clark, H. J. Pletsch, ***J. Wu****, et al. Science Advance, submitted, 2017*

Contents

5.1 A γ-ray Pulsar With Giant Glitch – PSR J1906+0722

5.1.1 Pulsar properties

3FGL J1906.6+0720, now associated with PSR J1906+0722, and was also known as 2FGL J1906.5+0720, is one of the most significant unassociated 2FGL sources. It was included in the "bright" pulsar-like source list presented by Romani (2012). It was long suspected to be a γ-rays pulsar due to its spectral properties in γ-ray. This source has been searched for pulsations, in both radio and γ-rays (Barr et al., 2013; Pletsch et al., 2012b; Xing & Wang, 2014). From the 120 minutes L-band follow-up observation at the 100-m Effelsberg radio telescope, there were no evidence for radio pulsation using the γ-ray timing solution. I computed the radio flux density limit of ≈ 21 μJy using the radiometer equation (equation 4.2). Which is below the radio-quiet threshold of 30 μJy used in 2PC (Abdo et al., 2013).

In the original γ-ray search dataset described in Chapter 4, clear pulsations were observed only after April 2010. To further investigate the temporal behaviour of the signal, an extended dataset was created of which included γ-ray photons observed up to 1 October 2014. As the pulsations were detected in part of the data, glitch analysis was performed to located possible glitch(es), as described in Clark et al. (2015). A glitch was found around MJD 55067^{+2}_{-9} ($\sim$24 August 2009), with a relative magnitude of $\Delta f/f \approx 4.5 \times 10^{-6}$. The time versus rotational phase diagram based on the timing solution is shown in Table 5.1 and the evolution of the pulse signal is displayed in Figure 5.2. Parameters derived from the timing analysis suggested that PSR J1906+0722 is a young, energetic, isolated pulsar, with a spin frequency of 8.9 Hz, a characteristic age of 49 kyr, and spin-down power 1.0×10^{36} erg s^{-1}.

From the phase-average spectral analysis, PSR J1906+0722 was found to have a relatively high cutoff energy ($E_c = 6.5 \pm 0.9$ GeV) compared to typical γ-ray pulsars. This suggests that the γ-ray spectrum could be contaminated by a nearby undetected γ-ray source, also noted by Xing & Wang (2014). This is supported by the fact that the timing position of PSR J1906+0722 fall well outside of the 95% confidence region of 3FGL J1906.6+0720, as illustrated in Figure 5.1. Off-pulse analysis was carried out with the aim of identify any possible undetected putative source in the surroundings. I analysed the off-pulse part of the data by restricting photons coming form the off-pulse interval defined using the Bayesian block decomposition method mentioned in Section 4.4.1. A residual test statistic (TS) map for the off-pulse region revealed a putative source $0.28 \pm 0.02^{\circ}$away from the pulsar position.

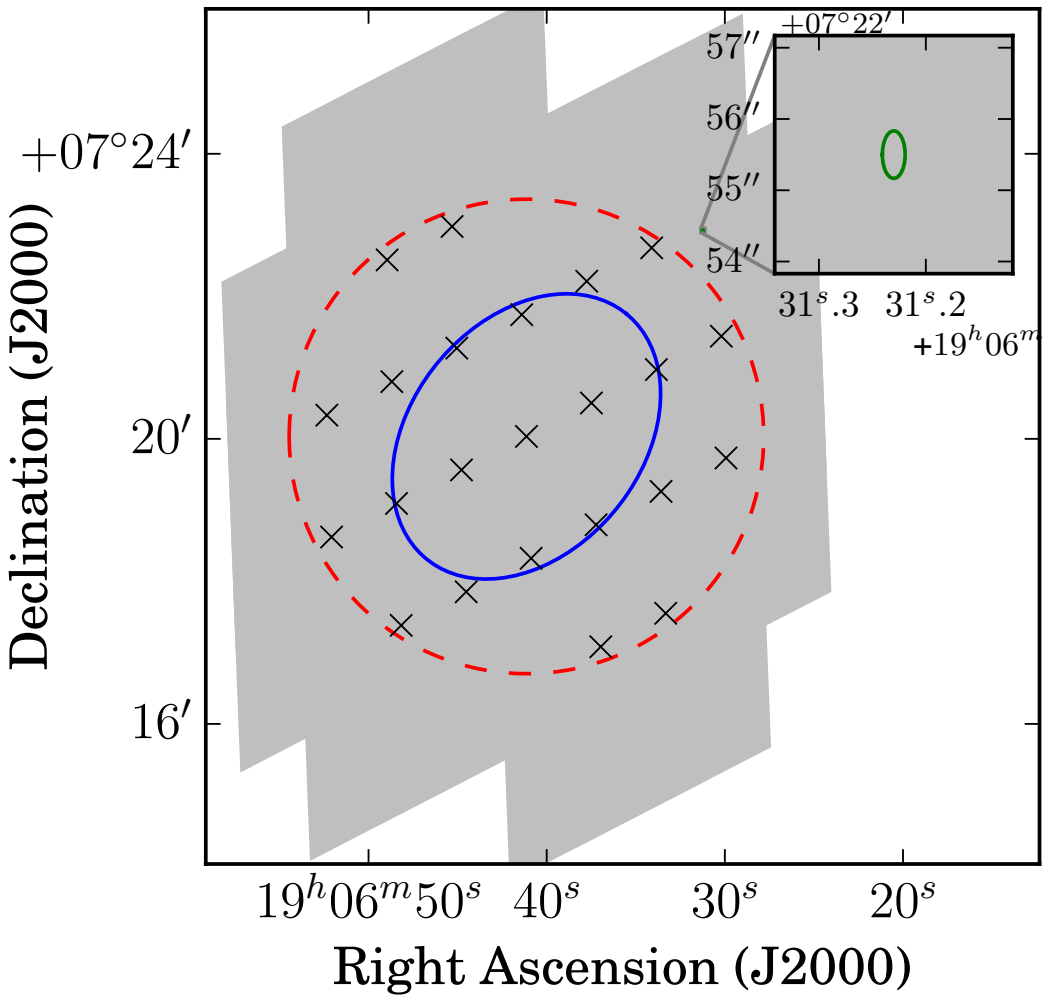

Figure 5.1 Sky map of PSR J1906+0722, the dotted ellipse shows the 95% confidence region of 3FGL J1906.6+0720. The dashed ellipse shows the sky region where the search gird (crosses) was constructed for the semi-coherent search. Grey area shows the sky area can be reached in the follow-up stage when optimizing the candidate's position. The inset shows the 1σ ellipse of PSR J1906+0722 result from the timing analysis. Plot reproduced from Clark et al. (2015).

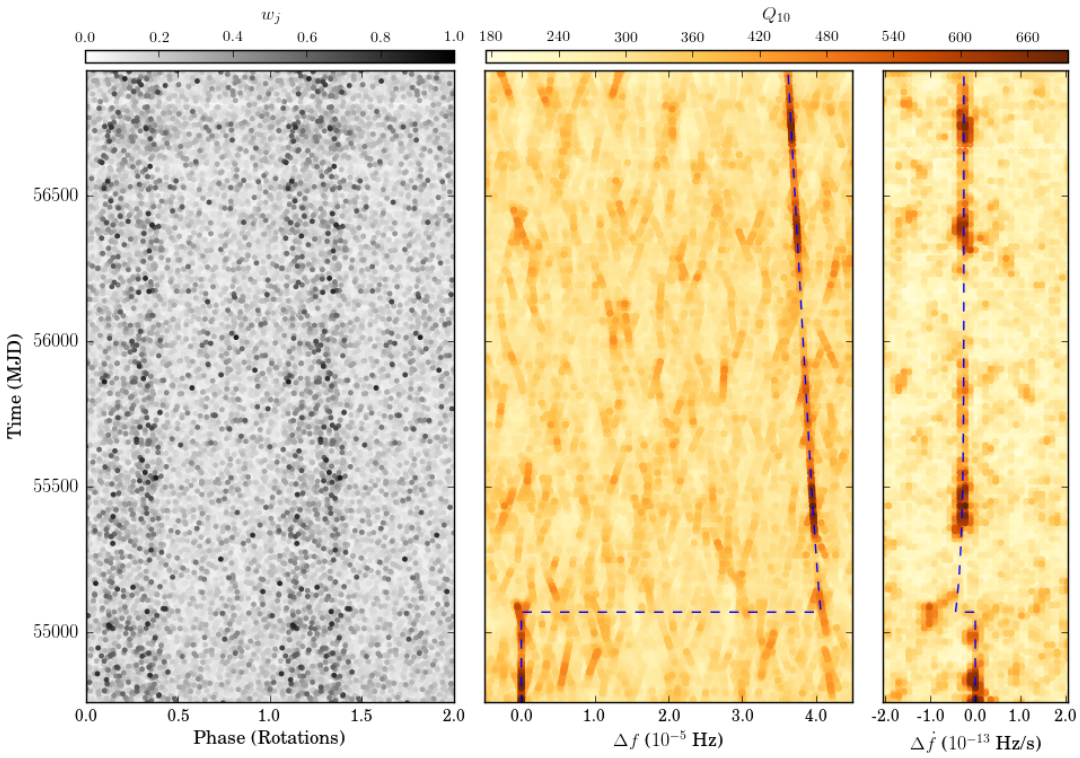

Figure 5.2 Evolution of the PSR J1906+0722's pulsed signal throughout the *Fermi* mission, including the glitch at MJD 55067. Left: Phase verses time where each point represents one photon, with the intensity representing the photon weight, two rotations are shown for clarity. Center and right: The strength of the signal is quantified with Q_{10}-test shown by the colour bar (Pletsch & Clark, 2014) in f and $\dot{f}$ space, centered on the pre-glitch parameters, in overlapping 150 day segments. The dashed line indicates the timing solution listed in Table 5.1 (Clark et al., 2015).

Table 5.1 Parameters for PSR J1906+0722 (Clark et al., 2015)

Parameter	Value
Range of Photon Data (MJD)	54682 – 56931
Reference epoch (MJD), $t_{\rm ref}$,	55716
Timing Parameters[a]	
Right Ascension, α (J2000.0)	$19^{\rm h}\,06^{\rm m}\,31^{\rm s}.20(1)$
Declination, δ (J2000.0)	$+07°22'55.''8(4)$
Frequency, f (Hz)	8.9666688432(1)
1st frequency derivative, $\dot{f}$, (Hz s^{-1})	$-2.884709(2) \times 10^{-12}$
2nd frequency derivative, $\ddot{f}$, (Hz s^{-2})	$3.18(1) \times 10^{-23}$
Glitch Parameters[a]	
Glitch epoch (MJD)	55067^{+2}_{-9}
Permanent f increment, Δf (Hz)	$4.033(1) \times 10^{-5}$
Permanent $\dot{f}$ increment, $\Delta\dot{f}$ (Hz s^{-1})	$-2.56(3) \times 10^{-14}$
Decaying f increment, $\Delta f_{\rm d}$ (Hz)	$3.64(9) \times 10^{-7}$
Glitch decay time constant, $\tau_{\rm d}$ (days)	221(12)
Spectral Properties[b]	
Spectral index, Γ	1.9 ± 0.1
Cutoff energy, $E_{\rm c}$ (GeV)	5.5 ± 1.2
Photon flux, F_{100} (photons cm^{-2} s^{-1})	$(1.1 \pm 0.3) \times 10^{-7}$
Energy flux, G_{100} (erg cm^{-2} s^{-1})	$(7.3 \pm 1.3) \times 10^{-11}$
Derived Properties	
Period, P (ms)	111.524136498(1)
1st period derivative, $\dot{P}$ (s s^{-1})	$3.587895(2) \times 10^{-14}$
Weighted H-test	731.2
Characteristic age, $\tau_{\rm c}$ (kyr)	49.2
Spin-down power, $\dot{E}$ (erg s^{-1})	1.02×10^{36}
Surface B-field strength, $B_{\rm S}$ (G)	2.02×10^{12}
Light-cylinder B-field, $B_{\rm LC}$ (G)	1.34×10^{4}
Heuristic distance, $d_{\rm h}$ (kpc)	1.91

Values for timing parameters are the mean values of the marginalized posterior distributions from the timing analysis, with 1σ uncertainties in the final digits quoted in parentheses.

[a] Glitch model parameters are defined in Edwards et al. (2006), with the correction noted by Yu et al. (2013).

[b] Fluxes above 100 MeV, F_{100} and G_{100}, were calculated by extrapolation from the E $>$ 200 MeV spectrum. The choice of the energy threshold is explained in Section 5.1.1.

The secondary source was then included in the source model with a power-law spectrum at the detected location, with its spectral index and normalization as free parameters. I then redid the spectral analysis in the full phase interval data. The 200 MeV energy threshold was used to improve angular resolution in order to better separate the pulsar emission from that of the secondary source. I found that the log-likelihood value increased and the new photon weights increased the S/N of the pulsations, strongly indicate that the inclusion of the secondary source does improve the overall fit. Figure 5.4 shows TS maps and SEDs for PSR J1906+0722 and the secondary source found in the off-pulse analysis. The location of the secondary source is very close to the western edge of the supernova remnant (SNR) G41.1-0.3 (Safi-Harb et al., 2005). Moreover, molecular cloud interacting with the SNR is also observed (Jiang et al., 2010). γ-ray emission observed from the secondary source might be originated from this interaction.

5.1.2 Implications

As one of the strongest γ-ray pulsar candidate, the identification of 2FGL J1906.5+0720 remained elusive until now, despite several years of attempts. Now identified as PSR J1906+0722, here we discuss the potential reasons for the failure of previous searches.

The biggest obstacle in the detection of PSR J1906+0722 was likely to be the large positional offset between its 3FGL catalog position and its actual position. This offset is due to the presence of the secondary source described in Section 5.1.1, reduced the pulsation significance. The detection could not be made without the huge sky position coverage in our search.

The low galactic latitude of PSR J1906+0722 (b = 0.03°) could also hindered its detection, as the large majority of the weighted photons can be coming from the Galactic γ-ray background. This result in a very low pulsed fraction as low as 6%, as shown in Figure 5.6, making its detection more challenging.

A further factor hinder the detection of PSR J1906+0722 was the glitch occurred about the one year after the start of the *Fermi* mission. This glitch is one of the largest detected from a γ-ray pulsar in terms of relative magnitude. Previous searches in γ-ray was severely affected by the glitch becasue of the shorter data span. As *Fermi* mission continues, the length of the dataset increases, as the pulsar's signal has become stable after the glitch, the effect of the glitch will be reduce in our semi-coherent search. Also the increase in the sensitivity by the Pass 8 analysis (Atwood et al., 2013) further increases the S/N throughout the mission, increases the chance of detecting weaker pulsars and pulsars with glitches.

The ability to detect young γ-ray pulsars in blind searches is important to the overall study of energetic pulsars. Since pulsars with a high $\dot{E}$ tend to exhibit timing noise and glitches (which does not affected radio searches due to the short integration time), they are harder to find in γ-ray data, where long integration times are required. Powerful search methods that can detect distorted signals such as that from PSR J1906+0722 are needed to reduce a potential bias against young, energetic and glitching pulsars in the radio-quiet regime, which are still lacking in the *Fermi*-LAT pulsar sample (Abdo

et al., 2013; Caraveo, 2014).

5.2 A Radio Quiet γ-ray pulsar with a measurable Braking Index – PSR J1208−6238

5.2.1 Pulsar properties

As in the case of PSR J1906+6722, a visual inspection of a candidate signal from 3FGL J1208.4−6239 result in the identification of this source as the pulsar now know as PSR J1208−6238. A second frequency derivative of 3.3×10^{-22} Hz s^{-2} was measured from the preliminary timing analysis. Timing analysis using the extended dataset revealed that a single braking index could not fit the whole dataset well. Instead, we find that we need increments in the pulsar spin-down rate in order to account for PSR J1208−6238's temporal behaviour. The timing residuals are shown in Figure 5.5 with different assumptions of the braking index. Post-glitch relaxation might be the cause of the changing braking index in the middle of the dataset, which means PSR J1208−6238 may have glitched before the start of the *Fermi* observations.

Significant emission above the background was observed from the integrated pulse profile from the initial timing solution (Figure 5.6), which indicates the presence of nearby unmodeled sources. To investigate the origin of the unpulsed flux, I performed a spectral analysis of the off-pulse emission (see Section 4.4.1). This revealed a number of unmodelled γ-ray sources, the closest one lies $20'$ from the pulsar's timing position. The spectral index of this nearby source is $\Gamma = 2.56 \pm 0.09$ and accounted for $(40 \pm 13)\%$ of the energy flux of PSR J1208−6238. After including these additional sources in our model, I re-fit the model and re-calculate the photon weights for PSR J1208−6238, with the new photon weights for PSR J1208−6238 the pulsation significance increased. The pulsar's spectral properties after the subtraction of the putative sources are given in Table 5.2.

Follow-up radio observations targeted at the pulsar position were conducted with the 64-m Parkes radio telescope for 2.5 hr and 4.3 hr at 1.4 GHz. No plausible pulsar candidates were found using the γ-ray ephemeris down to a mean radio flux density of ≈ 17 μJy.

5.2.2 Implications

PSR J1208−6238 is the youngest known radio-quiet γ-ray pulsar ever discovered, with the estimated age of the pulsar is around 2,700 yr. Also it is the first radio-quiet γ-ray pulsar with a reliable braking index measurement, and one of only ten pulsars with such measurement. The observed braking index, $n = 2.598 \pm 0.01$, is below the $n = 3$ predicted by a simple dipole braking model. The lower braking index could be due to a slowly growing magnetic field in the neutron since its birth over a long time scale ($\sim 10^5$ yr) to a steady state. The total spin-down power can also be dissipated through different physical processes with different braking indices as discussed in Section 1.2.4.

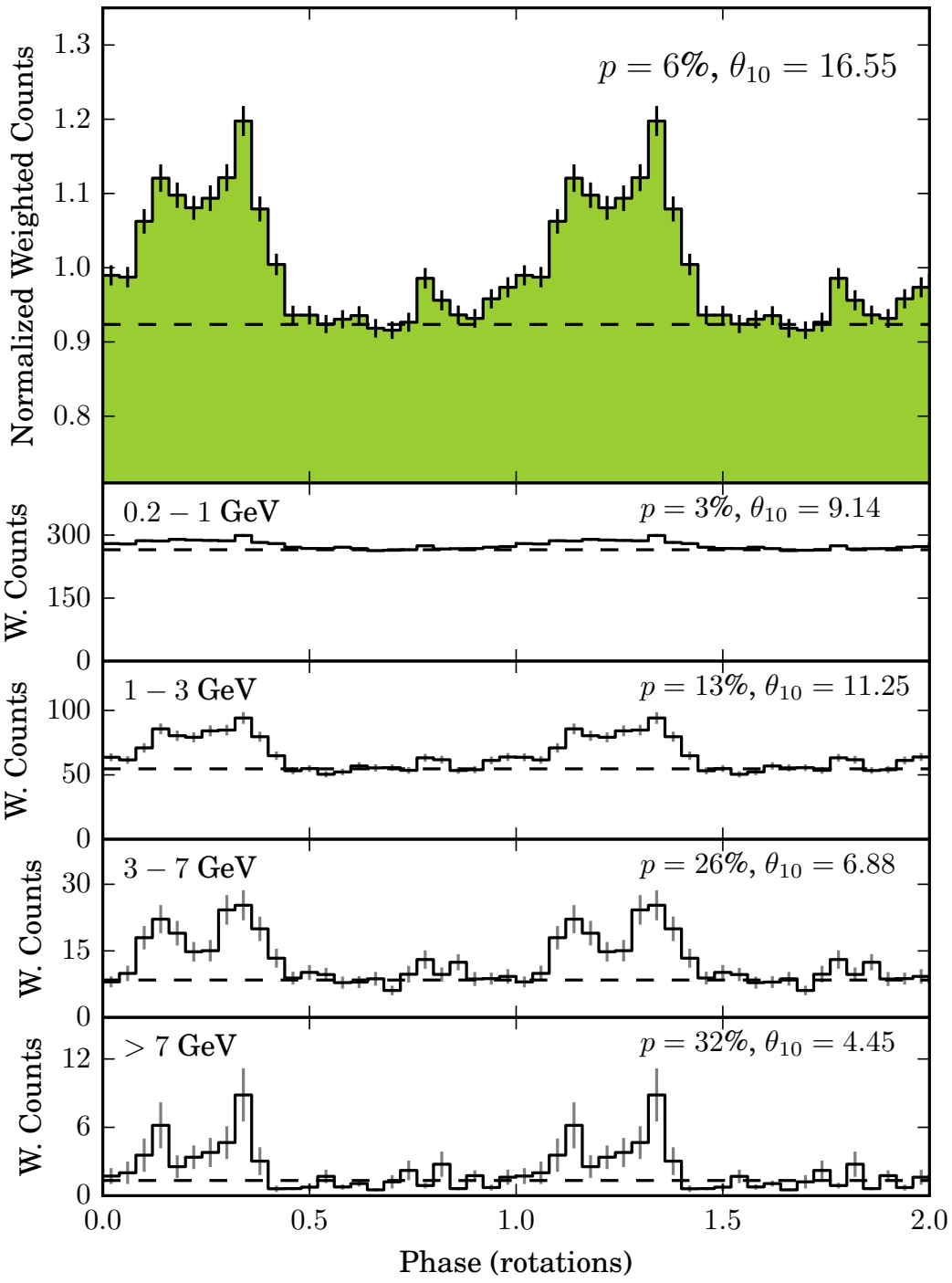

Figure 5.3 Top panel: weighted pulse profile of PSR J1906+0722 given by the timing solution shown in Table 5.1. Lower panels: weighted pulse profiles in different energy band. The estimated background level, calculated from the photon weights (Guillemot et al., 2012b), is shown by the dashed line in each panel. The error bars show 1σ statistical uncertainties (Pletsch et al., 2012b). In each energy band, the pulsed fraction, p, and pulsed S/N, θ_{10}, is also shown. Plot reproduced from Clark et al. (2015).

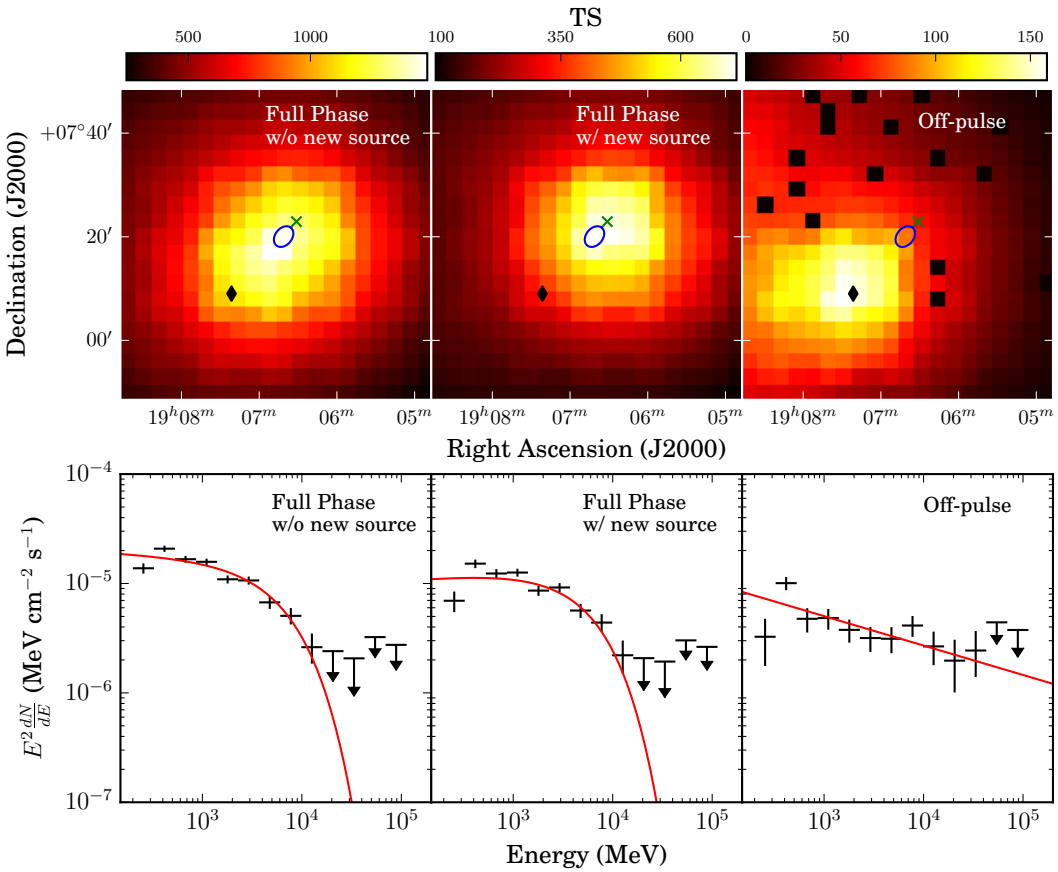

Figure 5.4 Top panels: Test statistic (TS) maps of the PSR J1906+0722 region above 200 MeV in full-phase interval. Each pixel shows the TS value for a point source located at the pixel position. The cross represents the timing position of PSR J1906+0722, the central ellipse shows the 95% confidence region of 3FGL J1906.6+0720, and the diamond represents the putative source position. Bottom panels: Spectral energy distributions for the full-pulse interval. The solid curves present the results of the likelihood analyses. Plot reproduced from Clark et al. (2015).

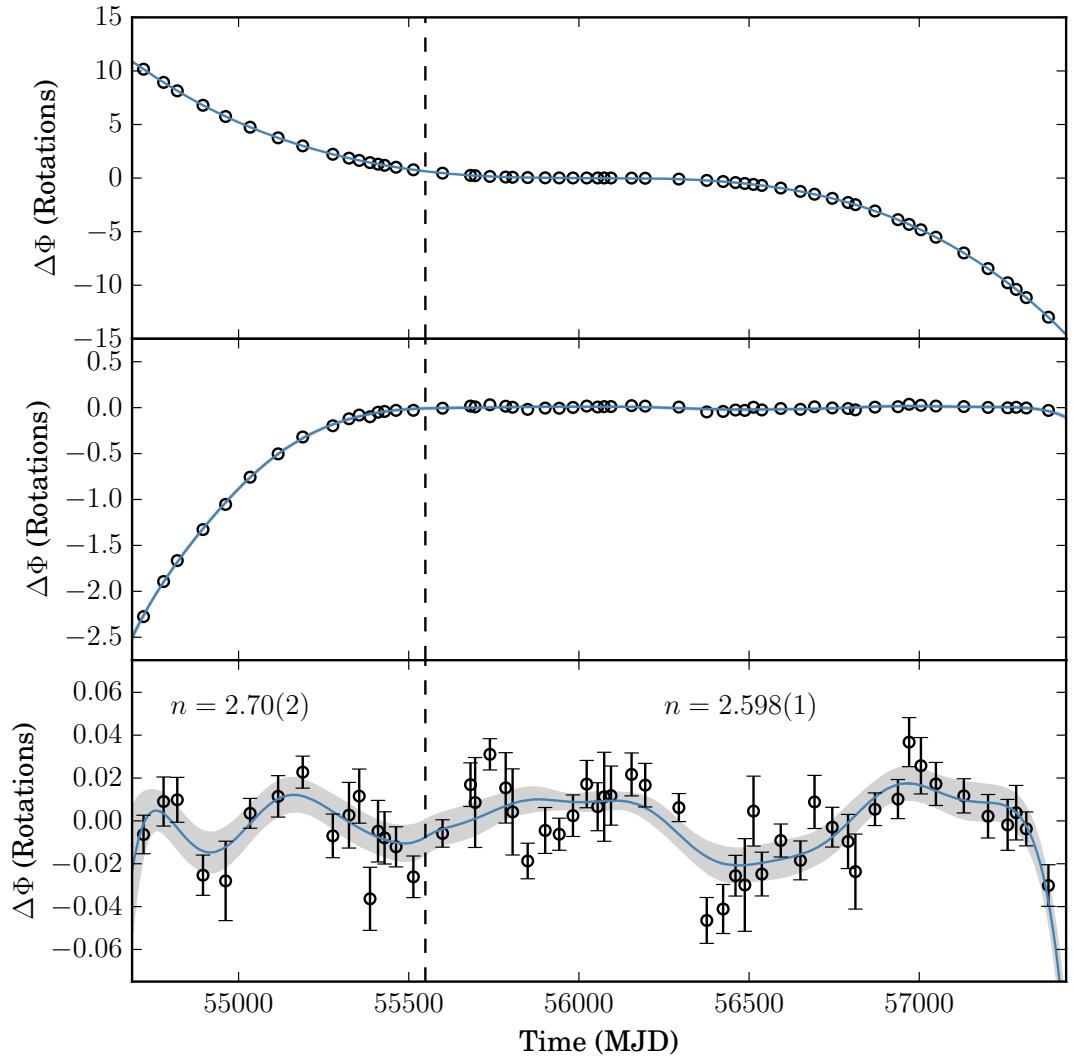

Figure 5.5 Phase residuals for PSR J1208−6238 with different the timing models. The blue lines and grey shaded regions represent the best-fit Taylor series phase model and 1σ uncertainties. Upper panel: phase residuals between the Taylor series and a pure dipole-braking model with $n = 3$. Middle panel: residuals between the Taylor series model and a best-fit constant braking index model with $n = 2.598$. Lower panel: residuals between the Taylor series model and a changing braking index and spin down rate at the dashed vertical line presented in Table 5.2. Plot reproduced from (Clark et al., 2016).

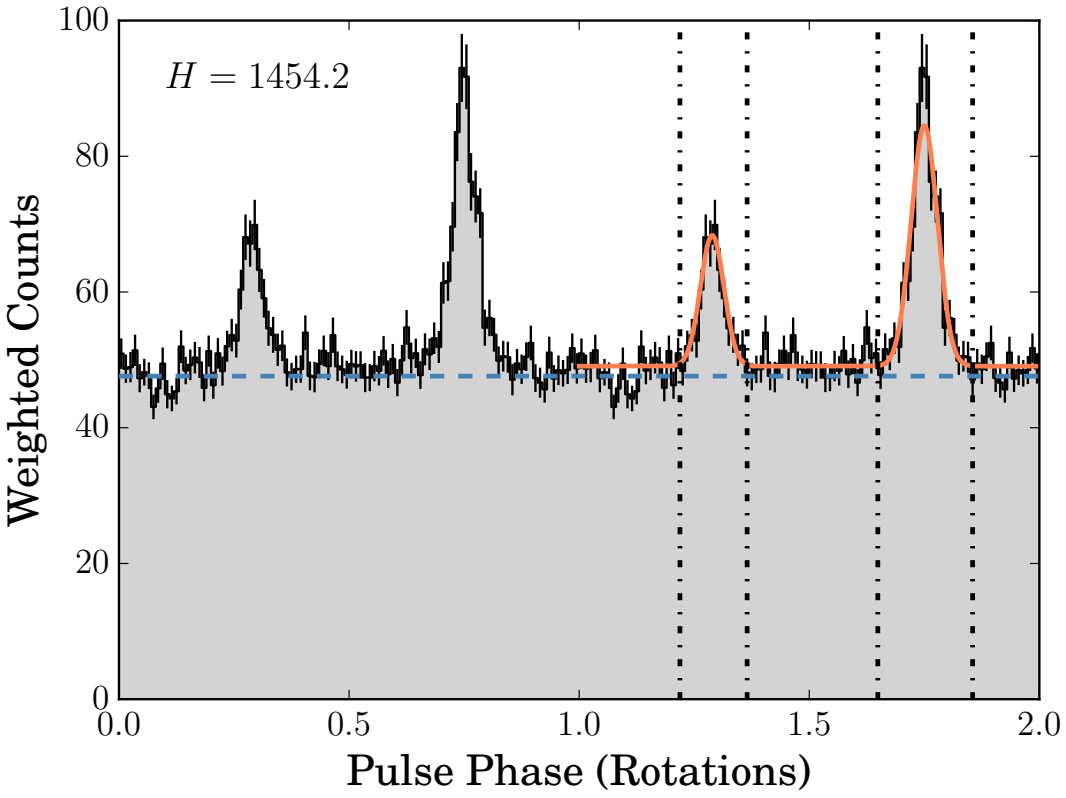

Figure 5.6 γ-ray pulse profile of PSR J1208−6238, weights are calculated with the spectral analysis result described in Section 5.2.1. The solid orange curve shows the template pulse profile used in the timing analysis. The dashed blue line shows the background level estimated from the photon weights (Abdo et al., 2013). Vertical dashed-dotted lines represent the phase ranges excluded from the off-pulsar analysis. Plot reproduced from (Clark et al., 2016).

Table 5.2 Parameters for PSR J1208−6238

Parameter	Value
Range of Photon Data (MJD)	$54682 - 57434$
Reference epoch (MJD), $t_{\rm ref}$,	56040
Timing Parameters[a]	
Right Ascension, α (J2000.0)	$12^{\rm h}\,08^{\rm m}\,13^{\rm s}.96(6)$
Declination, δ (J2000.0)	$-62°38'02''.3(4)$
Frequency, f (Hz)	2.26968010518(7)
1st frequency derivative, $\dot{f}$, (Hz s^{-1})	$-16.842733(5) \times 10^{-12}$
Braking index, n,	2.598(1)
$\dot{f}$-increment epoch (MJD)	55548(23)
$\dot{f}$-increment, $\Delta\dot{f}$ (10^{-15} Hz s^{-1})	0.59(9)
n-increment, Δn	−0.10(2)
Derived Properties[b]	
Galactic longitude, $l(°)$	297.99
Galactic latitude, $b(°)$	−0.18
Spin period, P (ms)	440.59072365(1)
Period derivative, $\dot{P}$ ($\times 10^{-12}$s s^{-1})	3.2695145(9)
Surface B-field, $B_{\rm S}$ (10^{12}G)	38.4
Estimated age[c], $\tau_{\rm c}$ (yr)	2672
Spin-down power, $\dot{E}$ (10^{36}erg s^{-1})	1.5
Surface B-field strength, $B_{\rm S}$ (G)	2.02×10^{12}
Heuristic distance, $d_{\rm h}$ (kpc)	3.0
Spectral Properties[d]	
Spectral index, Γ	$1.73 \pm 0.08 \pm 0.04$
Cutoff energy, $E_{\rm c}$ (GeV)	$4.86 \pm 0.59 \pm 0.70$
Photon flux, F_{100} (photons cm^{-2} s^{-1})	$(4.41 \pm 0.86 \pm 0.37) \times 10^{-8}$
Energy flux, G_{100} (erg cm^{-2} s^{-1})	$(3.49 \pm 0.44 \pm 0.29) \times 10^{-11}$

Note. − The reported values for f and $\dot{f}$ at the reference time include the effect of the earlier $\dot{f}$ increment.

[a] For timing parameters, we report mean values and 1σ uncertainties on the final digits in brackets from the results of the timing analysis described in Clark et al. (2016).

[b] Derived properties are calculated as described in Abdo et al. (2013). Heuristic distances are calculated as descibed in Section 4.4.4.

[c] The estimated age was calculated using the measured braking index.

[d] The first reported uncertainties are statistical, while the second uncertainties are systematic, determined by re-analyzing the data with bracketing IRFs and artificially changing the normalization of the Galactic diffuse model by ±6%, as described in Acero et al. (2016b).

5.3 Millisecond Pulsars found in blind search

In the γ-ray pulsar population, almost half of the young pulsars (56/113) are radio-quiet, but so far no radio-quiet MSP had been found. This can be explained by combination of the extreme computational challenge to detect such high spin frequency signals in γ-rays, not to mention the extra dimensions need to be searched for pulsars in binary systems. Also the wider radio beams of MSPs makes them more likely to be detected in the radio. So far, only one γ-ray MSP (PSR J1311−3430) had been found in previous semi-blind γ-ray searches (Pletsch et al., 2012a), with the help of additional positional and orbital constraints from optical and X-ray observations. Extensive radio follow-up observations of PSR J1311−3430 using multiple telescopes at multiple frequencies eventually revealed its radio pulsations (Ray et al., 2013), suggesting that radio-quiet MSPs are rare.

Therefore, finding radio-quiet MSPs in γ-rays is one of the primary goals of our survey in order to explore the unknown regime of the radio-quiet MSP population. In order to search for potential MSPs in the LAT data, we searched for spin frequencies up to 1520 Hz, which is more than twice the spin frequency of the fastest known MSP (716 Hz). The reason to search up to two times the spin frequency is because most of the power will go to the second harmonic if the pulse profile contains two similar peaks separated with half a rotation.

Among the 118 3FGL sources searched in our Einstein@Home γ-ray blind search survey, millisecond γ-ray pulsations from 3FGL J1035.7−6720 and 3FGL J1744.1−7619 were detected with very high significance. Their pulsar-like spectra and high Galactic latitudes had made them promising MSP candidates, as reported in Hui et al. (2015) and Saz Parkinson et al. (2016). They are also listed in the top 50 pulsar-like unassociated LAT sources in our search list (Table 4.9). Prior to our survey, 3FGL J1035.7−6720 and 3FGL J1744.1−7619 were searched 9 and 10 times respectively in radio with the Parkes radio telescope (Camilo et al., 2015) and in the previous Einstein@Home γ-ray blind search survey (Pletsch et al., 2013), but no pulsations were ever detected from these sources. The previous non-detections are due to the extremely low radio fluxes and shorter time span and lag window used in the γ-ray blind search. In the following sections, the characteristic of the two solitary γ-ray MSPs will be summarized and the implications of detecting radio-quiet MSP will be discussed.

5.3.1 Pulsars properties

Follow-up analyses for the two pulsars were performed using an extended dataset covering up to 16 March 2017 ($\sim$ 8.5 years of LAT data), we refined the spacial and temporal parameters for both pulsars with an unbinned timing analysis, shown in Table 5.3. The pulse profiles folded with the corresponding timing solution in Table 5.3 are shown in Figure 5.7.

I performed binned likelihood spectral analyses for photons from the full phase interval using *gtlike*, following the procedure described in Section 4.4.1. The resulting phase-averaged spectral parameters for each pulsar are given in Table 5.3. The phase-

averaged γ-ray spectral properties (Γ & E_{cut}) of both pulsars are similar to those of the MSP population seen in 2PC.

From the integrated pulse profile for PSR J1744−7619, significant γ-ray emission above the estimated background level was observed (Figure 5.7). We performed off-pulse spectral analysis for both pulsars to determine whether this is from the unpulsed magnetospheric emission, or contamination from nearby source(s).

I defined off-pulse regions for the two pulsars using the Bayesian Block decomposition method described in Section 4.4.1, the definitions of the off-pulse regions can be found in Table 5.3. Following the same procedure as Sections 4.4.1, no significant off-pulse emission was detected from PSR J1035−6720. Although the non-detection could due to the low photon statistics as only $\sim 14\%$ of the total spin phase was selected for PSR J1035−6720 in the analysis. Off-pulse emission at the PSR J1744−7619 position was detected at 5.8σ with a 2.9σ spectral cutoff, suggesting a likely magnetospheric origin of the off-pulse emission (Abdo et al., 2013).

In a recent radio pulsar survey targeting 56 unassociated *Fermi*-LAT sources with the Parkes radio telescope (Camilo et al., 2015), PSR J1035−6720 and PSR J1744−7619 were observed multiple times between 2009 and 2012, at a center frequency of 1390 MHz. Typical integration times were around 1 hr, ranged between 41 and 136 minutes for these two sources. They were searched 9 and 10 times respectively but no pulsations were detected. After the discovery, deeper radio follow-up observations, exposure time ranging from 164 – 232 minutes, from the Parkes radio telescope were able to detect the weak signals ($S_{1400} \approx 40$ μJy) from PSR J1035−6720 with a DM of 84.16 ± 0.22 pc cm^{-3}, corresponding to $d \approx 1.46$ kpc or $d \approx 2.24$ kpc estimated from Yao et al. (2017) and Cordes & Lazio (2002) Galactic electron-density models. However, PSR J1744−7619 still remains undetected in two dedicated three-hour follow-up searches, giving an upper limit in radio density of ~ 23 μJy.

Weak or no radio pulsations from the pulsar are expected if the radio beam is clipping or does not cross our line-of-sight at all, this is the case for PSRs J1035−6720 and J1744−7619. To understand the γ-ray emission geometries of these two pulsars, we used the fitting technique and models from Johnson et al. (2014) and considered three different models: an outer gap (OG), a two-pole caustic (TPC) model and a pair-starved polar cap (PSPC) model. The fitting results are shown in Figure 5.7. For PSR J1035−6720, only the PSPC model was able to predict the radio pulsation we detected, with the compatible phase lag with the observation. However the phase uncertainty of the radio pulse contributed by DM, up to 15% of the pulse period, prevents a joint fit of the radio and γ-ray data. Note that none of the models were able to reproduce the double peaks pulse profile observed from PSR J1035−6720. For PSR J1744−7619, both TPC and PSPC have our line-of-sight cutting through the modelled radio emission cone, giving rise to different radio pulse profiles. Since no radio pulsations were detected from PSR J1744−7619 we cannot differentiate which model fit better. The fact that PSR J1744−7619 is not detected in radio is either due to an extremely low radio luminosity, lower than 90% of the radio MSP population, or the current emission models are not adequate to explain the non-detection in radio.

5.3.2 Implications

It has been shown that MSPs have wide radio beams (Kramer et al., 1998; Manchester, 2005; Story et al., 2007; Ravi et al., 2010) that are detectable over a wide range of possible viewing geometries, implying very few radio-quiet MSPs. However, the absence of radio-quiet MSPs in the current pulsar population could be due to a selection bias as MSPs are much more difficult to find in a γ-ray blind search. PSR J1744−7619 is the perfect example of the hidden radio-quiet MSP population where γ-ray blind searches is the only way to gain access to them, as their radio emissions may be too weak to be detected or missing our line-of-sight. Also, the discovery of PSR J1035−6720 can shed some light on the biased radio MSP luminosity distribution, where MSPs with such low radio fluxes are clearly missing from the current radio MSP population (Lorimer, 2008). The discovery of PSR J1744−7619 and further radio-quiet MSP discoveries in the future will provide a less bias radio-quiet to radio-quiet MSP ratio in the γ-ray MSP population. This ratio can provide a constrain on the ratio of the radio and γ-ray emission beaming angles, which is an important factor for discriminating different pulsar emission models (Takata et al., 2011).

Given the high binary/isolated radio-loud γ-ray MSP ratio, the discovery of two isolated MSPs in our survey implies that there could be a good number of radio-quiet MSP in binary systems yet to be discovered. Orbital constraints from studies of 3FGL sources' X-ray or optical counterparts are needed to reduce the multidimensional parameter space in the search of binary MSPs in γ-ray. A number of 3FGL sources have already been identified as binary MSPs from their behaviour in other wavelengths, for example: 3FGL J0212.1+5320 (Li et al., 2016), 3FGL J0744.1−2523 (Salvetti et al., 2017) and 3FGL J2039.6−5618 (Salvetti et al., 2015). Sensitive blind searches using constraints from optical/X-ray may reveal their pulsations in the future.

There are a number of curved spectra LAT sources at high Galactic latitude which are still unassoicated. Besides pulsars, the spectra of these sources are also consistent with dark matter annihilation in ultra-faint dwarf spheroidal galaxies or dark matter subhalos (Ackermann et al., 2015; Charles et al., 2016). Blind searches targeting these sources maybe able to identify pulsating signal from MSPs Although these sources are more likely to be binary MSPs, finding any isolated MSPs in these unassoicated LAT sources could still rule out some of the sources from dark matter candidates.

5.4 Summary

In this chapter, I presented the timing and spectral analysis results of four of the pulsars from the Einstein@Home γ-ray blind search survey. Pulsars presented in this chapter are the perfect examples of how pulsars found in blind periodicity searches in γ-rays can reduce the detection bias against γ-ray pulsars in the Galactic pulsar population. It also pushes the boundary of our understanding of the pulsar emission mechanism. Despite the positional offset caused by the hidden serendipitous source and the giant glitch happened in August 2009, we were still able to recover signals from PSR J1906+0722 thanks to the photon weighting technique and the semi-coherent

multi-stage search algorithm. The ability to detect more pulsars that suffered from glitches like PSR J1906+0722 will reduce the detection bias against young, energetic and glitching radio-quiet γ-ray pulsars.

The study of braking indices is only possible for the youngest or highly magnetized pulsars, where their $\ddot{\nu}$ are large enough to dominate the timing noise. Prior to the discovery of PSR J1208−6238, only nine pulsars detected in radio/X-ray offered such reliable measurements. The discovery of PSR J1208−6238 opens a new window for braking index studies using radio-quiet γ-ray pulsars. More young, energetic and highly magnetized γ-ray pulsars discovered from LAT data will advance spin-down mechanism studies through radio-quiet γ-ray pulsars.

Lastly, the discovery of two isolated MSPs PSRs J1035−6720 and J1744−7619 has at last revealed the long speculated radio-quiet γ-ray MSP population. Once again this demonstrated the power of the search algorithm running on Einstein@Home which overcomes the computational challenge in order to pick up such high frequency signals. PSR J1744−7619 is the first radio-quiet MSP in the pulsar population, showing a hidden population is yet to be revealed from γ-ray blind searches. This allows us to eliminate the detection bias against the radio-quiet γ-ray MSP population. Through pulse profile analysis, we found that only the PSPC model could predict the detection of radio pulsations from PSR J1035−6720. However, none of the emission models can reproduce the broad double-peaked pulse profile from PSR J1035−6720. For PSR J1744−7619, two of the best-fitting models (TPC and PSPC) predicted radio emission, which is in contradiction to the ~ 23 μJy flux upper limit determined from our deep radio follow-up observations. Therefore, these two MSPs challenge the current emission models and demand the development of more advanced pulsar emission models.

Table 5.3 Parameters for PSRs J1035−6720 & J1744−7619

Parameter	PSR J1035−6720	PSR J1744−7619
Timing Parameters[a]		
Reference Epoch (MJD)	55716	
Data span (MJD)	54682 - 57828	
Right Ascension, α (J2000)	10:35:27.478(1)	17:44:00:488(2)
Declination, δ (J2000)	-67:20:12:692(6)	-76:19:14:710(9)
Proper Motion in α, μ_α (mas yr^{-1})	-12(3)	-21(3)
Proper Motion in δ, μ_δ (mas yr^{-1})	1(3)	-7(3)
Spin Frequency, f (s^{-1})	348.18864014054(8)	213.33223675351(5)
Spin-down rate, $\dot{f}$ (10^{-15}Hz s^{-2})	5.633(1)	0.4405(8)
Second frequency derivative, $\ddot{f}$ (10^{-25}Hz s^{-3})	< 1.1	< 0.7
Spin period, P (ms)	2.8720063916972(7)	4.687524094895(1)
Period derivative, $\dot{P}(10^{-20}ss^{-1})$	4.647(1)	0.968(2)
Derived Parameters[b]		
Galactic longitude, l (deg)	290.37	317.11
Galactic latitude, b (deg)	-7.84	-22.46
Spin-down power, $\dot{E}$ (10^{33} erg s^{-1})	75.0	< 3.7
Characteristic age, $\tau_c(10^9)$	1.0	7.7
Surface magnetic field, B_s (10^8)	3.7	2.2
Light-cylinder magnetic field, $B_{LC}(10^5)$	1.4	0.2
Phase-averaged γ-ray spectral parameters above 100 MeV[c]		
Test statistic, TS	1839.2	2492.2
Photon index, Γ	1.46 $\pm$ 0.07$\pm$ 0.09	1.07 $\pm$ 0.10 $\pm$ 0.02
Cutoff energy, E_c (GeV)	2.76 $\pm$ 0.26 $\pm$ 0.36	1.82 $\pm$ 0.19 $\pm$ 0.01
Photon flux, F (10^{-9} cm^{-2} s^{-1})	24.4 $\pm$ 1.7 $\pm$ 1.5	19.2 $\pm$ 1.5 $\pm$ 1.0
Energy flux, G (10^{-12} cm^{-2} s^{-1})	21.5 $\pm$ 0.8 $\pm$ 1.1	20.8 $\pm$ 0.8 $\pm$ 1.1
Off-pulsar spectral parameters above 100 MeV		
Phase range	0.13 - 0.27	0.06 - 0.31
Test statistic, TS	7.4	33.8
TS of exponential cutoff, TS$_{cut}$	-	8.3
Photon index, Γ	-	1.35 $\pm$ 0.70 $\pm$ 0.09
Cutoff energy, E_c (GeV)	-	1.06 $\pm$ 0.76 $\pm$ 0.13
Photon flux, F (10^{-9} cm^{-2} s^{-1})	-	1.9 $\pm$ 0.9 $\pm$ 0.1
Energy flux, G (10^{-12} cm^{-2} s^{-1})	-	1.2 $\pm$ 0.3 $\pm$ 0.1

[a] For timing parameters, we report mean values and 1σ uncertainties on the final digits in brackets from the results of the timing analysis described in Clark et al. (2017).

[b] Derived properties are calculated as described in Abdo et al. (2013). Heuristic distances are calculated as descibed in Section 4.4.4.

[c] The first uncertainty is statistical, the second estimates systematic uncertainties in the LAT's effective area, estimated by performing the same spectral analysis with rescaled effective areas.

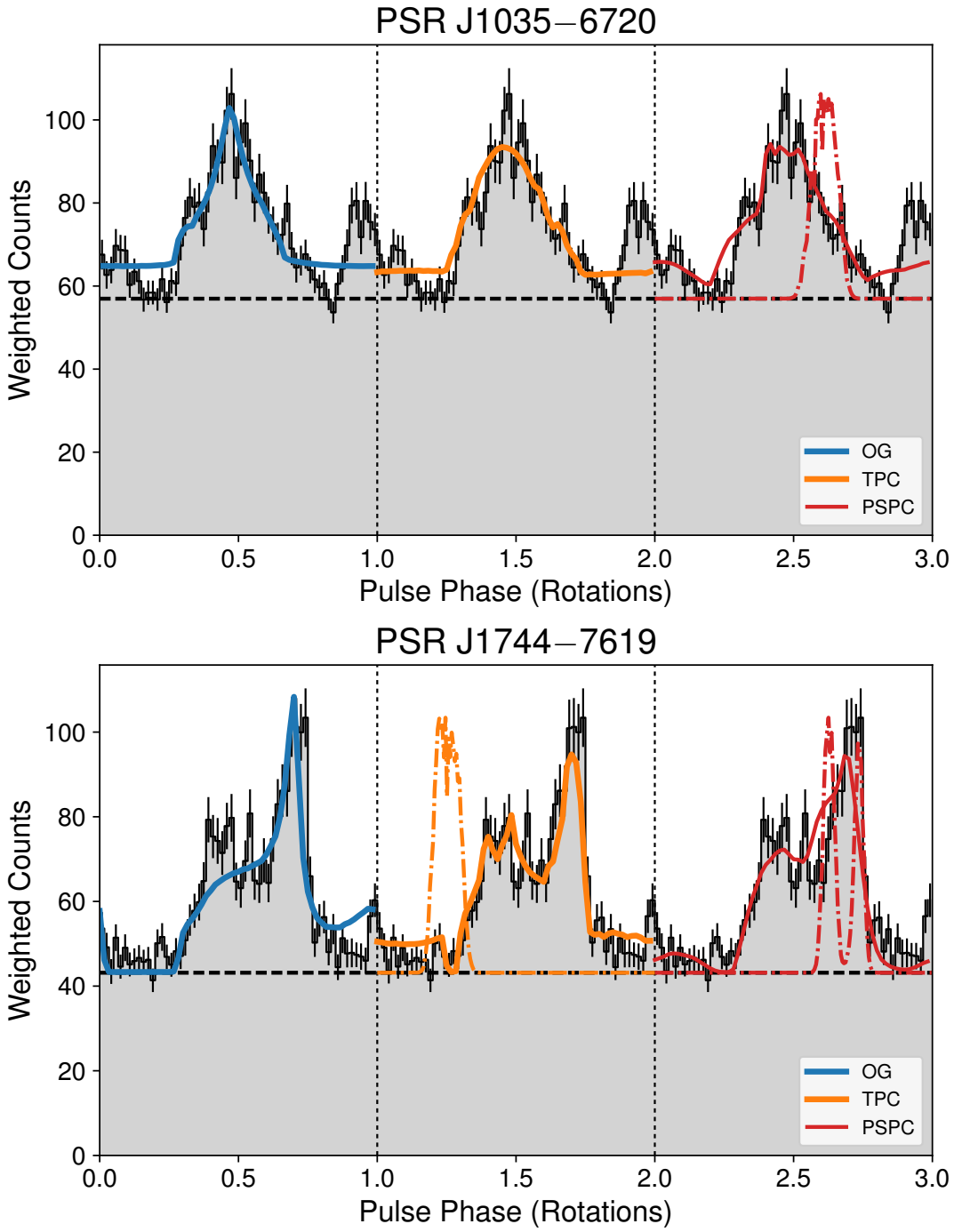

Figure 5.7 γ-ray pulse profiles of the newly detected MSPs. The overlaying solid curves and the dash-dotted curves are the best-fitting pulse γ-ray and radio profiles predicted by fits to outer-gap (OG), two-pole caustic (TPC) and pair-starved polar cap (PSPC) γ-ray emission models. The dashed black line is the estimated background level, derived from the photon weights as in Abdo et al. (2013). Plot reproduced from Clark et al. 2017, Science Advance, submitted.

Chapter 6

A Radio Pulsar Survey at Effelsberg using the Ultra Broad-Band (UBB) Receiver

Using the 100-m Effelsberg radio telescope with the state-of-the-art Ultra Broad Band (UBB) receiver operating between 0.6 - 1.4 GHz, we explored the possibility of using the UBB for a targeted pulsar survey by observing 54 unassociated *Fermi*-LAT sources from the 3FGL catalogue (Acero et al., 2015). The observed sources are known to contain 4 newly discovered Einstein@Home γ-ray pulsars (Chapters 4 and 5) which were undetected in our radio survey. We put limits on the radio flux densities for those pulsars and all the observed sources and discuss the details and possible improvement of the survey. The results presented here will be published in an upcoming publication (Wu & Torne et al. in prep.).

Contents

6.1 Introduction

There are 93 MSPs now known to be pulsating in γ-rays. Apart from those discovered through folding known radio pulsar ephemerides, 54 of them were discovered from targeted radio searches on unassociated LAT sources. From those 54 sources, 48 of them (88%) are in binary systems. Targeted radio searches of *Fermi* sources is proven to be very effective in fining candidate of MSPs which offers an alternative way to complete the pulsar population. Radio-dim MSPs and MSPs in binary systems are very hard to discover in conventional radio all-sky surveys or blind periodicity searches in γ-ray. Large collecting area, wide frequency coverage, fine frequency resolution and

high time sampling rate are necessary to reveal these faint pulsar signals from these systems. The aforementioned requirements are achievable only with the most advanced receivers, computers and processing algorithms available.

The majority of pulsar discoveries in unassociated *Fermi*-LAT sources were made at low radio frequencies (350 – 800 Mhz) because pulsars tend to have steep spectral indices (see Hessels et al., 2011; Ray et al., 2013; Bates et al., 2013). The new Ultra-Broad-Band (UBB) receiver developed at the MPIfR for the Effelsberg 100-m radio telescope has technical characteristics that fit excellently with the requirements for such a survey, significantly increasing the discovery probabilities over other similar surveys.

6.2 The Ultra Board Band receiver

The UBB is one of the first ultra wide bandwidth receivers developed in radio astronomy, it started in 2011 by MPIfR with the support of the European Research Council under the grant BEACON (P.I.: Paulo Freire). The UBB was originally designed to operate in the frequency range of 0.6 - 3 GHz, this allows us to observe at the previously successful low radio frequencies pulsar searches in unassociated LAT sources. Moreover, the larger instantaneous bandwidth of the UBB compared to other receivers means, apart from an increase in sensitivity, has an advantage in overcoming scintillation effects, which have been one of the reasons for unsuccessful surveys in the past. The large bandwidth will also increase the chance of finding a frequency band where the pulsar happens to be strong. The UBB feed is under-illuminating the dish, which means that not the full collecting area of the telescope is used, this turns out to be favourable for pulsar surveys. The under-illumination results in a bigger primary beam of the telescope, which allows the full coverage of the positional error ellipse of the selected candidates, thus minimizing the chances of missing the source. The under illumination of the dish also means a decrease in sensitivity, but the large bandwidth of the UBB counteracts this effect. In our survey, we covered from the lowest possible frequency, 600 MHz, up to what the current backend limitations allow, about 1.5 GHz, with 500 MHz non-contiguous bandwidth in total, see Figure 3.2 of an example of the observing band from one of the test pulsar PSR J0332+5435.

6.3 Observations and Analysis

All search data presented in this chapter were taken with the 100-m Effelsberg radio telescope between frequencies of 0.6 – 1.4 GHz during 17 – 18 November 2013 and 07 – 09 April 2014, using the new Effelsberg UBB receiver at the primary focus with 500-MHz effective bandwidth.

We have selected a list of unassociated LAT sources from the preliminary 3FGL catalog based on their γ-ray spectral shape and time variability. We selected sources with declinations north of -30° to fit with the elevation limitation of Effelsberg and positional error circles with diameters smaller than the $14'$ beam-width of UBB at 1400

MHz. Due to observational constraints, i.e. the tension between time allocation and the sky positions of the selected candidates, we could not observe all of the strongest pulsar candidates within the two observing sessions. Instead, we maximized the number of candidates observed in these two observing sessions by covering as many high priority sources as possible with lower priority candidates filling in between. Note that the application of GMM (Section 2.3) on the 3FGL catalog was done only after this survey, i.e. GMM was not used for selecting 3FGL candidates for this survey. Within the two observing sessions, 54 3FGL sources were observed in the two observing sessions. All sources were observed with 10- or 30-minute integrations. These short integrations allowed for the detection of tight binaries and are also favourable for sources harbouring brightest pulsars, those likely to have been of the greatest use for timing applications. The list of the sources observed during the two observing campaigns are listed in Table 6.2.

Data were recorded over 3000 filterbank channels, with a channel width of 244 kHz and a sampling rate of 65.5 μs. Initially, all data were sampled at 32 bits by the digitizers then brought down to 8 bits and written to the storage system. Then, the filterbank was split into three parts, with the frequency centred at 646.75, 875.47 and 1334.73 MHz with bandwidth of 46.50, 31.25 and 250.0 MHz respectively.

In order to meet the processing demands of the huge amount of data, I used the *Hercules* computing cluster located at the Max Planck Computing and Data Facility at Garching for most of the data analysis. The PRESTO software package (Ransom, 2011) was used for the data processing. In the first phase of the processing pipeline, the data was treated with a RFI removal technique where a time and frequency dependent mask was created for use in later stages. Since the 3FGL catalog does not contain distance information, data in each frequency band were de-dispersed by the trial dispersion measure (DM) within the range 0 – 1000 pc cm^{-3} with 4062, 1600 and 1938 DM steps respectively. The trial DMs mitigate the frequency dependent delay of the pulsar signal due to dispersion by free electrons along the line of sight. The choice of such fine sampling in the DM space makes it possible to preserve the maximum time resolution of the data at all DMs in each frequency band. The effect of this is an increased sensitivity to milliseconds and potential sub-millisecond pulsars.

All de-dispersed time series were fast Fourier transformed (FFT), the power spectrum obtained was de-reddened and the known RFI frequencies were removed. In order to reconstruct the power distributed in different harmonics in the power spectrum, incoherent harmonic summation was used. The original spectrum is summed with its own version stretched twice so that all the second harmonics are added to the corresponding fundamental. This process was repeated four times so that all the power distributed in even harmonics up to the 16th harmonic was incoherently added to the fundamental (see Section 3.1.4). Spectra from each stage of the summing process were searched for accelerated and non-accelerated signals.

At this stage, the number and size of the FFT needed to reach the sensitivity to fast binaries becomes too computational expensive for long observation. The search pipeline was divided into two stages to deal with this problem. Initially, all data were analyzed over the full length with a medium acceleration of the search in the Fourier

Table 6.1 The three observing bands of the UBB receiver.

Frequency (MHz)	Central frequency (MHz)	Bandwidth (MHz)	$S_{\nu,10}{}^a$ (mJy)	$S_{\nu,30}{}^b$ (mJy)
600	646.75	46.5	0.37	0.21
800	875.45	31.3	0.45	0.26
1400	1334.73	250.0	0.16	0.09

[a] Flux density limit for 10 minutes observation.
[b] Flux density limit for 30 minutes observation.

domain. This analysis is very sensitive to isolated and slightly accelerated pulsars. The second stage of processing involves dividing the data into 10-minute blocks, and re-analyzing with much higher acceleration ($z_{\rm max} = 1200$). Although this phase uses shorter integration, it is more sensitive to highly accelerated binaries. (see Section 3.1.4 for details of acceleration search). All candidate signals have passed through a sifting routine that removes all signals likely to be RFI. Finally, a set of diagnostic plots for visual examination was created for the 50 best candidates per pointing.

6.4 Sensitivity

To evaluate the sensitivity of our survey set-up we used the radiometer equation (Lorimer & Kramer, 2005),

$$S_{\rm min} = \beta \frac{S/N_{\rm min} T_{\rm sys}}{G\sqrt{n_{\rm p} t_{\rm int} \Delta F}} \sqrt{\frac{W}{P-W}}, \tag{6.1}$$

where the constant factor β denotes signal degradation due to digitisation, which for 8-bit digitisation is $\sim 1\%$, giving $\beta = 1.01$ (Kouwenhoven & Voûte, 2001). $T_{\rm sys}$ is the system temperature of the receiver. From flux density calibration measurements we found $T_{\rm sys} = 50$ K. The high $T_{\rm sys}$ is thought to be due to the strong RFI within the UBB band at Effelsberg, which had increased the $T_{\rm sys}$ of the UBB by a factor > 2 from its nominal value. The antenna gain G (1.5 KJy $^{-1}$ at 1.36 GHz), W the pulse duty cycles assumed to be 10%, $t_{\rm int}$ is the length of the observation, Δf is the effective bandwidth of the receiver and $n_{\rm p}$ is the number of polarisations summed, which is 2 in our survey. The factor $S/N_{\rm min}$ is the minimum signal-to-noise ratio with which we can make a detection. Based on false alarm statistics, we chose $S/N_{\rm min} = 8$. I compute the flux density limit with the median effective bandwidth and exposure time in different band, listed in Table 6.1.

6.5 Simulations

In any survey that contains many pointings, the chance of finding a pulsar which is not associated with the LAT source is non-negligible. In order to determine this

probability, simulations of the normal pulsar and MSP populations were made based on the model presented in Lorimer et al. (2006), using the PsrPopPy package[1]. As the population distributions for MSPs and normal pulsars is different, separate simulations were performed for pulsars with rotational periods above and below 40 ms.

To simulate the normal and millisecond pulsar population, the following parameters were chosen as an input:

1. An empirical period distribution taken from the probability density function of the known pulsar population.

2. A log-normal luminosity distribution, with mean and variance in log space of -1.1 and 0.9, respectively (Faucher-Giguère & Kaspi, 2006).

3. A Gaussian distribution of spectral indices, with a mean of -1.6 and variance of 0.5.

4. An exponential distribution for the height above the Galactic plane, with a scale height of 0.33 and 0.5 kpc for normal pulsar and MSP respectively (Lorimer et al., 2006), 0.5 kpc was chosen for MSPs to match the know MSP distribution better.

5. A radial distribution as described in (Lorimer et al., 2006).

6. The NE2001 Galactic free electron density model (Cordes & Lazio, 2002).

The number of simulated pulsars was calculated to match the following surveys: Parkes Multibeam Pulsar Survey (Manchester et al., 2001), Swinburne Intermediate Latitude Pulsar Survey (Edwards et al., 2001) and its expansion (Jacoby et al., 2009), Parkes High Latitude Survey (Burgay et al., 2006).

I compared the observations of each of the 54 pointings of our survey with the simulated pulsar distribution, and checked whether it was possible to detect a pulsar by chance. I simulated 1000 instances of the Galactic pulsar population for both normal and MSPs, then compared with each pointings. For normal pulsar an average detection rate of 0.695 and for MSP an average detection rate of 0.491 were found with 54 pointings. So in our survey we expected to find less than one pulsar by random chance.

6.6 Discussion

No pulsars were discovered in our survey; there are a number of possible reasons. The first reason is related to radio flux of pulsar and sensitivity. Since most of the bright radio pulsars have already been found in the previous surveys, we expect weak radio pulsars to be found in our survey. With the current performance of the UBB receiver, a 10 minutes integration at L-band should be able to detect ∼86% of the known radio pulsar population using data from the ATNF catalog. Four of the new γ-ray pulsar discoveries from Chapters 4 and 5 (PSRs J0002+6218, J1844−0344, J1906+0720 and

[1]https://github.com/samb8s/PsrPopPy

J2017+3627) were also observed with the UBB but none of them were detected. I compared our flux limit with the follow-up observations done in Chapters 4 and 5 and concluded that the non-detection in our UBB survey is consistent with the given sensitivity in our survey's observations. The other possibility is that these pulsars have extremely steep spectral indices. From previously studies, the mean radio spectral indices α (where $S \propto \nu^{\alpha}$) for pulsars are in the range of -1.6 to -1.8: -1.6 ± 0.3 (Lorimer et al., 1995), -1.6 ± 0.2 (MSPs) and -1.7 ± 0.1 (normal pulsars) (Kramer et al., 1998), -1.8 ± 0.2 (Maron et al., 2000). A recent MSP survey done with LOFAR, where two new MSPs were discovered (Bassa et al., 2017; Pleunis et al., 2017), follow-up radio observations revealed that both of them have very steep radio spectral indices $\alpha < -2.8$. The steep spectral indices of these LOFAR pulsars have made them not visible at high frequency (e.g. L-band). It could be the case that a number of the steep spectrum radio pulsars were missed in our survey. Furthermore, strong RFI can reduce our sensitivity to weak signals. In the 54 pointings that have been searched in our survey, almost half of the pointings (21/54) are heavily affected by RFI, they are marked with * in Table 6.2. That means we are much less sensitive in some of the pointings where RFI were strong. Thus it is possible that undiscovered pulsars have radio fluxes higher than our estimated sensitivity limit by still failed to be detected due to presence of strong RFI.

Also the effects of the ISM (i.e. scattering and scintillation) or the intrinsic emission properties of the pulsar are also known to be a factor varying the discovery rate. For example, the intermittent nature found in some radio pulsars are also a known complication where multiple observations are needed to increase the chance of detecting them. The limited time given to our survey means we could not observe a target long enough or multiple times. That means that there is a chance of missing some of the radio pulsars due to the effects of the ISM or the nature of the pulsed emission.

Another possibility is that there might be radio-quiet pulsars in the list of sources that we have searched with the UBB. In out list of targets, 32 of them were never searched in γ-rays for pulsations, some of them could be radio-quiet pulsars. The rest of the sources have already been searched in γ-ray, the reason of non-detection in γ-rays could be the following: they are radio-quiet γ-ray MSPs which are very hard to detect in γ-rays (see Section 5.3); they can be radio-quiet γ-ray binary MSPs, which cannot be found from current γ-ray blind search without additional information; they are canonical γ-ray pulsars with low γ-ray fluxes, which are below the current γ-ray blind search sensitivity; they could be glitching (see Section 5.1); they have large positional uncertainties due to confusion with other γ-ray source (e.g. PSR J1906+0722 from Section 5.1).

In the current γ-ray MSP population, the chance of finding a MSP in a binary system is about four times higher than an isolated MSP because of the evolution history of MSP (recycling process). Therefore in our survey, we are expecting binary systems which are known to be very difficult to find, another possible reason for no discovery. In searching for binary pulsars using *accelsearch*, one fundamental assumption is that the acceleration throughout the observation is constant. Any changes in the acceleration (i.e. the derivative of acceleration, also known as jerk) will decrease the sensitivity of

accelsearch. Many factors could contribute to the jerk: the non-circularity of the orbit; the orbital phase of the pulsar; the length of the orbit; the maximum acceleration of the system. In fact I have searched with very high acceleration, up to 1000 m/s^{-2} in our 10 minutes pointings, this should be able to cover most of the extreme binary systems (see Figure 5 in Ng et al., 2015), but there is still a chance the pulsed signal may be missed by our search pipeline, such as pulsar-black-hole binaries or any highly eccentric systems.

There is always the possibility that some of the targets may not be pulsars. By comparing our pointings with the GMM result presented in Section 2.3, 12 of them are not on the positive R_s list. This does not rule out the possibility that they are pulsars, but this tells us that their γ-ray properties do not resemble a typical γ-ray pulsar. This could mean they are not pulsar or they are weak in γ-ray so their spectral parameters are not well constrained. The low γ-ray brightness hinder the effectiveness of the pulsar candidate classification using γ-ray properties. From some of the recent pulsar discoveries in unassociated *Fermi*-LAT sources, we are discovering radio pulsars with low γ-ray brightness (Camilo et al., 2015; Cromartie et al., 2016).

It is not likely that a single aforementioned factor can explain the non-detections of our survey, rather than a mixture of the above factors.

6.7 Conclusion

Using the information from the 3FGL catalog, we have observed 54 γ-ray sources to explore the possibility of using the UBB receiver for targeted pulsar searching. The observed sample contains four γ-ray pulsars (PSRs J0002+6218, J1844−0344, J1906+0720 and J2017+3627), newly discovered through recent γ-ray blind search survey described in Chapters 4 and 5. Deep follow-up radio observations presented in Chapters 4 and 5 revealed that only one of these four γ-ray pulsars is detectable in radio (PSR J0002+6281). We found no evidence of radio pulsations from PSR J0002+6218 in the UBB data. This is consistent with its radio flux density (22 μJy) determined from Chapter 4, which is below our UBB sensitivity limit. We found that the T_{sys} is two times higher than the nominal value from the laboratory measurement. The high T_{sys} is due to the strong RFI environment at Effelsberg. This reduced our sensitivity by at least a factor two and strongly affected almost half of the pointings. Also the challenges in data processing and the RFI situation are the main obstacles for such survey with wide frequency coverage. In our experience Ultra-Wide-Bandwidth receivers like the UBB need careful RFI mitigation (such as the RFI filters being developed for Effelsberg) is critical to their usage for future pulsar surveys.

Table 6.2: Observed unassociated *Fermi* LAT sources with UBB.

3FGL name	R.A. (J2000)	Decl. (J2000)	L (°)	B (°)	R_{95}[a]	Integration time (s)
J0002.6+6218	00:02:41.88	+62:18:02.16	117.30	−0.04	3.64	600
J0004.2+6757	00:04:13.22	+67:57:33.48	118.51	5.49	6.09	1800
J0039.3+6256*	00:39:20.21	+62:56:29.40	121.56	0.10	3.37	600
J0212.1+5320	02:12:08.90	+53:20:09.60	134.93	−7.65	2.07	600
J0220.1+6202c	02:20:11.54	+62:02:37.68	133.13	0.94	7.13	1800
J0223.6+6204	02:23:37.46	+62:04:51.96	133.50	1.12	2.34	600
J0225.8+6159	02:25:53.33	+61:59:13.20	133.78	1.12	5.69	600
J0238.0+5237	02:38:01.18	+52:37:32.16	138.85	−6.92	3.52	900
J0238.0+5237	02:38:01.18	+52:37:32.16	138.85	−6.92	3.52	1800
J0242.1−0534	02:51:06.14	+26:03:50.76	153.92	−29.51	6.49	1800
J0251.1+2603	03:07:22.39	+49:16:13.44	144.53	−7.82	1.89	600
J0307.3+4916*	03:12:09.79	−09:21:33.48	191.51	−52.36	5.36	1800
J0312.1−0921	04:19:06.77	+66:36:17.64	141.54	11.57	3.25	1800
J0419.1+6636*	04:26:43.51	+54:37:00.48	150.87	3.87	4.26	600
J0426.7+5437	04:53:16.20	+63:21:56.16	146.45	12.17	2.91	1800
J0453.2+6321*	05:03:27.50	+45:22:28.56	161.72	2.34	6.05	1800
J0503.4+4522*	05:23:21.41	−25:28:34.68	228.20	−29.83	2.51	1800
J0523.3−2528	05:40:29.66	+58:23:25.80	153.93	14.26	1.80	1800
J0540.4+5823*	06:09:24.38	−02:48:21.96	210.63	−10.63	2.42	1800
J0609.4−0248*	07:02:43.13	−19:52:14.88	231.94	−6.53	3.42	1800
J0702.7−1952	07:33:18.72	+59:04:00.48	157.97	28.31	8.50	1800
J0733.3+5904	07:44:10.73	−25:23:57.84	241.34	−0.70	3.28	600
J0744.1−2523	08:38:48.98	−28:29:21.12	250.61	7.80	3.34	600
J0838.8−2829	09:53:42.94	−15:10:28.20	251.94	29.61	4.19	600
J0953.7−1510	11:19:56.28	−22:04:02.28	276.47	36.06	2.51	600
J1119.9−2204	11:55:18.48	−11:12:10.44	281.53	49.32	3.05	1800
J1155.3−1112	16:25:07.06	−00:21:30.96	13.88	31.84	2.25	600
J1625.1−0021	16:26:17.30	−24:28:00.84	353.00	16.89	3.41	600
J1626.2−2428c	16:53:40.56	−01:58:48.36	16.62	24.92	2.14	600
J1653.6−0158	17:39:02.28	+87:16:36.12	120.00	27.94	3.29	600
J1739.0+8716*	18:23:16.90	−13:39:04.68	17.60	−0.09	1.73	1800
J1823.2−1339	18:39:23.52	−05:52:53.76	26.33	−0.01	2.05	600
J1839.3−0552	18:44:23.93	−03:44:48.48	28.80	−0.14	3.39	600
J1844.3−0344	18:57:57.65	+02:10:13.44	35.61	−0.46	3.61	600
J1857.9+0210	19:01:35.86	−01:26:53.16	32.80	−2.92	3.35	1800
J1901.5−0126	19:06:41.14	+07:20:02.04	41.19	−0.03	2.22	600
J1906.6+0720	19:25:29.57	+17:27:47.52	52.29	0.64	6.18	1800
J1925.4+1727	20:04:52.68	+70:03:34.92	102.86	19.45	2.57	1800
J2004.8+7003*	20:17:56.33	+36:27:32.76	74.54	0.41	2.06	600
J2017.9+3627	20:18:31.68	+38:51:35.64	76.59	1.66	3.16	1800
J2018.5+3851*	20:32:33.46	+39:21:32.04	78.57	−0.27	5.71	1800
J2032.5+3921	20:33:21.07	+43:48:42.48	82.24	2.26	4.43	1800
J2033.3+4348c*	20:34:28.99	+38:33:50.76	78.16	−1.04	3.17	1800
J2034.4+3833c	20:35:01.85	+36:34:53.04	76.63	−2.32	3.09	600
J2035.0+3634	20:36:53.28	+42:34:05.16	81.63	1.00	4.64	1800

J2036.8+4234c	20:38:29.95	+42:12:30.60	81.53	0.54	3.53	600
J2038.4+4212*	20:41:07.37	+47:36:10.80	86.09	3.46	3.02	600
J2041.1+4736	20:56:42.91	+49:38:29.40	89.30	2.74	1.76	1800
J2056.7+4938*	21:03:46.18	−11:13:44.76	37.86	−34.42	3.95	1800
J2103.7−1113	21:14:05.83	+52:39:08.28	93.37	2.73	4.12	1800
J2114.0+5239*	22:17:13.68	+63:46:25.68	106.86	5.82	4.13	1800
J2217.2+6346	22:33:06.94	+65:42:53.28	109.34	6.56	5.76	1800
J2233.1+6542	23:23:28.85	+58:49:09.48	111.75	−2.13	1.00	600

* indicates the observation is heavily affected by RFI.

[a] R_{95} values are the major-axes of the 95% error ellipses for each source as found in the 3FGL catalog.

Chapter 7

Summary and Outlook

Until the advent of *Fermi*, the majority of the pulsars known were radio selected and most of the pulsar studies were built around the radio framework. This presents a strong selection bias in the way that we study pulsars, which in turn limits our ability to understand the full picture of the pulsar population. We have learnt so much from the radio frequencies but it seems that the knowledge gained solely from the radio is insufficient to fully address all the fundamental questions, such as the Galactic pulsar population, the structure of the pulsar magnetosphere, the emission mechanism across the electromagnetic spectrum, the beaming fraction of pulsar emission at different wavelengths, and channels of pulsar spin-down power losses. Unfortunately, in the last few decades, pulsar studies at other wavelengths such as X-ray and γ-ray were lagging behind mostly because of the technical difficulties of space-based observations, where the positional accuracy and time resolution are very limited. However, this is no longer the case after *Fermi* Gamma-ray Space Telescope (*Fermi*) was launched.

The Large Area Telescope (LAT) on board of *Fermi* is a real game changer, as it enables the study of the pulsar population from a very different angle. In particular, it enables the studies of pulsars with weak or even non-detectable radio emission. *Fermi*-LAT's all-sky surveying mode and excellent time resolution (< 10 μs) enables the discoveries of different types of pulsars through γ-ray pulsations. Many of the young γ-ray pulsars discovered have not yet been detected in subsequent radio searches, such as the majority of pulsars presented in Chapter 4. Pulsars presented in Chapter 4 are young and energetic, their characteristic ages are smaller than 3 Myr and their spin-down powers are larger than 10^{33} erg s^{-1}. They all have low radio fluxes, only two out of the 13 pulsars were detected in deep radio follow-up observations. This radio-quiet γ-ray pulsar population can only be accessed through blind periodicity searches in γ-ray. Therefore, blind periodicity search in γ-ray is the only way to complete the radio-quiet part of the Galactic pulsar census.

Due to the ever-limited computational resources, selecting the right γ-ray sources to perform blind search is one of the keys to increase the chance of finding γ-ray pulsars. Fortunately, their spectral characteristics in γ-ray enable the application of machine-learning algorithms such as the Gaussian Mixture Model (GMM) presented in Chapter 2 to select pulsar-like γ-ray sources from the 3FGL catalog for our survey in Chapters 4 and 5. With the help of the semi-coherent search algorithm and Gaussian Mixture Model, we were able to detect 17 new γ-ray pulsars out of 118 selected 3FGL sources. For those 3FGL sources where no detection has been made, some of them may fall below the blind search sensitivity or they could be MSPs in binary systems.

In addition, we were also able to detect γ-ray pulsars that could not be detected

in the past. For example, the young energetic PSR J1906+0720 (Section 5.1) was found in our data despite the giant glitch, one of the largest detected from a γ-ray pulsar, that occurred in the first year of the *Fermi* mission. Several complications for detecting PSR J1906+0720 were the positional offset caused by a previously undetected secondary γ-ray source, and the intense Galactic γ-ray diffuse emission. The detection of PSR J1906+0720 allows us to further improve our understanding of the energetic pulsar population. The 2,700 years old PSR J1208−6238 (Section 5.2) is the youngest radio-quiet γ-ray pulsar ever discovered, its high surface magnetic field strength (3.8×10^{13} G) and small characteristic age allow us to measure its braking index ($n = 2.598 \pm 0.01$) and thus study the spin-down process. The braking index of PSR J1208−6238 deviates from the simple dipole braking model ($n = 3$) which implies that the spin-down mechanism is not a pure magneto-dipole radiation. These studies are rare, so far ten pulsars offered such an opportunity. PSRs J1035−6720 and J1744−7619 (Section 5.3) are the only two isolated MSPs discovered without any information from other wavelengths. Despite the deep follow-up radio observations with the Parkes radio telescope, PSR J1744−7619 is still radio-quiet ($S_{1400} < 31$ μJy) while the best-fit emission geometry from its γ-ray pulse profile suggested otherwise. Other inconsistencies between models and observations have been found, such as PSR J0631+0646 (Chapter 4) where the current emission models failed to predict the observed radio-γ-ray phase lag. The discovery of PSRs J0631+0646 and J1744−7619 demand new approaches in emission modelling to explain the observables.

Despite the competition from a number of all-sky radio pulsar surveys, a significant portion of radio pulsars were found from targeted radio searches of unassociated LAT sources. This demonstrates that targeted searches of unassociated LAT sources are a complementary way to complete our knowledge on the pulsar population, especially for MSPs in binary systems. Phased Array Feed and Ultra-Wide-Bandwidth receivers are the main technologies for the next generation radio telescopes. The Ultra-Broad-Band receiver (UBB) is one of the prototypes of the Ultra-Wide-Bandwidth receiver technology being developed at the Effelsberg telescope. We explored the possibility of using the UBB for targeted pulsar searches on unassociated LAT sources at Effelsberg (Chapter 6). Unfortunately, UBB was strongly affected by Radio Frequency Interference (RFI) at the Effelsberg site. As a result, almost half of the observations were strongly affected because of the RFI. Also, the strong RFI at Effelsberg increased the system temperature ($T_{\rm sys}$) of the UBB by a factor > 2. Although we have not detected any radio pulsations, the experience gained from the survey provides valuable information, such as local RFI monitoring for future surveys at Effelsberg. Using the RFI information from the UBB survey, a new RFI filter is being developed at Effelsberg should bring the UBB sensitivity back to its nominal $T_{\rm sys} \simeq 20$ K, allowing pulsar broad-band spectral studies and targeted pulsar surveys. As similar Ultra-Wide-Band receiver technology are being developed for next generation radio telescopes like MeerKAT and the Square Kilometre Array (SKA), the lesson we have learnt from the UBB survey is beneficial in the deployment of the future Ultra-Wide-Bandwidth receivers. For example, although we may have missed some steep-spectrum radio pulsars in the UBB survey, the SKA-LOW pulsar survey which is designed to operate in low frequency (100 - 450 MHz), is

going to target this subset of pulsars.

Nevertheless, there are still a number of pulsar-like unassociated γ-ray sources ready to be searched when computational power is available. Meanwhile, a targeted binary pulsar survey on Einstein@Home has also started in collaboration with L. Nieder, using the constraints on the orbital parameters from optical/X-ray observations and the weight calculation pipeline described in Section 2.4. In the near future, we will apply the GMM classification scheme to the next version of the *Fermi* source catalog (i.e. 4FGL) with an addition of over 2000 γ-ray sources. Surely, more interesting pulsar discoveries will be made with the improved classification scheme and blind search techniques, stepping closer to the complete picture of the Galactic pulsar population. It is likely that more pulsars similar to the radio-quiet MSP PSR J1744−7619 will be discovered. These discoveries will continuously challenge and put new constraints on pulsar emission models.

The detection rate of LAT pulsars has been steady for the last nine years (Guillemot, 2017). This is unexpected as the detection rate should have levelled off as the extra sensitivity gain by increasing exposure time is scaled as its square root of the exposure. The steady increase of the LAT-detected pulsars is due to different factors: the improved Pass 8 LAT data which increases our sensitivity, the deployment of the semi-coherent blind search algorithm and new high-performance radio receivers which also led to more radio pulsar discoveries in unassociated LAT sources. As *Fermi* enters its 10th mission year in 2018, hopefully the LAT will continue to provide more exciting discoveries. Moreover, the synergies between MeV-GeV-TeV γ-ray observatories will be an important factor leading to more γ-ray pulsar discoveries. For example, there is an emerging class of high $\dot{E}$ and high $B_{\rm s}$ γ-ray pulsars with spectral cutoffs below a few hundred MeV, meaning they are very hard to be detected in LAT energy range. Also, the pulsed TeV detection of Crab pulsar by the Major Atmospheric Gamma Imaging Cherenkov (MAGIC) telescope (Ansoldi et al., 2016) implies that other young energetic pulsars such as Vela and Geminga could also be detected by future TeV Cherenkov telescopes. In the next decade, new space based γ-ray instruments with good sensitivity and angular resolution in the MeV energy range such as the All-Sky Medium Energy Gamma-Ray Observatory (AMEGO), Hermetic ARgon POlarimeter (HARPO) and e-ASTROGAM. Also new ground based TeV observatories such as the Cherenkov Telescope Array (CTA) will provide a factor of 5 to 10 improvement in sensitivity compare to the current generation of Cherenkov telescopes such as MAGIC, High Energy Stereoscopic System (H.E.S.S.) and Very Energetic Radiation Imaging Telescope Array System (VERITAS). These new γ-ray projects will surely provide new insight for pulsar studies in MeV to TeV γ-rays and provide crucial information to address all the open questions about pulsars.

Bibliography

Abbott B., et al., 2008, Physical Review Letters, 101, 211102 (Cited on page 18.)

Abdo A. A., et al., 2008, Science, 322, 1218 (Cited on pages 2 and 14.)

Abdo A. A., et al., 2009a, ApJS, 183, 46 (Cited on page 35.)

Abdo A. A., Ackermann M., Ajello M., Anderson 2009b, Science, 325, 840 (Cited on pages 14, 17, 58 and 74.)

Abdo A. A., et al., 2009c, ApJ, 699, 1171 (Cited on page 14.)

Abdo A. A., et al., 2010a, ApJS, 188, 405 (Cited on pages 23 and 35.)

Abdo A. A., et al., 2010b, A&A, 524, A75 (Cited on page 14.)

Abdo A. A., Ackermann M., Ajello M., Baldini L., 2010c, ApJ, 711, 64 (Cited on page 59.)

Abdo A. A., et al., 2013, ApJS, 208, 17 (Cited on pages vii, xi, 2, 9, 16, 19, 59, 90, 94, 99, 100, 102, 105 and 106.)

Ables J. G., Manchester R. N., 1976, A&A, 50, 177 (Cited on page 7.)

Acero F., Ackermann M., Ajello M., et al., 2015, ApJS, 218, 23 (Cited on pages viii, 18, 35, 36, 37, 38, 60 and 107.)

Acero F., et al., 2016a, ApJS, 223, 26 (Cited on page 64.)

Acero F., et al., 2016b, ApJS, 224, 8 (Cited on pages 78 and 100.)

Ackermann M., et al., 2012, The Astrophysical Journal Supplement Series, 203, 4 (Cited on page 30.)

Ackermann M., et al., 2015, Physical Review Letters, 115, 231301 (Cited on page 103.)

Allafort A., et al., 2013, ApJ, 777, L2 (Cited on pages 35 and 60.)

Allen B., et al., 2013, ApJ, 773, 91 (Cited on page 18.)

Ansoldi S., et al., 2016, A&A, 585, A133 (Cited on page 119.)

Archibald R. F., et al., 2016, ApJ, 819, L16 (Cited on page 6.)

Atwood W. B., Ziegler M., Johnson R. P., Baughman B. M., 2006, ApJ, 652, L49 (Cited on page 17.)

Atwood W. B., et al., 2009, ApJ, 697, 1071 (Cited on pages xiii, 13, 30 and 58.)

Atwood W., et al., 2013, preprint, (arXiv:1303.3514) (Cited on pages 30, 59 and 94.)

Barr E. D., et al., 2013, MNRAS, 429, 1633 (Cited on pages 14, 58, 75 and 90.)

Bassa C. G., et al., 2017, ApJ, 846, L20 (Cited on page 112.)

Bates S. D., Lorimer D. R., Verbiest J. P. W., 2013, MNRAS, 431, 1352 (Cited on page 108.)

Berezina M., et al., 2017, MNRAS, 470, 4421 (Cited on page 11.)

Bhattacharya D., van den Heuvel E. P. J., 1991, Phys. Rep., 203, 1 (Cited on page 11.)

Bhattacharyya B., et al., 2013, ApJ, 773, L12 (Cited on pages 14 and 58.)

Bignami G. F., et al., 1975, Space Science Instrumentation, 1, 245 (Cited on page 2.)

Blandford R. D., Romani R. W., 1988, MNRAS, 234, 57P (Cited on page 6.)

Blasi P., 2013, A&A Rev., 21, 70 (Cited on page 2.)

Boyles J., et al., 2013, ApJ, 763, 80 (Cited on page 75.)

Bradt H., Rappaport S., Mayer W., 1969, Nature, 222, 728 (Cited on page 2.)

Breed M., Venter C., Harding A. K., Johnson T. J., 2015, preprint, (arXiv:1504.06816) (Cited on pages vii and 22.)

Browning R., Ramsden D., Wright P. J., 1971, Nature Physical Science, 232, 99 (Cited on page 2.)

Burgay M., et al., 2006, MNRAS, 368, 283 (Cited on page 111.)

Burrows D. N., et al., 2005, Space Sci. Rev., 120, 165 (Cited on page 72.)

Camilo F., 1996, in Johnston S., Walker M. A., Bailes M., eds, Astronomical Society of the Pacific Conference Series Vol. 105, IAU Colloq. 160: Pulsars: Problems and Progress. p. 539 (Cited on page 11.)

Camilo F., Rasio F. A., 2005, in Rasio F. A., Stairs I. H., eds, Astronomical Society of the Pacific Conference Series Vol. 328, Binary Radio Pulsars. p. 147 (arXiv:astro-ph/0501226) (Cited on page 14.)

Camilo F., et al., 2009, ApJ, 705, 1 (Cited on page 59.)

Camilo F., et al., 2012, ApJ, 746, 39 (Cited on pages 14 and 58.)

Camilo F., et al., 2015, ApJ, 810, 85 (Cited on pages 14, 58, 101, 102 and 113.)

Caraveo P. A., 2014, Annual Review of Astronomy and Astrophysics, 52, 211 (Cited on page 95.)

Cash W., 1979, ApJ, 228, 939 (Cited on page 73.)

Charles E., et al., 2016, Phys. Rep., 636, 1 (Cited on page 103.)

Chen K., Ruderman M., 1993, ApJ, 402, 264 (Cited on page 9.)

Cheng K. S., Ho C., Ruderman M., 1986, ApJ, 300, 500 (Cited on pages 23 and 70.)

Clark C. J., et al., 2015, ApJ, 809, L2 (Cited on pages x, xi, xiii, 58, 59, 63, 88, 89, 90, 91, 92, 93, 96 and 97.)

Clark C. J., et al., 2016, ApJL, 832, L15 (Cited on pages xi, 63, 70, 88, 89, 98, 99 and 100.)

Clark C. J., et al., 2017, ApJ, 834, 106 (Cited on pages 59, 89 and 105.)

Cocke W. J., Disney M. J., Taylor D. J., 1969, Nature, 221, 525 (Cited on page 2.)

Cognard I., et al., 2011, ApJ, 732, 47 (Cited on pages 14 and 58.)

Cordes J. M., Lazio T. J. W., 2002, ArXiv Astrophysics e-prints, (Cited on pages 9, 72, 80, 102 and 111.)

Cordes J. M., et al., 2006, ApJ, 637, 446 (Cited on page 75.)

Coroniti F. V., 1990, ApJ, 349, 538 (Cited on page 25.)

Cromartie H. T., et al., 2016, ApJ, 819, 34 (Cited on pages 14, 58 and 113.)

Deneva J. S., Stovall K., McLaughlin M. A., Bates S. D., Freire P. C. C., Martinez J. G., Jenet F., Bagchi M., 2013, ApJ, 775, 51 (Cited on page 75.)

Derdeyn S. M., Ehrmann C. H., Fichtel C. E., Kniffen D. A., Ross R. W., 1972, Nuclear Instruments and Methods, 98, 557 (Cited on page 2.)

Deutsch A. J., 1955, Annales d'Astrophysique, 18, 1 (Cited on page 70.)

Dyks J., Rudak B., 2003, ApJ, 598, 1201 (Cited on pages 23 and 70.)

Edwards R. T., Bailes M., van Straten W., Britton M. C., 2001, MNRAS, 326, 358 (Cited on page 111.)

Espinoza C. M., Lyne A. G., Kramer M., Manchester R. N., Kaspi V. M., 2011, ApJ, 741, L13 (Cited on page 6.)

Evans P. A., et al., 2014, ApJS, 210, 8 (Cited on page 73.)

Faucher-Giguère C.-A., Kaspi V. M., 2006, ApJ, 643, 332 (Cited on page 111.)

Fermi-LAT Collaboration 2017, preprint, (arXiv:1705.00009) (Cited on page 75.)

Fisher R., 1925, Statistical methods for research workers. Edinburgh Oliver & Boyd (Cited on page 30.)

Freire P. C. C., et al., 2011, Science, 334, 1107 (Cited on page 14.)

Garmire G. P., Bautz M. W., Ford P. G., Nousek J. A., Ricker Jr. G. R., 2003, in Truemper J. E., Tananbaum H. D., eds, Proc. SPIEVol. 4851, X-Ray and Gamma-Ray Telescopes and Instruments for Astronomy.. pp 28–44, doi:10.1117/12.461599 (Cited on page 72.)

Goldreich P., Julian W. H., 1969, ApJ, 157, 869 (Cited on page 19.)

Gomez-Gonzalez J., Guelin M., 1974, A&A, 32, 441 (Cited on page 7.)

Graham-Smith F., 2003, Reports on Progress in Physics, 66, 173 (Cited on page 21.)

Guillemot L., 2017, Proc. 7th international Fermi Symposium (Cited on page 119.)

Guillemot L., et al., 2012a, MNRAS, 422, 1294 (Cited on pages 14 and 58.)

Guillemot L., et al., 2012b, ApJ, 744, 33 (Cited on pages x, xi, 65 and 96.)

Guillemot L., et al., 2013, ApJ, 768, 169 (Cited on page 71.)

Halpern J. P., Holt S. S., 1992, Nature, 357, 222 (Cited on page 19.)

Harding A. K., 2009, in Becker W., ed., Astrophysics and Space Science Library Vol. 357, Astrophysics and Space Science Library. p. 521, doi:10.1007/978-3-540-76965-1_19 (Cited on page 23.)

Harding A. K., Contopoulos I., Kazanas D., 1999, ApJ, 525, L125 (Cited on page 6.)

Harding A. K., Gonthier P. L., Ouellette M. S., O'Brien S., Berrier J., 2002, in Slane P. O., Gaensler B. M., eds, Astronomical Society of the Pacific Conference Series Vol. 271, Neutron Stars in Supernova Remnants. p. 335 (Cited on page 19.)

Harding A. K., Grenier I. A., Gonthier P. L., 2007, Ap&SS, 309, 221 (Cited on page 19.)

Haslam C. G. T., Salter C. J., Stoffel H., Wilson W. E., 1982, A&AS, 47, 1 (Cited on page 69.)

Hermsen W., et al., 1977, Nature, 269, 494 (Cited on page 2.)

Hessels J. W. T., Ransom S. M., Stairs I. H., Freire P. C. C., Kaspi V. M., Camilo F., 2006, Science, 311, 1901 (Cited on page 11.)

Hessels J. W. T., et al., 2011, in Burgay M., D'Amico N., Esposito P., Pellizzoni A., Possenti A., eds, American Institute of Physics Conference Series Vol. 1357, American Institute of Physics Conference Series. pp 40–43 (arXiv:1101.1742), doi:10.1063/1.3615072 (Cited on page 108.)

Hewish A., Bell S. J., Pilkington J. D. H., Scott P. F., Collins R. A., 1968, Nature, 217, 709 (Cited on pages 2 and 58.)

Hobbs G., 2011, Astrophysics and Space Science Proceedings, 21, 229 (Cited on page 3.)

Hui C. Y., et al., 2015, The Astrophysical Journal, 809, 68 (Cited on page 101.)

Hulse R. A., Taylor J. H., 1975, ApJ, 195, L51 (Cited on page 3.)

Jacoby B. A., Bailes M., Ord S. M., Edwards R. T., Kulkarni S. R., 2009, ApJ, 699, 2009 (Cited on page 111.)

Jiang B., Chen Y., Wang J., Su Y., Zhou X., Safi-Harb S., DeLaney T., 2010, ApJ, 712, 1147 (Cited on page 94.)

Johnson T. J., et al., 2013, ApJ, 778, 106 (Cited on page 14.)

Johnson T. J., et al., 2014, ApJS, 213, 6 (Cited on pages viii, 26, 27, 28, 70, 71 and 102.)

Kalapotharakos C., Harding A. K., Kazanas D., Contopoulos I., 2012, ApJ, 754, L1 (Cited on page 71.)

Kalapotharakos C., Harding A. K., Kazanas D., 2014, ApJ, 793, 97 (Cited on page 71.)

Keith M. J., et al., 2010, MNRAS, 409, 619 (Cited on page 75.)

Keith M. J., et al., 2011, MNRAS, 414, 1292 (Cited on pages 14 and 58.)

Kerr M., 2010, PhD thesis, University of Washington (Cited on pages 35, 40 and 61.)

Kerr M., 2011, ApJ, 732, 38 (Cited on pages 18, 48 and 61.)

Kerr M., et al., 2012, ApJ, 748, L2 (Cited on pages 14 and 58.)

Kong A. K. H., Hui C. Y., Cheng K. S., 2010, ApJ, 712, L36 (Cited on page 14.)

Kouwenhoven M. L. A., Voûte J. L. L., 2001, A&A, 378, 700 (Cited on page 110.)

Kramer M., Xilouris K. M., Lorimer D. R., Doroshenko O., Jessner A., Wielebinski R., Wolszczan A., Camilo F., 1998, ApJ, 501, 270 (Cited on pages 17, 103 and 112.)

Kramer M., et al., 2006, Science, 314, 97 (Cited on page 3.)

Lee K. J., Guillemot L., Yue Y. L., Kramer M., Champion D. J., 2012, MNRAS, 424, 2832 (Cited on pages 18, 35, 40 and 60.)

Lee K. J., et al., 2013, MNRAS, 433, 688 (Cited on page 48.)

Li K.-L., Kong A. K. H., Hou X., Mao J., Strader J., Chomiuk L., Tremou E., 2016, ApJ, 833, 143 (Cited on pages 75 and 103.)

López-Coto R., 2016, in European Physical Journal Web of Conferences. p. 04007 (arXiv:1509.09173), doi:10.1051/epjconf/201612104007 (Cited on page 3.)

Lorimer D. R., 2008, Living Reviews in Relativity, 11, 8 (Cited on page 103.)

Lorimer D. R., 2011, SIGPROC: Pulsar Signal Processing Programs, Astrophysics Source Code Library (ascl:1107.016) (Cited on page 44.)

Lorimer D., Kramer M., 2005, Handbook of Pulsar Astronomy. Cambridge University Press, Cambridge (Cited on pages vii, viii, 3, 4, 8, 23, 46, 68 and 110.)

Lorimer D. R., Yates J. A., Lyne A. G., Gould D. M., 1995, MNRAS, 273, 411 (Cited on page 112.)

Lorimer D. R., et al., 2006, MNRAS, 372, 777 (Cited on pages 47 and 111.)

Lyne A. G., Pritchard R. S., Graham-Smith F., 1993, MNRAS, 265, 1003 (Cited on page 6.)

Lyne A. G., Pritchard R. S., Graham-Smith F., Camilo F., 1996, Nature, 381, 497 (Cited on page 6.)

Lyne A., Graham-Smith F., Weltevrede P., Jordan C., Stappers B., Bassa C., Kramer M., 2013, Science, 342, 598 (Cited on page 6.)

Maan Y., 2015, ApJ, 815, 126 (Cited on page 59.)

Maan Y., Aswathappa H. A., Deshpande A. A., 2012, MNRAS, 425, 2 (Cited on page 59.)

Manchester R. N., 2005, Ap&SS, 297, 101 (Cited on pages 17 and 103.)

Manchester R. N., et al., 2001, MNRAS, 328, 17 (Cited on page 111.)

Marelli M., Mignani R. P., De Luca A., Saz Parkinson P. M., Salvetti D., Den Hartog P. R., Wolff M. T., 2015, ApJ, 802, 78 (Cited on page 73.)

Maron O., Kijak J., Kramer M., Wielebinski R., 2000, AASS, 147, 195 (Cited on page 112.)

Marshall F. E., Guillemot L., Harding A. K., Martin P., Smith D. A., 2016, The Astrophysical Journal Letters, 827, L39 (Cited on page 6.)

Mattox J. R., et al., 1996, ApJ, 461, 396 (Cited on page 30.)

Menou K., Perna R., Hernquist L., 2001, ApJ, 554, L63 (Cited on page 6.)

Michel F. C., Tucker W. H., 1969, Nature, 223, 277 (Cited on page 6.)

Mignani R. P., et al., 2017, preprint, (arXiv:1708.02828) (Cited on page 58.)

Mirabal N., Frías-Martinez V., Hassan T., Frías-Martinez E., 2012, MNRAS, 424, L64 (Cited on pages 18, 35 and 60.)

Muslimov A. G., Harding A. K., 2003, ApJ, 588, 430 (Cited on pages 23 and 70.)

Muslimov A. G., Harding A. K., 2004a, ApJ, 606, 1143 (Cited on pages 23 and 70.)

Muslimov A. G., Harding A. K., 2004b, ApJ, 617, 471 (Cited on page 25.)

Ng C., et al., 2015, MNRAS, 450, 2922 (Cited on page 113.)

Nolan P. L., et al., 2012, ApJS, 199, 31 (Cited on page 35.)

Pétri J., 2012, MNRAS, 424, 2023 (Cited on page 25.)

Pierbattista M., Harding A. K., Grenier I. A., Johnson T. J., Caraveo P. A., Kerr M., Gonthier P. L., 2015, A&A, 575, A3 (Cited on pages 70 and 71.)

Pletsch H. J., Clark C. J., 2014, ApJ, 795, 75 (Cited on pages x, 48, 51 and 92.)

Pletsch H. J., et al., 2012a, Science, 338, 1314 (Cited on pages 18, 75 and 101.)

Pletsch H. J., Guillemot L., Allen B., et al., 2012b, ApJ, 744, 105 (Cited on pages xi, 18, 58, 59, 60, 74, 90 and 96.)

Pletsch H. J., et al., 2013, ApJ, 779, L11 (Cited on pages 18, 74 and 101.)

Pleunis Z., et al., 2017, ApJ, 846, L19 (Cited on page 112.)

Press W. H., Teukolsky S. A., Vetterling W. T., Flannery B. P., 2007, Numerical Recipes 3rd Edition: The Art of Scientific Computing, 3 edn. Cambridge University Press, New York, NY, USA (Cited on page 40.)

Ransom S., 2011, PRESTO: PulsaR Exploration and Search TOolkit, Astrophysics Source Code Library (ascl:1107.017) (Cited on pages 44 and 109.)

Ransom S. M., Eikenberry S. S., Middleditch J., 2002, AJ, 124, 1788 (Cited on page 47.)

Ransom S. M., et al., 2011, ApJ, 727, L16 (Cited on pages 14 and 58.)

Ravi V., Manchester R. N., Hobbs G., 2010, ApJ, 716, L85 (Cited on pages 17 and 103.)

Ray P. S., et al., 2013, ApJ, 763, L13 (Cited on pages 101 and 108.)

Romani R. W., 2012, ApJ, 754, L25 (Cited on page 90.)

Safi-Harb S., Dubner G., Petre R., Holt S. S., Durouchoux P., 2005, ApJ, 618, 321 (Cited on page 94.)

Salvetti D., et al., 2015, ApJ, 814, 88 (Cited on pages 72, 73, 75 and 103.)

Salvetti D., et al., 2017, preprint, (`arXiv:1702.00474`) (Cited on pages 75 and 103.)

Saz Parkinson P. M., Dormody M., Ziegler M., 2010, ApJ, 725, 571 (Cited on pages 17 and 58.)

Saz Parkinson P. M., Xu H., Yu P. L. H., Salvetti D., Marelli M., Falcone A. D., 2016, ApJ, 820, 8 (Cited on pages 18, 35, 60, 74 and 101.)

Scargle J. D., Norris J. P., Jackson B., Chiang J., 2013, ApJ, 764, 167 (Cited on page 64.)

Slane P., Seward F. D., Bandiera R., Torii K., Tsunemi H., 1997, ApJ, 485, 221 (Cited on page 14.)

Spruit H. C., 2009, in Strassmeier K. G., Kosovichev A. G., Beckman J. E., eds, IAU Symposium Vol. 259, Cosmic Magnetic Fields: From Planets, to Stars and Galaxies. pp 61–74, doi:10.1017/S1743921309030075 (Cited on page 4.)

Story S. A., Gonthier P. L., Harding A. K., 2007, ApJ, 671, 713 (Cited on pages 17, 70 and 103.)

Stroh M. C., Falcone A. D., 2013, ApJS, 207, 28 (Cited on page 72.)

Strüder L., et al., 2001, A&A, 365, L18 (Cited on page 72.)

Swiggum J. K., et al., 2015, ApJ, 805, 156 (Cited on page 11.)

Swiggum J. K., et al., 2017, ApJ, 847, 25 (Cited on page 58.)

Takata J., Wang Y., Cheng K. S., 2010, ApJ, 715, 1318 (Cited on pages viii, 23 and 24.)

Takata J., Wang Y., Cheng K. S., 2011, MNRAS, 415, 1827 (Cited on page 103.)

Tam P. H. T., Kong A. K. H., Hui C. Y., Cheng K. S., Li C., Lu T.-N., 2011, ApJ, 729, 90 (Cited on page 14.)

Taylor J. H., Huguenin G. R., 1969, Nature, 221, 816 (Cited on page 46.)

Thompson D. J., 2004, in Camilo F., Gaensler B. M., eds, IAU Symposium Vol. 218, Young Neutron Stars and Their Environments. p. 399 (arXiv:astro-ph/0310509) (Cited on pages vii and 12.)

Thompson D. J., 2008, Reports on Progress in Physics, 71, 116901 (Cited on page 2.)

Thompson D. J., Fichtel C. E., Kniffen D. A., Ogelman H. B., 1975, ApJ, 200, L79 (Cited on page 2.)

Thompson D. J., et al., 1993, ApJS, 86, 629 (Cited on pages xiii and 13.)

Turner M. J. L., et al., 2001, A&A, 365, L27 (Cited on page 72.)

Venter C., Harding A. K., Guillemot L., 2009, ApJ, 707, 800 (Cited on pages 25 and 70.)

Watters K. P., Romani R. W., Weltevrede P., Johnston S., 2009, ApJ, 695, 1289 (Cited on page 70.)

Weinstein A., 2014, Nuclear Physics B Proceedings Supplements, 256, 136 (Cited on page 3.)

Wilks S. S., 1938, Ann. Math. Statist., 9, 60 (Cited on page 32.)

Wu J. H. K., Hui C. Y., Wu E. M. H., Kong A. K. H., Huang R. H. H., Tam P. H. T., Takata J., Cheng K. S., 2013, ApJ, 765, L47 (Cited on page 14.)

Xing Y., Wang Z., 2014, PASJ, 66, 72 (Cited on page 90.)

Yao J. M., Manchester R. N., Wang N., 2017, ApJ, 835, 29 (Cited on pages 9, 72, 80 and 102.)

Zhu W. W., et al., 2014, ApJ, 781, 117 (Cited on page 48.)

Ziegler M., Baughman B. M., Johnson R. P., Atwood W. B., 2008, ApJ, 680, 620 (Cited on page 17.)

de Jager O. C., Raubenheimer B. C., Swanepoel J. W. H., 1989, A&A, 221, 180 (Cited on pages 53 and 70.)

Acknowledgements

There is no way this thesis could be completed without the help and support from many people, I would like to express my greatest gratitude in the following paragraphs.

Firstly, I would like to thank my advisor David, Lucas and Michael for the patience and guidance over the past four years. Research is not easy when you are the only student in the group who studies γ-ray pulsars. You always give me new ideas and vision to tackle on problems that I have encountered.

I would like to thank all the colleagues of the Fundi group who had helped me on different aspects, not to mention those entertaining conversations during coffee breaks. I want to thank K.J. Lee in particular who taught me how to apply machine leaning algorithm to the γ-ray data, also Ramesh Karuppusamy who explained me how the UBB back-end and the observing system works, and helped me through numerous Effelsberg observations.

I would like to thank Holger Pletsch, Colin Clark and Lars Nieder for designing and implementing the blind search algorithm on Einstein@Home, without the powerful blind search algorithm we would not have those exciting pulsar discoveries. I have to specially thank Colin for the collaboration on the Einstein@Home blind search project and keep updating me with exciting discoveries, it is a pleasure to work with you.

I would like to thank K.S. Cheng, Albert Kong and David Hui for introducing me to the world of astrophysics. If it wasn't the final year project that I've done at HKU, I wouldn't have the chance to continue my study in astrophysics and explore different parts of the world. I also want to thank Mr. Lee, my high school physics teacher, who taught me how to appreciate the beauty of physics.

I would like to thank everyone I worked with in the *Fermi*-LAT collaboration, especially Paul Ray, Regina Caputo, David Salvetti, Julia Deneva, Tyrel Johnson, Matthew Kerr, David Smith, Jean Ballet, Seth Digel, David Thompson, Francesco de Palma for their hard work and helpful advice. Your valuable input to the papers in any forms are vital.

I would like to thank to all the students in the group, especially those who shared offices with me. I would like to specially thank Pablo Torne for sharing his experiences in radio astronomy and motivating the work we have done together for the UBB survey, I have learn a lot from you. Also I would like to thank Alessandro Ridolfi and Nicolas Caballero for numerous scientific discussions and Open Arena sessions. Many thanks to fellow students in the group, my horizon has widened thanks to those strange discussions in my office and around the lunch table. Also I have to thank all my friends in Hong Kong who keep me entertained from time to time.

I would also thank all the administrative staffs especially Kira Kühn, Barbara Menten and Le Tran who helped me through many confusing German regulations.

I would like to thank my fiancée Ann who supported me while I was writing, thank you for proofreading my thesis and making suggestions. Sorry I have lower your English level by asking you weird questions about grammar.

I would like to thank my parents Sam and Kicoo and my brother Terence, they have always supported me to pursue my dreams. Without your support this would not be possible.

Erklärung

Ich versichere, dass ich die von mir vorgelegte Dissertation selbständig angefertigt, die benutzten Quellen und Hilfsmittel vollständig angegeben und die Stellen der Arbeit- einschlielich Tabellen, Karten und Abbildungen –, die anderen Werken im Wortlaut oder dem Sinn nach entnommen sind, in jedem Einzelfall als Entlehnung kenntlich gemacht habe; dass diese Dissertation noch keiner anderen Fakultät oder Universität zur Prfung vorgelegen hat; dass sie noch nicht verffentlicht worden ist sowie, da ich eine solche Veröffentlichung vor Abschluss des Promotionsverfahrens nicht vornehmen werde. Die Bestimmungen dieser Promotionsordnung sind mir bekannt. Die von mir vorgelegte Dissertation ist von Prof. Dr. Michael Kramer betreut worden.

Unterschift:

_____

Datum:

_____

Publications list

C. J. Clark, **J. Wu**, H. J. Pletsch, L. Guillemot, B. Allen, C. Aulbert, C. Beer, O. Bock, A. Cuéllar, H. B. Eggenstein, H. Fehrmann, M. Kramer, B. Machenschalk, and L. Nieder, *The Einstein@Home Gamma-ray Pulsar Survey. I. Search Methods, Sensitivity, and Discovery of New Young Gamma-ray Pulsars*, The Astrophysical Journal, Volume 834, 2, 2017

C. J. Clark, H. J. Pletsch, **J. Wu**, L. Guillemot, F. Camilo, T. J. Johnson, M. Kerr, B. Allen, C. Aulbert, C. Beer, O. Bock, A. Cuéllar, H. B. Eggenstein, H. Fehrmann, M. Kramer, B. Machenschalk, and L. Nieder, *The Braking Index of A Radio-quiet Gamma-ray Pulsar*, The Astrophysical Journal Letter, Volume 832, 1, 2016

C. J. Clark, H. J. Pletsch, **J. Wu**, L. Guillemot, M. Ackermann, B. Allen, A. de Angelis, C. Aulbert, L. Baldini, J. Ballet, G. Barbiellini, D. Bastieri, R. Bellazzini, E. Bissaldi, O. Bock, R. Bonino, E. Bottacini, T. J. Brandt, J. Bregeon, P. Bruel, S. Buson, G. A. Caliandro, R. A. Cameron, M. Caragiulo, P. A. Caraveo, C. Cecchi, D. J. Champion, E. Charles, A. Chekhtman, J. Chiang, G. Chiaro, S. Ciprini, R. Claus, J. Cohen-Tanugi, A. Cuéllar, S. Cutini, F. D'Ammando, R. Desiante, P. S. Drell, H. B. Eggenstein, C. Favuzzi, H. Fehrmann, E. C. Ferrara, W. B. Focke, A. Franckowiak, P. Fusco, F. Gargano, D. Gasparrini, N. Giglietto, F. Giordano, T. Glanzman, G. Godfrey, I. A. Grenier, J. E. Grove, S. Guiriec, A. K. Harding, E. Hays, J. W. Hewitt, A. B. Hill, D. Horan, X. Hou, T. Jogler, A. S. Johnson, G. Jóhannesson, M. Kramer,1, F. Krauss, M. Kuss, H. Laffon, S. Larsson, L. Latronico, J. Li, L. Li, F. Longo, F. Loparco, M. N. Lovellette, P. Lubrano, B. Machenschalk, A. Manfreda, M. Marelli, M. Mayer, M. N. Mazziotta, P. F. Michelson, T. Mizuno, M. E. Monzani, A. Morselli, I. V. Moskalenko, S. Murgia, E. Nuss, T. Ohsugi, M. Orienti, E. Orlando, F. de Palma, D. Paneque, M. Pesce-Rollins, F. Piron, G. Pivato, S. Rainò, R. Rando, M. Razzano, A. Reimer, P. M. Saz Parkinson, M. Schaal, A. Schulz, C. Sgrò, E. J. Siskind, F. Spada, G. Spandre, P. Spinelli, D. J. Suson, H. Takahashi, J. B. Thayer, L. Tibaldo, P. Torne, D. F. Torres, G. Tosti, E. Troja, G. Vianello, K. S. Wood, M. Wood, and M. Yassine, *PSR J1906+0722: An Elusive γ-ray Pulsar*, The Astrophysical Journal Letter, Volume 809, 1, 2015

J. Wu, C. J. Clark, H. J. Pletsch, L. Guillemot, T. J. Johnson, P. Torne, D. J. Champion, J. Deneva, P. S. Ray, D. Salvetti, M. Kramer, C. Aulbert, C. Beer, B. Bhattacharyya, O. Bock, F. Camilo, I. Cognard, A. Cuéllar, H. B. Eggenstein, H. Fehrmann, E. C. Ferrara, M. Kerr, B. Machenschalk, S. M. Ransom, S. Sanpa-Arsa, K. Wood, *The*

Einstein@Home Gamma-Ray Pulsar Survey II. Source Selection, Spectral Analysis and Multi-wavelength Follow-up, The Astrophysical Journal, Volume 854, Number 2, 2018

C. J. Clark, H. J. Pletsch, **J. Wu**, L. Guillemot, M. Kerr, T. J. Johnson, F. Camilo, D. Salvetti, B. Allen, D. Anderson, C. Aulbert, C. Beer, O. Bock, A. Cuéllar, H. B. Eggenstein, H. Fehrmann, M. Kramer, S. A. Kwang, B. Machenschalk, L. Nieder, M. Ackermann, M. Ajello, L. Baldini, J. Ballet, G. Barbiellini, D. Bastieri, R. Bellazzini, E. Bissaldi, R. D. Blandford, E. D. Bloom, R. Bonino, E. Bottacini, T. J. Brandt, J. Bregeon, P. Bruel, R. Buehler, T. H. Burnett, S. Buson, R. A. Cameron, R. Caputo, P. A. Caraveo, E. Cavazzuti, C. Cecchi, E. Charles, A. Chekhtman, S. Ciprini, L. R. Cominsky, D. Costantin, S. Cutini, F. D'Ammando, A. De Luca, R. Desiante, L. Di Venere, M. Di Mauro, N. Di Lalla, S. W. Digel, C. Favuzzi, E. C. Ferrara, A. Franckowiak, Y. Fukazawa, S. Funk, P. Fusco, F. Gargano, D. Gasparrini, N. Giglietto, F. Giordano, M. Giroletti, G. A. Gomez-Vargas, D. Green, I. A. Grenier, S. Guiriec A. K. Harding, J. W. Hewitt, D. Horan, G. Jóhannesson, S. Kensei, M. Kuss, G. La Mura, S. Larsson, L. Latronico, J. Li, F. Longo, F. Loparco, M. N. Lovellette, P. Lubrano, J. D. Magill, S. Maldera, A. Manfreda, M. N. Mazziotta, J. E. McEnery, P. F. Michelson, N. Mirabal, W. Mitthumsiri, T. Mizuno, M. E. Monzani, A. Morselli, I. V. Moskalenko, E. Nuss, T. Ohsugi, N. Omodei, M. Orienti, E. Orlando, M. Palatiello, V. S. Paliya, F. de Palma, D. Paneque, J. S. Perkins, M. Persic, M. Pesce-Rollins, T. A. Porter, G. Principe, S. Rainò, R. Rando, P. S. Ray, M. Razzano, A. Reimer, O. Reimer, R. W. Romani, P. M. Saz Parkinson, C. Sgrò, E. J. Siskind, D. A. Smith, F. Spada, G. Spandre, P. Spinelli, D. Tak, J. B. Thayer, D. J. Thompson, D. F. Torres, E. Troja, G. Vianello, K. Wood, M. Wood, *Einstein@Home Discovers a Radio-quiet Gamma-ray Millisecond Pulsar*, Science Advances, Volume 4, Number 2, 2018

J. Wu, P. Torne, D. J. Champion, L. Guillemot, M. Kramer, *A Radio Pulsar Survey at Effelsberg using the Ultra Broad-Band (UBB) Receiver.* To be submitted to Monthly Notices of the Royal Astronomical Society, 2017

RHEINISCHE FRIEDRICH–WILHELMS–UNIVERSITÄT BONN

Summary

by Hung Kit (Jason) Wu for the degree of

Doctor rerum naturalium

Until the advent of *Fermi*, the majority of the pulsars known were radio selected and most of the pulsar studies were built around the radio framework. This presents a strong selection bias in the way that we study pulsars, which in turn limits our ability to understand the full picture of the pulsar population. We have learnt so much from the radio frequencies but it seems that the knowledge gained solely from the radio is insufficient to fully address all the fundamental questions, such as the Galactic pulsar population, the structure of the pulsar magnetosphere, the emission mechanism across the electromagnetic spectrum, the beaming fraction of pulsar emission at different wavelengths, and channels of pulsar spin-down power losses. Unfortunately, in the last few decades, pulsar studies at other wavelengths such as X-ray and γ-ray were lagging behind mostly because of the technical difficulties of space-based observations, where the positional accuracy and time resolution are very limited. However, this is no longer the case after *Fermi* Gamma-ray Space Telescope (*Fermi*) was launched.

The Large Area Telescope (LAT) on board of *Fermi* is a real game changer, as it enables the study of the pulsar population from a very different angle. In particular, it enables the studies of pulsars with weak or even non-detectable radio emission. *Fermi*-LAT's all-sky surveying mode and excellent time resolution (< 10 μs) enables the discoveries of different types of pulsars through γ-ray pulsations. Many of the young γ-ray pulsars discovered have not yet been detected in subsequent radio searches, such as the majority of pulsars presented in Chapter 4. Pulsars presented in Chapter 4 are young and energetic, their characteristic ages are smaller than 3 Myr and their spin-down powers are larger than 10^{33} erg s^{-1}. They all have low radio fluxes, only two out of the 13 pulsars were detected in deep radio follow-up observations. This radio-quiet γ-ray pulsar population can only be accessed through blind periodicity searches in γ-ray. Therefore, blind periodicity search in γ-ray is the only way to complete the radio-quiet part of the Galactic pulsar census.

Due to the ever-limited computational resources, selecting the right γ-ray sources to perform blind search is one of the keys to increase the chance of finding γ-ray pulsars. Fortunately, their spectral characteristics in γ-ray enable the application of machine-learning algorithms such as the Gaussian Mixture Model (GMM) presented in Chapter 2 to select pulsar-like γ-ray sources from the 3FGL catalog for our survey in Chapters 4 and 5. With the help of the semi-coherent search algorithm and Gaussian Mixture Model, we were able to detect 17 new γ-ray pulsars out of 118 selected 3FGL sources. For those 3FGL sources where no detection has been made, some of them may fall below the blind search sensitivity or they could be MSPs in binary systems.

In addition, we were also able to detect γ-ray pulsars that could not be detected in the past. For example, the young energetic PSR J1906+0720 (Section 5.1) was found in our data despite the giant glitch, one of the largest detected from a γ-ray pulsar, that occurred in the first year of the *Fermi* mission. Several complications for detecting PSR J1906+0720 were the positional offset caused by a previously undetected secondary γ-ray source, and the intense Galactic γ-ray diffuse emission. The detection of PSR J1906+0720 allows us to further improve our understanding of the energetic pulsar population. The 2,700 years old PSR J1208−6238 (Section 5.2) is the youngest radio-quiet γ-ray pulsar ever discovered, its high surface magnetic field strength (3.8×10^{13} G) and small characteristic age allow us to measure its braking index ($n = 2.598 \pm 0.01$) and thus study the spin-down process. The braking index of PSR J1208−6238 deviates from the simple dipole braking model ($n = 3$) which implies that the spin-down mechanism is not a pure magneto-dipole radiation. These studies are rare, so far ten pulsars offered such an opportunity. PSRs J1035−6720 and J1744−7619 (Section 5.3) are the only two isolated MSPs discovered without any information from other wavelengths. Despite the deep follow-up radio observations with the Parkes radio telescope, PSR J1744−7619 is still radio-quiet ($S_{1400} < 31$ μJy) while the best-fit emission geometry from its γ-ray pulse profile suggested otherwise. Other inconsistencies between models and observations have been found, such as PSR J0631+0646 (Chapter 4) where the current emission models failed to predict the observed radio-γ-ray phase lag. The discovery of PSRs J0631+0646 and J1744−7619 demand new approaches in emission modelling to explain the observables.

Despite the competition from a number of all-sky radio pulsar surveys, a significant portion of radio pulsars were found from targeted radio searches of unassociated LAT sources. This demonstrates that targeted searches of unassociated LAT sources are a complementary way to complete our knowledge on the pulsar population, especially for MSPs in binary systems. Phased Array Feed and Ultra-Wide-Bandwidth receivers are the main technologies for the next generation radio telescopes. The Ultra-Broad-Band receiver (UBB) is one of the prototypes of the Ultra-Wide-Bandwidth receiver technology being developed at the Effelsberg telescope. We explored the possibility of using the UBB for targeted pulsar searches on unassociated LAT sources at Effelsberg (Chapter 6). Unfortunately, UBB was strongly affected by Radio Frequency Interference (RFI) at the Effelsberg site. As a result, almost half of the observations were strongly affected because of the RFI. Also, the strong RFI at Effelsberg increased the system temperature ($T_{\rm sys}$) of the UBB by a factor > 2. Although we have not detected any radio pulsations, the experience gained from the survey provides valuable information, such as local RFI monitoring for future surveys at Effelsberg. Using the RFI information from the UBB survey, a new RFI filter is being developed at Effelsberg should bring the UBB sensitivity back to its nominal $T_{\rm sys} \simeq 20$ K, allowing pulsar broad-band spectral studies and targeted pulsar surveys. As similar Ultra-Wide-Band receiver technology are being developed for next generation radio telescopes like MeerKAT and the Square Kilometre Array (SKA), the lesson we have learnt from the UBB survey is beneficial in the deployment of the future Ultra-Wide-Bandwidth receivers. For example, although we may have missed some steep-spectrum radio pulsars in the UBB survey, the SKA-

LOW pulsar survey which is designed to operate in low frequency (100 - 450 MHz), is going to target this subset of pulsars.